Electrochemistry with nanoelectrodes

By

Jeyavel Velmurugan

A dissertation submitted to the Graduate Faculty of Chemistry in partial fulfillment of the requirements for the degree of Doctor of Philosophy, The City University of New York

2012

This manuscript has been read and accepted for the Graduate Faculty in Chemistry in satisfaction of the dissertation
requirement for the degree of Doctor of Philosophy

_____ _____

Date Chair of Examining Committee

_____ _____

Date Executive Officer

Dr. Michael Mirkin

Dr. James Rusling

Dr. Ronald Birke

Dr. Uri Samuni

Supervisory Committee

Abstract

Electrochemistry with nanoelectrodes

By

Jeyavel Velmurugan

Adviser: Prof Michael V. Mirkin

Nanometer-sized electrodes have drawn considerable interest in recent years. One of the reasons is that with nanoelectrodes one can obtain a high rate of mass transport and study kinetics of fast heterogeneous electron transfer (ET) reactions. They can also be used for high-resolution chemical imaging of surfaces and interfaces and as microscopic chemical sensors.

We developed methodologies for preparation and characterization of electrochemical nanoprobes and their use as tips in the scanning electrochemical microscope (SECM). The applications range from studies of hydrogen adsorption and spillover to high-resolution imaging of surface topography and reactivity to nanofabrication. Finally, some unusual physicochemical phenomena can be observed at nanointerfaces but are not accessible by macroscopic electrochemical probes will be discussed.

Visualization of the nanoelectrode surface is challenging, and the interpretation of the electrochemical response often relies on assumptions about its shape and size. Recently, we obtained the first AFM images of nanoelectrodes, which provide detailed and unambiguous information about the electrode geometry. *In-situ* AFM is also useful for monitoring surface reactions at nanoelectrodes. This approach was used to control electrodeposition of Pt black into an etched nanocavity and prepare well-shaped

platinized nanoelectrodes for intracellular measurements of reactive oxygen and nitrogen species. Another example is the study of nucleation and growth of individual metal clusters on nanoelectrodes monitored by the AFM.

Acknowledgements

I am grateful to my mentor, Prof. Michael Mirkin, for his guidance and care. Michael has been extremely supportive and has constantly encouraged me to challenge myself during the past five years. With his financial support I have been able to focus all my attention to my research work.

I would like to thank Prof. James Rusling, Prof. Ronald Birke and Prof. Uri Samuni for their guidance and interest in my education.

I would like to express my gratitude to my former and current colleagues Dr. Sun, Dr. Laforge, Dr. Zhan, Dr. Nogala, Dr. Noel, Dr. Kececi, Ms.Wang, Mr. Yu and Ms. Elsamadisi for their support.

The financial support from the City University of New York and the Electrochemical Society is deeply appreciated.

Finally I would like to express my gratitude to Prof. Rose Kfar Rose for her generosity.

Table of content

List of Tables

List of Charts

Chapter I

Nanoelectrodes and SECM

1.1 Introduction

The introduction of micrometer-sized electrodes led to significant advances in studies of fast heterogeneous and homogeneous reactions, measurements in various microenvironments, and high resolution electrochemical imaging.[1] Even smaller, i.e., nanometer-sized electrodes are required for characterization of the electrode/electrolyte interfacial processes with nanometer-scale resolution.[2] The initial stages of many important processes, such as metal corrosion and heterogeneous nucleation, include formation of nanometer-sized transient structures. [3] To probe such structures electrochemically, one needs a comparably sized electrode. The ability of nanoelectrodes to quickly attain steady-state is used for imaging and its fast mass-transfer rate helps in kinetic measurements in fast electron transfer reaction. During the last several years, a few research groups have been exploring different methodologies of manufacturing nanometer-sized disks, bands, cones, and arrays of UMEs,[4-10]

The polished, flat nano-tips can yield more reliable and reproducible data. Some of the problems in working with these nanoelectrodes are imperfect shape, difficult visualization and characterization, and low current measurements. The voltammetric response of a nanoelectrode does not provide sufficient information about the geometry of either the conductor exposed to electrolyte or the insulating sheath. The diffusion to a small electrode (hemisphere, cone, disk) rapidly becomes hemispherical when the electrode is in the bulk solution far from any object. [11] Thus, the shape of a reversible steady-state voltammogram is the same for any electrode geometry. Scanning electrochemical microscopy (SECM) and atomic force microscopy (AFM) were shown to be most useful techniques for nanoelectrode characterization. [34]

The advantages of polished disk-type nanoelectrodes can be fully realized by employing them as SECM tips.[35] They can greatly enhance the SECM capacity for acquiring spatially resolved chemical information, which makes it a powerful tool for visualizing microstructures and studying surface processes. The ultimate resolution of the SECM is limited by the size and geometry of the probe (nanoelectrode). The fabrication and characterization of the SECM probe are therefore important for the acquisition of reliable data.

1.2 Nanoelectrodes

The fabrication of a nanotip starts with pulling a micrometer-sized metal wire into a glass capillary. Briefly, an annealed 25-µm wire was inserted into a borosilicate capillary (1.0-mm o.d., 0.58-mm i.d.), which was fixed in the V groove of the Sutter P-2000/G laser pipet puller. The designed programs were used to produce Pt or Au nanoelectrodes with a desired size and shape. A pulled capillary with a sealed Au wire was polished using a BV-10 micropipet beveller under video microscopic control. The micromanipulator was used to move the capillary vertically towards the rotating disk to which a 50 nm lapping tape was attached. During polishing, the pipet axis was made exactly perpendicular to the rotating disk using a plumb bob and a two-axis bubble level. Additional fine polishing was done with 50-nm alumina particles placed on the same rotating disk. The polished electrodes were rinsed with water and annealed in the oven at 90 ºC for an hour. The schematics of a typical nanoelectrode is shown in Fig 1.1.

The important parameters for the tip geometry are (1) the radius, a of the conductive core; and (2) the total tip radius (insulating sheath thickness plus the radius of the electroactive area), r_g. The dimensionless parameter RG = r_g/a.

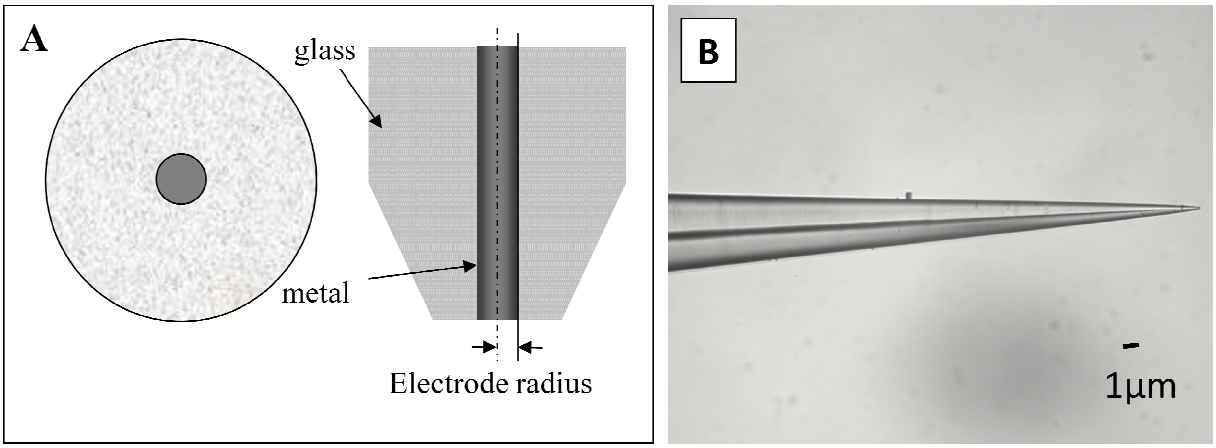

Figure 1.1. A - Schematics of a nanoelectrode. The exposed metal is the active part of the electrode. B- Optical micrograph of a UME tip. The platinum wire is sealed inside a glass sheath.

1.3. SECM principle of operation

Figure 1.2 shows the basic setup of an SECM instrument employing an amperometric microprobe or ultramicroelectrode (UME). An UME, the tip, is attached to a 3D piezo positioner, controlled by a computer, which is also used for data acquisition. A bipotentiostat (i.e., a four-electrode potentiostat) controls the potentials of the tip and/or the substrate versus the reference electrode and measures the tip and substrate currents. The SECM instrument is often mounted on a vibration-free optical table inside a Faraday cage to isolate it from environmental electromagnetic noise. The tip current varies depending on the environment of the tip. When the tip is approached close, i.e. a few radii, to the substrate one can obtain information about the substrate.

In a feedback mode experiment, the tip is immersed in a solution containing redox mediator (e.g., an oxidizable species, R). When a sufficiently positive potential is applied to the tip, the oxidation of R occurs via the reaction

$$R - ne^- \rightarrow O \qquad (1.1)$$

at a rate governed by the diffusion of R to the UME. If the tip is far (i.e., greater than several tip diameters) from the substrate (Fig. 1.3A) the steady-state current, $i_{T,\infty}$, is given by

$$i_{T,\infty} = 4nFDca \qquad (1.2)$$

where F is the Faraday constant, n is the number of electrons transferred in the tip reaction, D is the diffusion coefficient of R, c is the bulk concentration of R, and a is the tip radius.

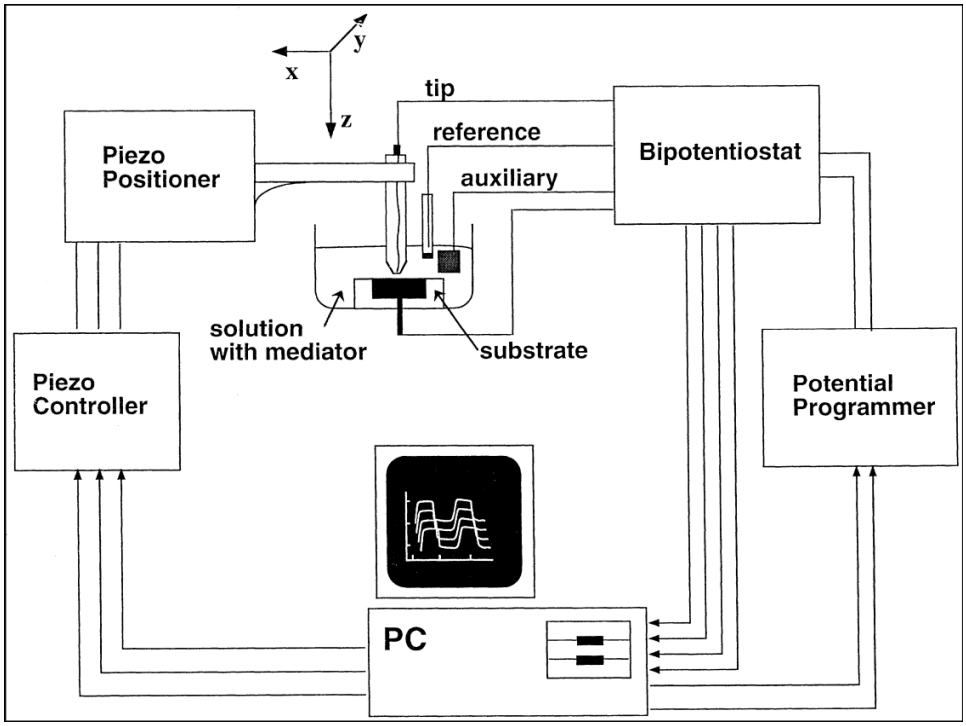

Figure 1.2. schematics of an SECM setup. (From Ref. 14).

When the tip is brought to within a few tip radii of a conductive substrate surface (Fig. 1.3B), the O species formed in the reaction (1.18) diffuses to the substrate where it may be reduced back to R

$$O + ne^- \rightarrow R \qquad (1.3)$$

This process produces an additional flux of R to the tip and hence "positive feedback", i.e., an increase in tip current ($i_T > i_{T,\infty}$). The smaller the tip-substrate distance (d), the larger is i_T. In fact, when reaction (1.3) is rapid, $i_T \rightarrow \infty$ as $d \rightarrow 0$.

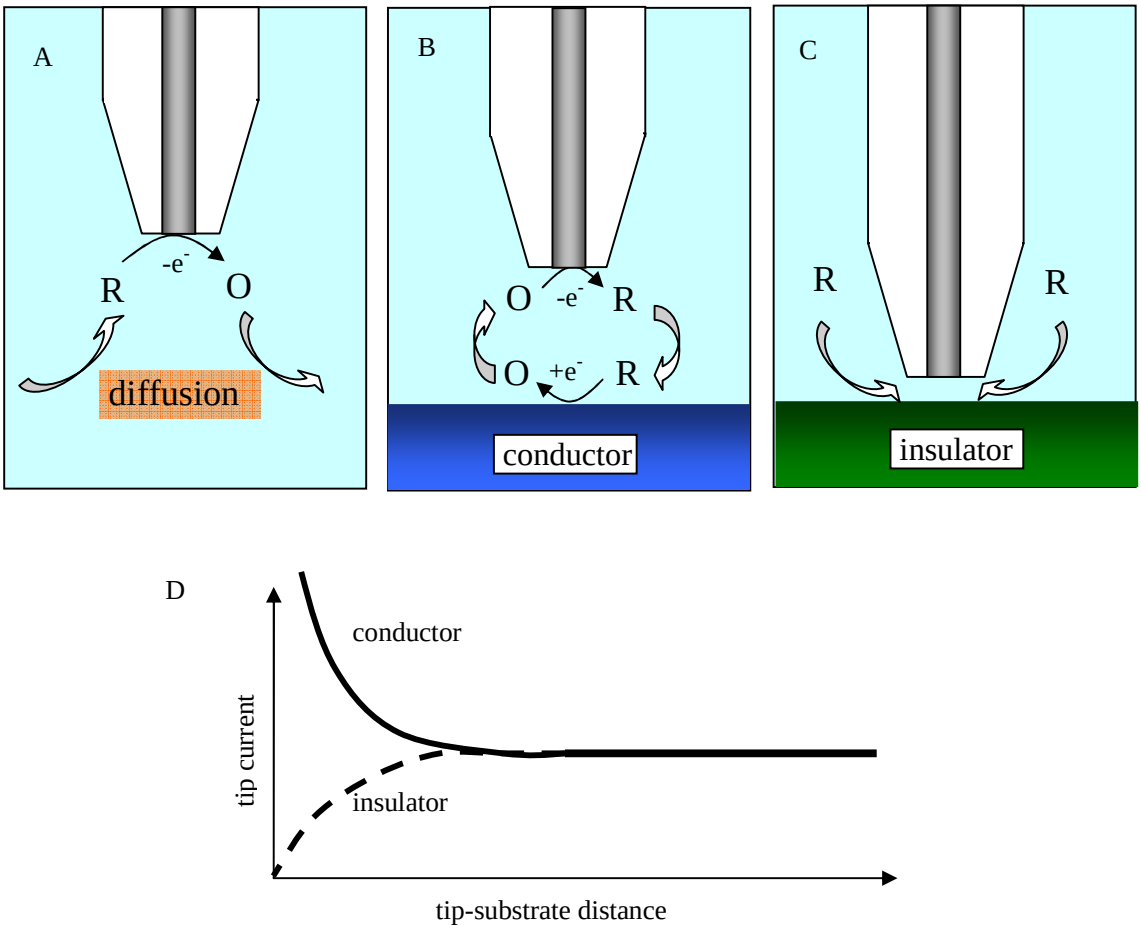

Figure 1.3. Feedback mode. A- Bulk oxidation – no feedback. B- oxidation near a perfect conductor – positive feedback. C- oxidation near a perfect insulator – negative feedback. D- Approach curves corresponding to B and C.

If the substrate is an inert electrical insulator the tip-generated species, O, cannot react at its surface. At small d, $i_T < i_{T,\infty}$ because the insulator blocks diffusion of species R to the tip ("negative feedback"; Fig. 1.3C). The closer the tip is to the insulator substrate, the smaller i_T will be, with $i_T \rightarrow 0$ as $d \rightarrow 0$. Overall, the rate of mediator regeneration at the substrate determines the magnitude of the tip current, and conversely the measured i_T vs. d dependence ("approach curve") provides information on the kinetics of the process at the substrate.

The rate of reaction (1.3) can be controlled by applying a suitable potential to the substrate by a potentiostat. Alternatively, the potential of a conductive substrate (E_s) may be determined by concentrations of redox species in solution without an external bias. For example, if the solution contains only the reduced form of the redox species, most of the substrate, which is usually much larger than the tip, is in contact with a solution of R. According to the Nernst equation

$$E_S = E° + RT/nF\ln c_O/c_R \qquad (1.4)$$

in this case $E_S - E° << 0$, where $E°$ is the standard potential of the mediator.

1.4. Experimental issues with Nanoelectrodes.

1.4.1. Electrode size and shape characterization. The characterization of a nanoelectrode includes the evaluation of its effective radius, true surface area exposed to solution, and the thickness of the insulting sheath, as well as the determination of the electrode geometry. In most published studies, the electrode radius was evaluated from the steady-state diffusion limiting current assuming either hemispherical, or conical, or planar disk geometry. For a non-flat electrode, this assumption is often problematic because of essentially unavoidable imperfections of its geometry. A more reliable approach is to use fast-scan voltammetry of adsorbed species to evaluate the effective surface area of the electrode.[15] The combination of the area value with the radius value obtained from steady-state voltammetry of dissolved redox species allows more complete characterization of the nanoelectrode geometry. However, it was difficult to use the same electrode for area measurements and kinetic experiments and to accurately measure the amount of adsorbed species for electrodes smaller than ~60-nm radius.[15]

Several authors used SEM to evaluate the size and shape of the tip. However, even for relatively large electrodes (e.g., a > 50 nm) SEM micrographs provide mostly qualitative information that cannot be used for quantitative modeling of the electrode response. For example, from the SEM micrograph shown in Fig. 1.4,[18] the authors inferred that the imaged electrode is not a true hemisphere; nevertheless in kinetic analysis they had to assume a hemispherical geometry. Even more importantly, SEM images do not provide any information about the exposed metal surface area or solution leakage (see the next section). Some of these issues can be addressed by using a nanoelectrode as an SECM tip. Major differences in the shape of the current vs. distance curves obtained with flat (disk-type) tips and with protruding tips shaped as a cone or a spherical cap allow one to evaluate the effective radius and the height of a nanoelectrode.[19] It was shown later that the depth of the recess of the conductive surface into the insulator can also be evaluated by fitting an experimental approach curve to the theory.[20] An advantage of the SECM characterization is that it is based not on the appearance of a nanoelectrode, but on its electrochemical response, which is much more relevant to kinetic measurements. However, if the geometry of a non-planar tip is imperfect, fitting an experimental approach curve to the theory may be problematic. The SECM is most useful for characterizing planar electrodes because high positive (or negative) feedback can only be

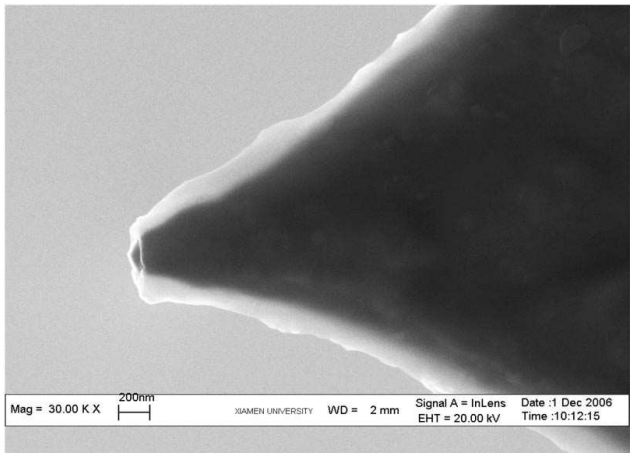

Figure 1.4. SEM image of an etched Pt-Ir electrode (a ~ 60 nm) coated with cathodic electrophoretic paint.[18]

obtained with a flat, well polished tip whose entire surface can be brought close to the flat substrate.

In Figure 1.5A, an SECM approach curve is fitted to the theory with a = 46 nm. The same a value was obtained independently from the diffusion limiting current at the same Pt electrode (Fig. 1.5B). The radius value is reliable because of the high positive feedback current (up to a

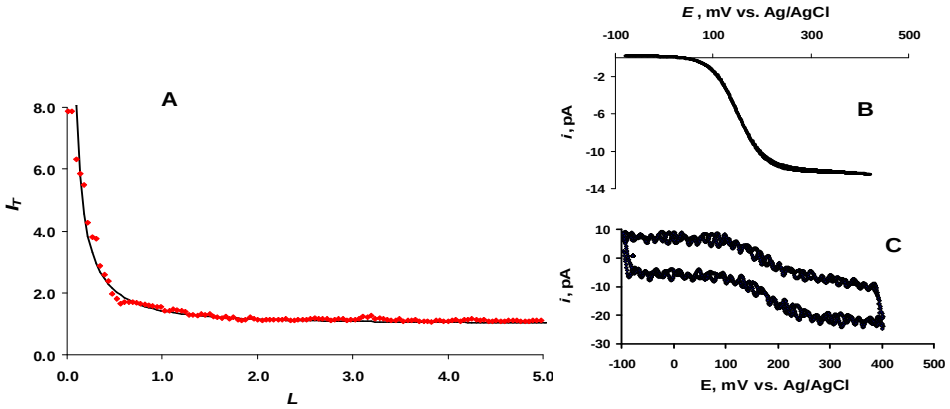

Figure 1.5. SECM current vs. distance curve (A), steady-state voltammogram (B), and two successive fast-scan cyclic voltammograms (C) obtained with a 46-nm-radius polished Pt tip. Aqueous solution contained 1 mM $FcCH_2OH$ and 0.2 M NaCl. (A) Theoretical curve (solid line) for diffusion-controlled positive feedback was calculated from Eq. (6). Symbols are experimental data. The tip approached the unbiased Au film substrate with a 5 nm/s speed. v = 50 mV/s (B) and 10 V/s (C). [20]

normalized current of 8). The distance of the closest approach in Fig. 1.5A (~5 nm) could be achieved only with the essentially flat and well-polished tip surface. Fast scan voltammetry can be used to check that the true area of the nanoelectrode is not much larger than its geometrical area. A relatively low charging current and practically identical successive fast-scan voltammograms (Fig. 1.5C) are expected in this case.

Presently, good quality SECM approach curves can only be obtained for nanoelectrodes with the radii $\gtrsim$ 10 nm. Several recent attempts to employ extremely small (a < 5 nm) electrodes for kinetic experiments underscore the importance of developing characterization techniques for

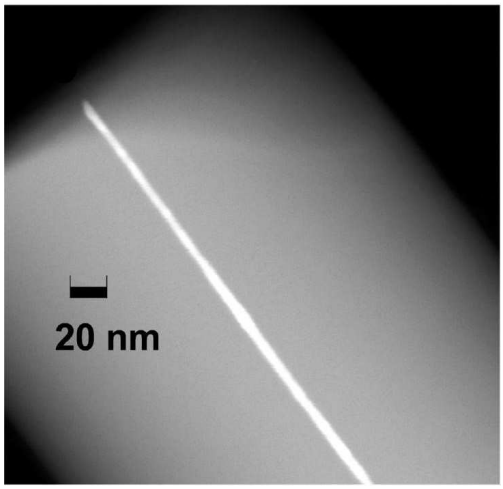

Figure 1.6. TEM image of a 3 nm radius Pt nanoelectrode sealed in SiO_2.[32]

such electrodes. Li *et al.*[32] presented TEM side views of ≤3 nm radius Pt wires inside the insulating sheath of their nanoelectrodes. These impressive micrographs unambiguously demonstrate that the radius of the conductive core is comparable to the effective value of the electrode radius obtained from diffusion limiting current. So far, no similar resolution images of the exposed metal surface have been reported, and therefore the geometry of ultra-small nanoelectrodes remains largely unknown. The main issues are the possibility of solution leakage (see the next section) and whether these electrodes are essentially flush with the surrounding insulator or recessed, or protruding. For instance, a very small, 1 nm recess would cause the current to a 1-nm-radius electrode to be only 43% of the current to the equally sized, non-recessed disk.[20]

1.4.2.Solution leakage. Detecting solution leakage through the insulator/metal boundary is very difficult. This phenomenon (as well as the related "lagooned geometry"[33,34]) may not be apparent from the value of the diffusion limiting current or the shape of a steady-state voltammogram. The leakage is supposed to increase the surface area of the metal/solution interface and therefore the double layer charging current. However, the apparent capacitance of

a nanoelectrode is much larger than the capacitance of the metal/solution nanointerface due to "stray capacitance" of its insulated portion and wiring. Thus, detecting the leakage from capacitive current (e.g., by increasing the potential sweep rate) is not straightforward.

Fast scan voltammetry can be used to evaluate the electrode surface area by measuring the total charge of an adsorbed molecular monolayer[15] and to compare it to the geometric surface area calculated from the apparent radius of the nanoelectrode. An agreement between the two area values provides strong evidence against solution leakage. However, the adsorbed species must be immobilized on the surface, and surface diffusion must be negligibly slow; otherwise, a monolayer of adsorbed molecules may form on the lateral surface of the nanowire (i.e., at the metal/glass interface) thus greatly increasing the effective surface area. Another approach to leakage detection is based on the comparison of fast scan (e.g., 10 – 50 V/s) and slow scan (e.g., ≤ 200 mV/s) voltammograms of the dissolved species (Figs. 1.5B and 1.5C). In the case of leakage, the presence of a thin layer of solution containing electroactive species inside the insulating sheath should result in peak-like features in fast-scan voltammograms, with a peak height proportional to the scan rate. By contrast, sigmoidal fast-scan voltammograms very similar to the slow-scan, steady-state voltammograms—except for a moderate charging current contribution (Fig. 1.5C)—point to the consistent seal and no solution leakage. Well shaped SECM approach curves showing high positive (and negative) feedback response in good agreement with the theory have also been considered as an evidence against leakage.[17]

1.4.3. Deviations of nanoelectrode responses from classical theory. An implicit assumption in classical electrochemical theory is that the electrode dimensions are much larger than the thickness of the diffuse double layer and incomparably larger than the radius of species involved in the interfacial CT reaction. Starting with the pioneering work of Smith and White,[22]

a number of theoretical and experimental studies focused on possible deviations from conventional electrochemical theory at nanometer-sized electrodes and in nanometer-thick TLCs. The most extensively discussed is the effect of diffuse layer on mass-transfer, which is expected to be significant if the diffusion layer thickness is comparable to that of the diffuse double layer.[22-24] The magnitude of this effect and its influence on the values of kinetic parameters extracted from a steady-state voltammogram depends on a number of factors including the charge of electroactive species, its standard potential (with respect to the potential of zero charge), and the ionic strength of solution. In most cases, the predicted deviations should be significant at $a \leq 10$ nm and barely detectible at $a \geq 100$ nm.[35] A new treatment for disk nanoelectrodes based on Marcus theory and taking into account long-distance ET predicted especially dramatic effects (e.g., peak-shaped voltammograms) for extremely small ($a \leq 5$ nm) electrodes and multicharged ions.[24] For oxidation/reduction of neural species (e.g., Fc or FcMeOH) the double layer effects are much less important.

In ref. 25, ET rates were measured for the $Fc(CN)_6^{3-}$ / $Fc(CN)_6^{4-}$ couple in 1 M KCl at a number of paint-coated, etched Pt electrodes with a varied between 10 nm and several μm. To explain observed deviations from conventional voltammetric theory, the authors carried out Monte Carlo simulations of nm-thick TLCs and concluded that the rate constants found from $E_{1/2}$ values at nanoelectrodes with 10 nm < a < 300 nm were overestimated by the factor of three due to non-negligible length of the mean free path of the diffusing redox species in comparison with the electrode size.

More recent Brownian dynamics simulations[26] coupled with long-range ET probability values predicted a “tunneling depletion layer” that should result in a potential-dependent

diffusion-limited current and non-sigmoidal current vs. potential dependences at very short TLC thicknesses (e.g., ~1 nm).

From the analysis of collisional encounters between the redox molecule and electrode surface based on Brownian dynamics simulations, it was concluded that the largest heterogeneous ET rate constant observable at the nanoelectrodes in conventional solvents should be ~5 cm/s. [27] An opposite situation—a relatively slow ET reaction occurring at a very small electrode—was recently treated by Feldberg[28] who suggested that application of the Butler-Volmer formalism in this case should yield incorrect values of k^o and meaningless values of α. Moreover, the Marcus-Hush model predicts a limiting current for such systems that can be significantly smaller than the mass transport limited current.[28]

A number of size-related electrochemical phenomena and their effects on ET rates have yet to be explored. For instance, the discreteness and stochasticity of ET events at nanointerfaces may be yet another source of deviations from classical theory.[29] Numerical simulations based on the electrochemical master equation suggested that ET rate at a nanoelectrode should be significantly faster than the rate of the same reaction at a macroscopic electrode.[29] A more rapid potential drop within the diffuse double layer at a hemispherical electrode smaller than 50 – 100 nm should also result in an enhanced driving force for ET.[30] Negative charges residing on the insulating surface can affect mass transfer (and consequently the apparent ET rate) at glass-sealed nanoelectrodes.[31]

No comprehensive theoretical description of ET reactions at nanointerfaces is currently available to take into account all size-related phenomena discussed above. The relative importance of each effect remains incompletely understood. To observe and quantitatively evaluate major deviations from conventional theory, one needs electrodes smaller than ~5-nm

radius with well characterized geometry, which have yet to be fabricated. Some striking voltammetric features predicted by recent models have not yet been observed, and in some cases no significant differences were found between kinetic parameters determined at very small and at much larger nanoelectrodes.[32] At the same time, deviations from conventional theory observed at relatively large (e.g., up to 300 nm[25]) electrodes as well as a non-linear concentration dependence of the diffusion current[36] are likely to be artifacts.

1.5. Heterogeneous electron transfer at metal/solution nanointerfaces

The ET current expressed by the Butler-Volmer equation is proportional to the product of k^o and the electrode surface area.[2] Thus, the reliability of nanoelectrochemical kinetic experiments is largely determined by our knowledge of the electrode geometry and the true surface area exposed to solution. An early report by Penner et al.[37] has demonstrated a great potential of nanoelectrodes for fast kinetic measurements and gave a powerful impulse to the development of electrochemical nanoprobes. At the same time, this work exposed the perils of using nanoelectrodes without proper characterization. It was suggested that extremely high k^o values obtained in ref. 37 for several outer-sphere ET reactions resulted from the recession of the electrode into a small chamber of surrounding insulator ("lagooned geometry").[38-39] Several approaches to improving fabrication and characterization of nanoelectrodes resulted in more consistent ET measurements surveyed below. This review does not include the data obtained with no supporting electrolyte because the existing theory does not provide quantitative treatment for very significant double layer and ion pairing effects expected in this case.[40,41]

1.5.1 ET kinetics measured by nanoelectrochemical techniques.

Two main strategies employed in fabrication of axisymmetric (i.e., disk-type, spherical cap, or conical) nanoelectrodes have been etching/insulating[42,43] and pulling/heat sealing into

glass capillaries.[44] The former approach typically yields non-polishable conical or spherical-type tips, while pulled electrodes can be polished.[16,26-29] Both types of probes have been employed in ET measurements by steady-state voltammetry.[44-47] Polished electrodes with a thin insulating sheath (i.e., the ratio of the insulator thickness to the disk radius, $RG = r_g/a \leq 10$) have been employed as SECM tips for feedback mode kinetic experiments.[20] The results of nanoelectrochemical ET experiments are summarized in Table 1.1.

Watkins et al.[48] measured the kinetics of ferrocenylmethyltrimethylammonium ($TMAFc^+$) oxidation at 19 quasi-hemispherical Pt electrodes with the effective radius varied between 2 nm and 150 nm. This work shows how hard it is to make kinetic measurements at non-flat nanoelectrodes. Despite major efforts made to characterize the electrode size and shape (see the next section) and a large number of analyzed voltammograms, a significant uncertainty in the determined rate constant was apparently due to imperfect electrode geometry. Importantly, no strong correlation was found between the electrode size and the measured kinetic parameters even for the radii as small as $a \leq 10$ nm, for which such correlation can be expected from existing theory. Another important lesson to be learned from ref. 48 is that an individual kinetic experiment at a nm-sized electrode may not be reliable. To ensure that the results are meaningful, one has to treat a number of CVs obtained for a wide range of experimental conditions.

Similar quasi-hemispherical Pt electrodes were used to study kinetics of $IrCl_6^{3-}$ oxidation.[22] The electrode radii in this case were somewhat larger (48 nm - 654 nm), which may be the reason for much smaller uncertainties in the measured kinetic parameters. The authors have stressed significant deviations of the nanoelectrode responses from the classical theory observed in the absence of the supporting electrolyte and additional complications caused

by ion pairing. However, no effect of the electrode size on the measured ET rate with excess KCl was reported, and the k^o values measured at nanoelectrodes were similar to those obtained at larger electrodes in ref. 40 and in the literature.

Table 1.1 ET kinetic parameters measured by nanoelectrochemical approaches.

redox couple	electrolyte	k^o, cm/s	α	electrode, *a* (nm)	method	Ref.
$TMAFc^+/TMAFc^{2+}$	0.2 KCl	4.8 ± 3	$0.6_4 \pm 0.1_5$	Pt quasi-hemisphere 1.7 – 150	steady-state voltammetry	48
$IrCl_6^{3-}/IrCl_6^{2-}$	0.5 M KCl	2.9 ± 0.2	0.50 ± 0.01	Pt quasi-hemisphere 48 – 654	steady-state voltammetry	40
$FcMeOH/Fc^+MeOH$	0.2 M NaCl	6.8 ± 0.7	0.42 ± 0.03	polished Pt 25 – 290	SECM	20
Fc/Fc^+ in acetonitrile	0.3 M $TBAClO_4$	8.4 ± 0.2	0.47 ± 0.02	polished Pt 3.7 – 142		
$Ru(NH_3)_6^{3+}/ Ru(NH_3)_6^{2+}$	0.5 M KCl	17.0 ± 0.9	0.45 ± 0.03	polished Pt 14.7 – 282		
TCNQ/TCNQ- in acetonitrile	0.1 M $TBAClO_4$	1.1 ± 0.04	0.42 ± 0.02	polished Pt 76 – 386		
$Fc(MeOH)_2/Fc(MeOH)_2^+$	0.25 M KCl	6.0 ± 1.4	0.49 ± 0.09	Pt TLC *d* = 50 nm	steady-state voltammetry	16
	2 M KCl	>13	0.49 ± 0.13			
	0.25 M $NaClO_4$	3.2 ± 0.5	0.56 ± 0.07			
	2 M $NaClO_4$	1.5 ± 0.2	0.55 ± 0.04			
$Ru(NH_3)_6^{3+}/Ru(NH_3)_6^{2+}$	0.2 M KNO_3	8.6	0.58	Pt/Hg TLC *a* = 8.2 nm *d* = 1.2 nm	single molecule steady-state voltammetry	17
$Fc(CN)_6^{3-} / Fc(CN)_6^{4-}$	0.5 M KCl	0.12 – 17.3	–	Pt-Ir cone 1.1 – 95.6	low-overpotential polarization curves	18
$TMAFc^+/TMAFc^{2+}$	0.5 M KCl	1.1 – 11.9	–	Pt-Ir cone 1.5 – 150		
$IrCl_6^{3-}/ IrCl_6^{2-}$	0.2 KCl	0.5 – 13	0.72 ± 0.15	polished Pt 0.6 – 62.5	steady-state voltammetry	32
Fc/Fc^+ in acetonitrile	0.2 M $TBAClO_4$	3.4 – 13.4	0.85 ± 0.06	polished Pt 1.6 – 183.5		
$FcMeOH/Fc^+MeOH$	0.1 M NaCl	0.5 – 18.8	0.78 ± 0.16	polished Pt 3.8 – 132		

Another kinetic study[18] employed non-flat Pt –Ir electrodes with the radii ranging from extremely small (e.g., 1.1 nm) to relatively large (e.g., 150 nm). Unlike other results summarized in Table 1.1, the rate constants determined for $FcTMA^{2+}/FcTMA^+$ and $Fe(CN)_6^{3-}$

/$Fe(CN)_6^{4-}$ redox couples increased markedly (i.e., by about one and two orders of magnitude, respectfully) with decreasing *a* value. Moreover, the k^o values obtained for the former species at larger nanoelectrodes were several times lower than those measured in ref. 15 for the same reaction or for oxidation of either aqueous ferrocenemethanol (FcMeOH)[20] or ferrocenedimethanol ($Fc(MeOH)_2$) in KCl.[16] Besides the uncertainties in electrode geometry, these results may also have been affected by unusual approach to data.

No strong correlation between the electrode radius and kinetic parameters was found with glass-sealed polished nanoelectrodes.[47] The average rate constant values determined for the oxidations of Fc and FcMeOH and $IrCl_6^{3-}$ were close to those found by other groups. However, the variation in k^o was significant (e.g., more than an order of magnitude for the oxidation of FcMeOH) and the determined α values were much higher than α = 0.5 expected from classical ET theory and also higher than the values reported by others (Table 1.1).

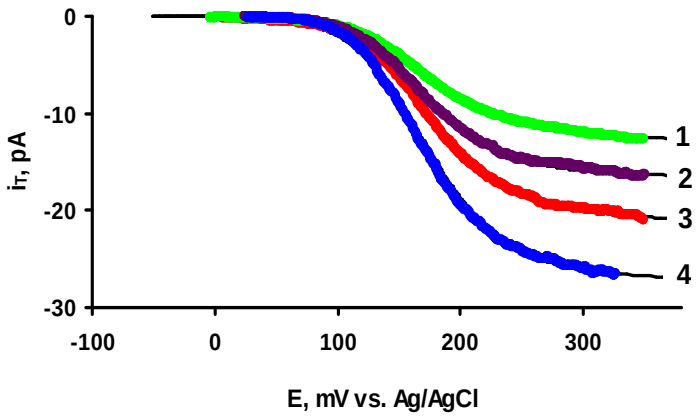

Figure 1.7. Experimental (symbols) and theoretical (sold lines) steady-state voltammograms of 1 mM FcMeOH in 0.2 M NaCl obtained at different separation distances between the 36-nm Pt tip and Au substrate. $d = \infty$ (1), 54 nm (2), 29 nm (3), and 18 nm (4). v = 50 mV/s. Theoretical curves were calculated from Eq. (5) [20]

Kinetic measurements by SECM combine useful features of ultramicroelectrodes and thin-layer cells(TLC). For short tip-substrate distances, the attainable *m* can be several times higher than its value at the same tip electrode in the bulk solution. In this way, the kinetics of the fast oxidation of ferrocenemethanol (FcMeOH) at Pt was measured (Figure 1.7).[20] Reproducible k^o and α values were obtained from dozens of steady-state voltammograms recorded at different polished Pt tips and over a wide range of the tip/substrate separation distances. Three other rapid ET reactions—the reduction of 7,7,8,8-tetracyanoquinodimethane (TCNQ) and the oxidation of ferrocene (Fc) in acetonitrile, and the reduction of $Ru(NH_3)_6^{3+}$—were investigated in a similar manner. The essential independence of kinetic parameters of *m*, which was varied two orders of magnitude, suggested the validity of the experimental results.

Steady-state voltammetry in nano-TLCs was described in two publications. A 50-nm thick nanofluidic cell with a well-defined geometry was fabricated and used to measure kinetics of $Fc(MeOH)_2$ oxidation with different supporting electrolytes.[16] While the kinetic parameters determined in KCl solutions were reasonably close to those measured by SECM for FcMeOH,[16] the effects of the nature and concentration of electrolyte on k^o and i_d values have yet to be clarified. Unlike SECM, neither the electrode radius nor the separation distance in the nano-TLC can be varied easily. Thus, all measurements in ref. 16 were made using essentially identical devices. An advantage of such an approach is in high reproducibility of kinetic experiments. At the same time, changing the dimensions and mass-transfer characteristics of a TLC to check the data validity and investigate the origins of unusual effects of the electrolyte concentration on ET was not possible. In Ref. 17, the use of a very small TLC (a = 8.2 nm, d =

1.2 nm) enabled kinetic measurements at the level of a single molecule. The rate constant value found for the reduction of $Ru(NH_3)_6^{3+}$ was slightly lower than that measured by SECM in a KF solution; however, the results of this proof-of-concept experiment have yet to be reproduced.

The nanoelectrochemical ET experiments summarized in Table 1 involve nine redox couples, several electrolytes, and three different solvents. Surprisingly, most measured k^o values (except for a few values obtained at poorly characterized electrodes) are spread within one order of magnitude. By contrast, the homogeneous self-exchange rate constants of the same redox species cover the range of more than six orders of magnitude (e.g., from ~10^3 $M^{-1}s^{-1}$ for $Ru(NH_3)_6^{3/2+}$ to 10^9 $M^{-1}s^{-1}$ for TCNQ/$TCNQ^-$). Moreover, no direct correlation between the homogeneous and heterogeneous rate constants expected from the Marcus formula was found. There are also no striking differences between the rate constants measured by different techniques and at electrodes of different dimensions.

Chapter II

Effect of Electrode Material on Electron Transfer Rates

2.1 Introduction

The availability of nanometer-sized electrochemical probes with well-characterized geometry and desired properties is essential for electrochemical experiments on the nanoscale.[1] The nanoelectrodes of various geometries, such as disks, bands, cones and recessed electrodes, were produced by several research groups.[2-15] The preparation and characterization of the disk-type, polished nanoelectrodes with a radius, $a \geq 3$ nm has been reported previously from our lab.[15a] A small *RG* value (i.e., the ratio of the insulating sheath radius to *a*) of <10 allowed such electrodes to be used as tips in scanning electrochemical microscopy (SECM) and to serve as nanoprobes for experiments inside living cells[15c] and in electrochemical nano-junctions.[15d]

All nanoelectrodes previously fabricated in our laboratory were made of Pt. Other metal (e.g., Au) electrodes may be required for various applications (e.g., surface modification by molecular self-assembly,[16] electrocatalysis,[17] or kinetic measurements). Zhang *et al*.[3d] recently reported the preparation of nanometer-sized Au and Pt glass-sealed nanoelectrodes. In that work, the same methodology was used to fabricate Pt and Au nanoelectrodes with thick insulating glass (large *RG*). However, significant modifications in pulling procedures are required to produce Au SECM nanotips with $RG \leq 10$.

Here, we employ Au nanoelectrodes to study heterogeneous electron transfer (ET) kinetics. With nanoelectrodes, one can attain a high rate of mass transport and study kinetics of

fast ET under steady-state conditions.[18] In the previous study,[15a] the kinetic parameters of several rapid ET reactions were extracted from SECM voltammograms obtained at the tip electrode positioned near a conductive substrate. The tip potential was swept slowly to obtain a steady-state voltammogram, while the substrate was poised at a constant potential, at which the regeneration of the redox mediator was diffusion controlled.[19] In feedback mode SECM experiments, the shorter the separation distance between the tip and the conductive substrate (d), the larger the mass transfer coefficient (m).[20] Thus, the mass transfer rate could be changed within a wide range (e.g., by more than two orders of magnitude[15a]) by varying a and d. Using this approach, the kinetic parameters were measured for four rapid outersphere ET reactions (i.e., the oxidations of ferrocenemethanol in water and of ferrocene in acetonitrile, and the reductions of $Ru(NH_3)_6^{3+}$ in 0.5 M KCl and of TCNQ in acetonitrile) at Pt nanoelectrodes.[15a] The standard rate constants ($k°$) measured at nanoelectrodes were similar to or somewhat higher than the values obtained previously at larger electrodes. They also were essentially independent of both from a and d—an important test of the data validity.

No direct correlation was found in ref. 15a between the measured electrochemical rate constants and corresponding self-exchange rate constants (k_{ex}): the lowest $k°$ was measured for the redox couple with the fastest k_{ex} ($TCNQ/TCNQ^-$), and vice versa, the fastest heterogeneous rate constant was obtained for $Ru(NH_3)_6^{3+/2+}$ in 0.5 M KCl whose k_{ex} was the lowest among the studied couples. It was suggested that the measured rates may reflect the differences in adiabaticity of those heterogeneous ET processes. Although it is pretty common to invoke the adiabaticity argument when the measured ET rates are lower than those predicted theoretically, few experimental observations of definitely nonadiabatic electrochemical ET have been reported to date.[21]

The extent of adiabaticity can be evaluated by probing the effect of the electrode material on the ET rate. According to Gosavi and Marcus,[22] the rate constant is expected to be proportional to the density of electronic states of the metal at the Fermi level (ρ_F) for nonadiabatic ET and independent of ρ_F in the adiabatic case. For the former case, they predicted the ratio of standard rate constants of the same ET at Pt and Au electrodes to be ~1.8 (assuming that the reorganization energy, λ, is the same for both electrodes) because the ρ_F of Pt is larger. While this prediction has been corroborated experimentally for ET across self-assembled monolayers,[23] no similar results have yet been obtained at bare metal electrodes. Similar rate constants were measured at Pt and Au for various redox species, e.g., benzoquinone in dimethylformamide,[24] or $Ru(NH_3)_6^{3+/2}$ in 1 M KF.[25] In addition to double-layer effects that can compromise the comparative ET measurements,[23] relatively low mass-transfer rates attainable at macroelectrodes may have thwarted previous attempts to detect differences in k^o at different metal surfaces. Here, we compare the results of kinetic experiments at Au nanoelectrodes to those done at similarly sized Pt tips in ref. 15a in order to investigate the effect of electrode material on the rates of fast ET reactions and detect possible nonadiabaticy.

2.2 Experimental Section

Chemicals. Ferrocenemethanol ($FcCH_2OH$, 97%) from Aldrich (Milwaukee, WI) was recrystallized twice from acetone. Hexaammineruthenium (III) chloride (99%) was obtained from Strem Chemicals (Newburyport,MA). Tetrathiafulvalene (97%), 2,2,6,6-tetramethyl-1-piperidinyloxy free radical (TEMPO, 96%), and methylphenothiazine (98%) were from Aldrich (Milwaukee, WI). 7,7,8,8-tetracyanoquinodimethane (TCNQ, 98%) and, ferrocenemethanol ($FcCH_2OH$, 97%) from Aldrich were recrystallized twice from acetone. Ferrocene (Fc, 98%; Aldrich) was sublimed twice before use. Tetrabutylammonium perchlorate (Fluka), NaCl, KI, $LiSO_4$ and KCl (99+%, Aldrich) were used as supporting electrolytes. Aqueous solutions were

prepared from deionized water (Milli-Q, Millipore Co.). Either 99.95% acetonitrile (Aldrich), or twice distilled HPLC grade DCE (Sigma-Aldrich) was used to prepare organic solutions.

Electrodes and electrochemical cells. A two-electrode configuration was employed with a 0.25-mm-diameter Ag wire coated with AgCl serving as a reference electrode. 100-nm-thick evaporated Au films on glass prepared with the aminosilane coupler and annealed[26] were obtained as a gift from Alexander Vaskevich (Weizmann Institute of Science) and used as a conductive SECM substrate. The cell was made by attaching a 7 mm glass tube to the Au coated slide, which was mounted on a vibration-isolated horizontal stage. In the negative feedback mode, a bare glass slide was used as an insulating substrate to check the tip geometry.

The fabrication of a nanotip starts with pulling a micrometer-sized Au wire into a glass capillary, as described previously.[15a] Briefly, an annealed 25-µm wire (Goodfellow) was inserted into a borosilicate capillary (1.0-mm o.d., 0.58-mm i.d.), which was fixed in the V groove of the Sutter P-2000/G laser pipet puller. The programs designed to produce Au nanoelectrodes with a desired size and shape were different from those used previously to pull Pt electrodes because of comparatively low melting point of gold. For example, the parameter "heat" which controls the output power of a laser was set somewhat lower for gold (400) than for platinum (500), and the "velocity" parameter value was kept higher for Au (30) than for Pt (15). The larger value of the latter parameter resulted in a lower temperature of the Au wire at the moment when the capillary was pulled.

A pulled capillary with a sealed Au wire was polished using a BV-10 micropipet beveller (Sutter) under video microscopic control. The micromanipulator was used to move the capillary vertically towards the rotating disk to which a 50 nm lapping tape (Precision Surfaces International, Houston, TX) was attached. During polishing, the pipet axis was made exactly

perpendicular to the rotating disk using a plumb bob and a two-axis bubble level. (See ref. 15b for details of the tip/polisher and tip/substrate alignment). Additional fine polishing was done with 50-nm alumina particles placed on the same rotating disk. The polished electrodes were rinsed with water and annealed in the oven at 90 ºC for an hour.

For kinetic measurements by SECM, it is essential to bring the tip very close (the minimum attainable tip/substrate separation distance should be ~0.1*a* or smaller) to the substrate surface. This can be done only if the metal core of the tip is not recessed into the insulating glass and the *RG* is sufficiently small. Unfortunately, repolishing the tip, which may be required to clean it and ensure reproducibility of the results, increases the thickness of the glass sheath and may result is a slight recess of the Au surface. This problem can be avoided by using an aqueous suspension of alumina particles to repolish the tip. The polishing was done by moving the tip inside concentrated suspension (very soft paste) of 50-nm alumina particles in water. Figure 2.1 shows two voltammograms of 1 mM of $FcCH_2OH$ at a 70 nm radius Au tip before (A) and after (B) repolishing it in suspension of 50 nm alumina. A marked improvement in the electrode response is not surprising if one keeps in mind that the tip radius was comparable to that of an average alumina particle. Random collisions of particles with the tip result in gentle and efficient polishing.

SECM apparatus and procedure. A home-built SECM instrument and experimental procedures were described previously.[15a,b] Briefly, the initial approach of the nanotip to the substrate surface was attained by using a z-axis Inchworm motor (EXFO-Burleigh) to move the tip toward the substrate at a relatively slow speed (e.g., 200 nm/s). The motion was stopped instantly when the change in tip current was detected, i.e., at the tip/substrate separation distance equivalent to several tip radii. The final approach was done using a piezo actuator (PI-841, Physik Instrumente, Germany) to move the tip toward the substrate at a very low speed (5 nm/s

to 30 nm/s) and recording the tip current as a function of separation distance. The approach was monitored by a video microscope. A proper tip/substrate alignment was achieved as described in ref. 15b.

To obtain an approach curve, the tip was biased at a potential where the oxidation (or reduction) of the mediator species occurred at a diffusion-controlled rate; the mediator regeneration at the unbiased Au substrate was also diffusion-controlled. For SECM voltammetric experiments, the nanotip was positioned at a suitable distance from the substrate, and its potential was scanned. The corresponding approach curve was used as a distance calibration to determine the tip/substrate distance from the diffusion limiting current. All experiments were carried out at room temperature (23 ± 2 °C) inside a Faraday cage. Steady-state voltammograms were obtained using an EI-400 bipotentiostat (Ensman Instruments, Bloomington, IN) or a BAS 100B electrochemical workstation (Bioanalytical Systems, West Lafayette, IN). The solution containing $Ru(NH_3)_6^{3+}$ was purged with high purity nitrogen for at least 30 min before voltammetric measurements.

2.3 Results and Discussion

Electrode characterization.

Cyclic voltammetry and SECM were used to check that the surface of polished gold nanoelectrodes is flat and not recessed. A steady-state voltammogram of 1 mM ferrocenemethanol (Fig. 2.1A) is fully retraceable and well shaped with a flat diffusion plateau. The tip radius, a = 68 nm was obtained from Eq. (2.1)

$$i_{T,\infty} = 4FDac^* \qquad (2.1)$$

where F is the Faraday constant, $D = 7.8 \times 10^{-6}$ cm^2/s is the diffusion coefficient of $FcCH_2OH$,[15a] and c^* is its concentration in solution. An SECM current vs. distance curve obtained with the

same Au tip approaching an insulating substrate (Fig. 2.1B, symbols) was fitted to the theory for positive feedback (solid line)[27] using the same radius value. The *RG* value (*RG* = 10) was determined from the same current-distance curve, as discussed previously.[15a,27] A high positive feedback current obtained at 60-nm Au tip approaching a conductive substrate (Fig. 2.1C) is indicative of a flat, non-recessed, and well polished tip surface. *RG* = 10 obtained from Figs. 2.1B and 2.1C is typical of the Au tips used in this work. Although a very careful tip/substrate alignment (see Experimental section) was required to attain short separation distances with a relatively large *RG*, we preferred to employ such tips for measurements of fast heterogeneous kinetics because the theory Eq. (2.2) was developed for *RG* = 10.[15a]

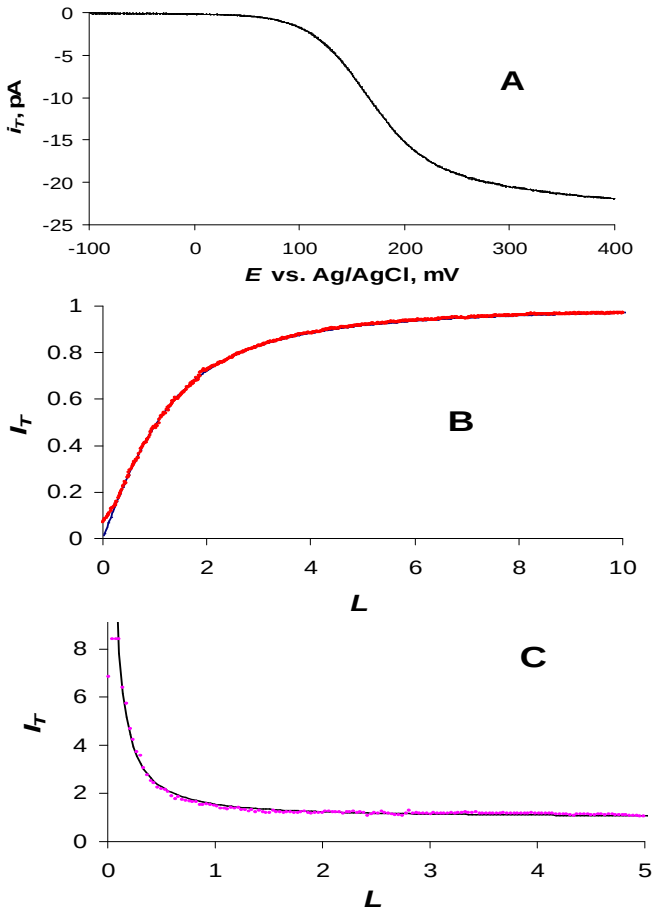

Figure 2.1 Steady state voltammogram (A) and SECM approach curves (B) and (C) obtained at a Au tip in solution containing 1 mM $FcCH_2OH$ and 0.2 M KNO_3. *a* = 68 nm (A) and (B), and 60 nm (C). Theoretical curves (solid lines) were calculated with *RG* = 10 for negative feedback (B) and diffusion-controlled positive feedback (C);[27] symbols are experimental data. The current is normalized by the value measured in the bulk solution. The tip approached the substrate with a 5 nm/s (B) and 10 nm/s (C) speed. The potential sweep rate was *v* = 50 mV/s (A).

Kinetics of ET Reactions at Au Nanoelectrodes. Kinetic parameters of $FcCH_2OH$ oxidation in 0.2 M NaCl (6.8 ± 0.7 cm/s; α = 0.42 ± 0.03) were extracted in Ref. 15a from a number of voltammograms obtained at Pt nanoelectrodes of different radii (from 25 nm to 290 nm). Fig. 2.2 shows a family of voltammograms of the same ET reaction obtained with a 109 nm Au tip positioned at different distances from the conductive, Au film substrate. k^o and the transfer coefficient (α) were obtained by fitting the voltammograms to Eq. (2.2):[15a]

$$I_T(E,L) = \frac{0.78377}{L(\theta + 1/\kappa)} + \frac{0.68 + 0.3315exp(-1.0672/L)}{\theta\left[1 + \frac{\pi}{\kappa\theta}\frac{2\kappa\theta + 3\pi}{4\kappa\theta + 3\pi^2}\right]} \qquad (2.2)$$

where $L = d/a$, E is the tip potential, $\kappa = \pi\lambda\exp\text{-}\alpha F(E\text{-}E^{\circ\prime})/RT/(4\ I_T^c)$, $\lambda = k^{\circ}a/D$, $\theta = 1 + \exp F(E - E^{\circ\prime})/RTD_O/D_R$, $E^{\circ\prime}$ is the formal potential, R is the gas constant, T is the temperature, D_O and D_R are the diffusion coefficients of oxidized and reduced forms of redox species ($D_O = D_R = D$ is assumed below), and I_T^c is the normalized diffusion limiting tip current for the same L at a conductive substrate:

$$I_T^c = 0.68 + 0.78377/L + 0.3315\exp(-1.0672/L) \qquad (2.3)$$

The tip current $I_T(E,L)$ in Eq. (2.2) is normalized by the steady-state diffusion limiting current to a microdisk electrode, $i_{T,\infty}$, which given by Eq. (2.1) for a sufficiently large RG (e.g., ~10).

Kinetic parameters extracted from the series of SECM voltammograms obtained at five different Au tips are summarized in Table 2.1. As discussed previously,[15a,19] the upper limit for the measurable standard rare constant can be given in terms of the dimensionless kinetic parameter $\lambda' = k^{\circ}d/D = Lk^{\circ}a/D$. The tip voltammogram is essentially reversible if $\lambda' \gtrsim 10$. When the tip is far from the substrate, the condition of reversibility is $\lambda = k^{\circ}a/D \gtrsim 10$. Thus, the kinetic parameters in Table 2.1 were obtained only from voltammograms that yielded $\lambda' < 10$ (or $\lambda < 10$

at $L >> 1$). Similarly to the results obtained previously at Pt nanoelectrodes, there is no apparent correlation between the determined kinetic parameters and a or d values. Essentially the same formal potential value (within ± 5 mV) was found from different voltammograms obtained at the same tip. The variations between $E^{o\prime}$ values obtained with different tips are due to the slow shift in the coated-wire reference potential (on the time scale of several days). The mean values of the kinetic parameters from Table 2.1 are $k° = 8 \pm 1$ cm/s and $\alpha = 0.42 \pm 0.06$. (Here and below, the uncertainties are 95% confidence intervals). The determined α value is the same as the one found for $FcCH_2OH$ oxidation at Pt nanoelectrodes, and the $k°$ value is slightly higher than the one in ref. 15a (6.8 ± 0.7 cm/s). This difference is within the range of our experimental uncertainty, and a slightly larger rate constant measured at Au electrodes indicates that a higher density of electronic states in Pt is not a factor here. No statistically significant difference was

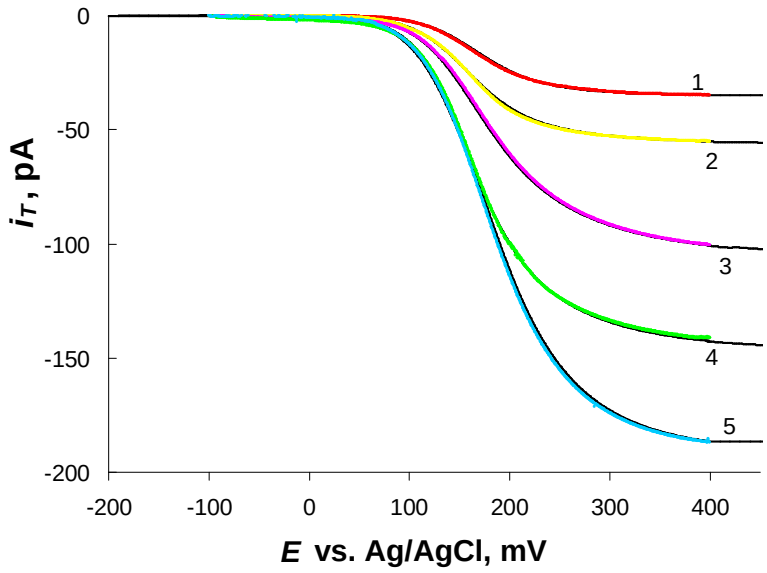

Figure 2.2. Experimental steady state voltammograms of 1 mM $FcCH_2OH$ obtained at different separation distances between the 109-nm Au tip and Au substrate. $d = \infty$ (1), 72 nm (2), 35 nm (3), 31nm (4), and 21 nm (5). $v = 50$ mV/s.

also found between kinetic parameters of the oxidation of Fc in acetonitrile measured at ten Au nanoelectrodes ($k°$ = 8.0 ± 0.5 cm/s; α = 0.44 ± 0.03) and those obtained previously[15a] at Pt tips ($k°$ = 8.4 ± 0.2 cm/s; α = 0.47 ± 0.02). These findings indicate that the oxidations of $FcCH_2OH$ in water and Fc in acetonitrile are adiabatic processes.[22]

Table 2.1. Kinetic parameters of $FcCH_2OH$ oxidation at Au nanoelectrodes in 0.2 M NaCl

a, nm*	L	$k°$, cm/s	α	$E°'$	λ' or λ
153	∞	reversible			
153	0.86	reversible			
153	0.42	9.0	0.31	153	7.4
153	0.34	10.5	0.30	151	7.0
153	0.21	9.8	0.30	142	4.0
109	∞	reversible			
109	0.66	7.3	0.32	172	6.8
109	0.32	5.5	0.33	168	2.5
109	0.28	8.9	0.32	161	3.5
109	0.19	8.3	0.41	162	2.3
65	∞	5.3	0.57	131	4.5
65	0.6	6.8	0.51	121	3.5
57	∞	6.7	0.51	192	4.8
57	1.5	7.5	0.49	196	8.2
57	0.71	7.8	0.49	190	4.0
55	∞	8.2	0.45	138	6.3
55	2.15	9.1	0.57	134	5.2
55	1.2	11.6	0.48	135	5.9

Similar approach was used to measure kinetic parameters of the reduction of $Ru(NH_3)_6^{3+}$ in 0.5 M KCl (Table 2.2). Like it was found above for $FcCH_2OH$, the mean transfer coefficient value for $Ru(NH_3)_6^{3+}$ reduction at Au electrodes ($\alpha = 0.45 \pm 0.09$) is exactly the same as at Pt.[15a] However, the mean rate constant value at Au surfaces ($k° = 13._5 \pm 2$ cm/s) is lower than that measured at Pt tips in ref. 15a (17.0 ± 0.9 cm/s). The difference between these two mean values is statistically significant: using a *t* test[28] at the 95% confidence level, one can find $t_{calc} = 3.65$, which is larger than $t_{table} = 2.1$. The dependence of the rate of $Ru(NH_3)_6^{3+}$ reduction on the nature of the metal surface points to some degree of non-adiabaticity, however, the ratio, $k°_{Pt}/k°_{Au} = 1.26$ is smaller than the 1.8 value expected for a completely non-adiabatic reaction.

Table 2.2. Kinetic parameters of $Ru(NH_3)_6^{3+}$ reduction at Au nanoelectrodes (solution contained 2 mM $Ru(NH_3)_6^{3+}$ and 0.5 M KCl)

a, nm*	*L*	*k*°, cm/s	α	*E*°′	λ
134	∞	reversible			
134	0.62	reversible			
134	0.53	reversible			
134	0.40	10.5	0.3	151	8.4
134	0.36	11.4	0.30	142	8.2
98	∞	reversible			
98	0.31	13.3	0.51	131	6.0
98	0.25	15.0	0.51	133	5.4
98	0.18	18.4	0.49	127	4.9
84	∞	reversible			
84	0.26	19.8	0.63	162	6.5
84	0.20	12.5	0.67	156	7.1
62	∞	reversible			

62	0.87	9.1	0.35	134	8
62	0.67	11.6	0.33	135	5

The above finding is different from the results of Iwasita *et al.*,[25] who measured very similar rate constant values for the $Ru(NH_3)_6^{3+/2+}$ couple at different metallic electrodes and concluded that the ET reaction is fully adiabatic. However, the supporting electrolyte in ref. 25 was 1 M KF. It was also suggested that the kinetics of $Ru(NH_3)_6^{3+}$ reduction strongly depends on the nature of the supporting electrolyte, and the $k°$ value greatly increases in the presence of high concentration of chloride.[5] Therefore, we determined the kinetics of this reaction at both Pt and Au nanoelectrodes in 1 M KF. The results presented in Table 2.3 can be summarized as follows: $k° = 11.9 \pm 0.5$ cm/s, $\alpha = 0.40 \pm 0.05$ (at Pt) and $k° = 9.3_5 \pm 0.4$ cm/s, $\alpha = 0.42 \pm 0.03$ (at Au). Similarly to the results obtained in KCl, there is no significant difference between the transfer coefficient values measured at Au and Pt electrodes. For both Au and Pt, the mean $k°$ measured in KF is somewhat (~30%) lower than the corresponding values in KCl. Moreover, in KF the $k°_{Pt}/k°_{Au}$ ratio is 1.27, i.e., very close to the 1.26 value obtained in KCl. In either solution, the reduction of $Ru(NH_3)_6^{3+}$ is not completely adiabatic. The discrepancy between this finding and the previously reported results[25] is probably due to a very high $k°$ value, which was hard to accurately measure at macroscopic electrodes back in 1985.

One should notice that the self-exchange rate constant measured for $Ru(NH_3)_6^{3+/2+}$ is significantly (~3 orders of magnitude) lower than that obtained for the ferrocene couple.[29,30] This data and a higher degree of adiabaticity of $FcCH_2OH$ oxidation discussed above are at variance with the larger k^o values measured for $Ru(NH_3)_6^{3+}$ reduction at both Pt and Au electrodes. A plausible explanation is that the k^o of $Ru(NH_3)_6^{3+}$ reduction is enhanced by the

diffuse double layer effect (Frumkin correction), which can be expressed as $k_t = k^o exp((z-\alpha)F\varphi_2/RT)$, where z is the ionic charge and φ_2 is the potential at the outer Helmholtz plane.[31] Although it is hard to quantitatively evaluate φ_2 and the magnitude of the Frumkin correction at solid nanoelectrodes, this correction should be larger for $Ru(NH_3)_6^{3+}$ (z =3) than for a neutral $FcCH_2OH$ species. Moreover, $Ru(NH_3)_6^{3+/2+}$ is the only redox couple for which the rate constant measured either at Au or at Pt nanoelectrodes was significantly higher than the values obtained previously at macroscopic electrodes. This observation agrees with the theoretical prediction that a double layer effect on heterogeneous kinetics may be stronger at nanoelectrodes[32] (and nanoparticles[33]) than at macroscopic electrodes, especially for multicharged ions.[34]

Table 2.3. Kinetic parameters of the reduction of 2 mM $Ru(NH_3)_6^{3+}$ at Pt and Au nanoelectrodes in 1 M KF

electrode	a, nm*	L	$k°$, cm/s	α	$E°'$	λ
Au	70	∞	reversible			
Au	70	1.1	reversible			
Au	70	0.61	9.3	0.34	-282	6.1
Au	70	0.42	9.1	0.38	-284	4.1
Au	70	0.30	9.6	0.4	-280	3.1
Au	56	∞	9.5	0.48	-282	8.2
Au	56	0.98	10.2	0.46	-278	8.6
Au	56	0.58	9.0	0.38	-276	4.5
Au	56	0.45	9.8	0.42	-278	3.8
Au	56	0.36	8.4	0.46	-280	2.6
Pt	77	∞	reversible			
Pt	77	0.98	reversible			

Pt	77	0.58	11.8	0.37	-272	8.1
Pt	77	0.40	11.4	0.38	-268	5.4
Pt	77	0.21	12.9	0.37	-274	3.2
Pt	62	∞	reversible			
Pt	62	0.78	11.6	0.52	-268	8.6
Pt	62	0.56	11.2	0.38	-258	5.98
Pt	62	0.30	12.6	0.37	-259	3.6

Other ET Reactions. The kinetics of several other fast outer-sphere redox couples at Au and Pt nanoelectrodes were investigated. A few of them exhibited near-ideal voltammetric responses at both types of nanoelectrodes. A typical example is the rapid oxidation of tetrathiafulvalene in 1,2-dichloroethane, whose kinetic parameters are essentially the same at Pt ($k°$ = 8.8 ± 0.4 cm/s, $\alpha = 0.37_5 \pm 0.02$) and Au ($k°$ = 9.0 ± 0.4 cm/s, $\alpha = 0.39_5 \pm 0.02$) surfaces (Table 2.4). Similar results were obtained for two other redox species, i.e., TEMPO in acetonitrile and methylphenothiazine in 1,2-dichloroethane (data not shown).

Another group of ET reactions appear to be strongly surface-dependent. A typical example is the reduction of 7,7,8,8-tetracyanoquinodimethane (TCNQ) in acetonitrile. At Pt nanoelectrodes, this process yielded essentially ideal voltammetric responses, and the determined $k°$ = 1.1 ± 0.04 cm/s[15a] was relatively slow in contrast to the very fast self-exchange rate constant of TCNQ (4×10^9 $M^{-1}s^{-1}$ [35]). One could expect this ET to be non-adiabatic and to show significant differences between the rates measured at Pt and Au. However, the voltammograms of TCNQ at Au nanoelectrodes were poorly shaped, and no quantitative kinetic analysis was possible. Similarly, we were unable to obtain well shaped voltammograms at Au nanoelectrodes for $Ru(bpy)_3^{3+/2+}$, $Fe(CN)_6^{3-/4-}$, and $Fe^{3+/2+}$ couples.

Table 2.4. Kinetic parameters of the oxidation of tetrathiafulvalene in 1,2-dichloroethane at Pt and Au nanoelectrodes (solution contained 2 mM tetrathiafulvalene and 0.1 M tetrabutylammonium perchlorate)

electrode	*a*, nm*	*L*	*k*°, cm/s	α	*E*°′	λ
Pt	72	∞	8.6	0.38	352	7.2
Pt	72	0.46	8.8	0.34	354	3.4
Pt	72	0.25	9.1	0.42	354	1.9
Pt	72	0.17	8.4	0.38	350	1.2
Pt	65	∞	8.2	0.41	360	6.2
Pt	65	0.78	8.7	0.35	358	5.1
Pt	65	0.44	8.4	0.36	360	2.8
Pt	65	0.28	9.9	0.35	360	2.1
Au	68	∞	9.4	0.36	348	7.4
Au	68	0.82	8.0	0.41	348	5.2
Au	68	0.45	8.7	0.38	346	3.1
Au	68	0.25	8.6	0.38	345	1.7
Au	54	∞	9.9	0.38	350	6.2
Au	54	0.9	9.7	0.38	352	5.5
Au	54	0.68	8.2	0.36	350	3.5
Au	54	0.32	9.0	0.40	349	1.8
Au	43	∞	8.6	0.45	364	4.3
Au	43	0.87	9.4	0.41	358	4.1
Au	43	0.55	9.1	0.45	352	2.5

2.4 Conclusion

The flat, polished Au nanoelectrodes were prepared and characterized by SECM and voltammetry. These probes were used to measure the kinetic parameters of several rapid heterogeneous ET reactions by steady-state SECM voltammetry. While the mass transfer rate was changed by varying the tip radius and the tip/substrate separation distance, the determined kinetic parameters were essentially independent of both *a* and *d*. For several species including Fc, $FcCH_2OH$, and tetrathiafulvalene the standard rate constants and transfer coefficient values measured at Au tips were very similar to those obtained at Pt nanoelectrodes, as expected for adiabatic ET reactions.[22] However, the standard rate constants of $Ru(NH_3)_6^{3+}$ reduction in KCl and KF solutions at Au electrodes were found to be lower than those obtained at Pt electrodes, indicating that this reaction is not fully adiabatic.

Chapter III

Nanoscale Imaging of Surface Topography and Reactivity with the SECM

3.1 Introduction

The capacity for acquiring spatially resolved chemical information makes SECM a powerful tool for visualizing microstructures and studying surface processes.[1] A wide range of the reported applications include mapping local heterogeneous kinetics,[2] rapid screening of electrocatalysts,[3] studies of charge-transfer processes at liquid interfaces,[1,4] and in biological cells,[5] investigations of corrosion[6] and crystal dissolution.[7] Various substrates from enzyme-patterned molecular films[8] to diamond electrodes[9] and semiconductor surfaces[10] to living cells[11] have been imaged by SECM. Among most recent applications are visualization of 1-D conductors,[12] proteins[13] and fingerprints on surfaces.[14]

Among several modes of the SECM operation, the feedback mode offers important advantages for topographic and reaction rate imaging.[1] These include high spatial resolution due to the minimal diffusional broadening of the image and high sensitivity to the surface reactivity. Feedback mode SECM images are obtained by scanning the tip above the substrate and recording the variations in the tip current (constant-height mode) or z-coordinate (constant-current mode) in solution containing either oxidized or reduced form of a redox mediator. The tip current is produced by reduction (or oxidation) of the mediator species at its surface. If the mediator species is regenerated at the conductive substrate surface at the diffusion-controlled rate, such a process produces an enhancement in the tip current (positive feedback). In the absence of the mediator regeneration, an insulating substrate blocks the diffusion of redox species to the tip, and so the tip current (i_T) decreases with decreasing d (negative feedback).

The strong i_T vs. d dependence under both positive and negative feedback conditions constitutes the basis for topographic SECM imaging. If the mediator regeneration at the substrate is kinetically controlled, a feedback mode SECM image provides information of the spatial distribution of the reaction rate at the substrate.[15a]

Most SECM images reported in the literature were obtained with micrometer-size tips, and therefore provided micrometer-scale resolution.[1,16] The previously available nanotips were shaped either as a cone or a spherical cap.[17] Conical and spherical tips have been employed for generation/collection mode imaging,[18] imaging "in humid air",[16,19] and for electrochemical imaging with combined SECM-AFM,[20] but low feedback responses make them less suitable for the feedback mode experiments. Here, we report the use of polishable disk-type nanotips[21a] for feedback-mode imaging of substrate topography and reactivity. Similar probes have recently been employed for nanoscale imaging of biological cells.[11] However, it was difficult to interpret such images and evaluate their validity. In this work, the spatial resolution and other aspects of nanoscale SECM experiments will be characterized by imaging well defined samples ranging from recordable compact disks (CDs) to computer chips.

Another type of probes potentially suitable for the feedback mode imaging is nanopipettes.[22a] A pipette can be filled with a solvent immiscible with the outer solution and used as an SECM tip.[22b] The tip current is produced by the transfer of an ion across the liquid/liquid interface e.g., from water to 1,2-dichloroethane (DCE) inside the pipette. This current is limited by diffusion of the transferable ion in the outer solution. It decreases when the tip is brought close to a solid substrate, which blocks the diffusion to the pipette orifice (negative feedback). The theory developed for the ion transfer (IT) feedback mode is similar to the conventional SECM feedback theory, and the quantitative agreement between theoretical and

experimental current vs. distance curves was demonstrated for nanopipette tips.[22c] Here, we present the first example of high resolution topographic imaging based on the negative IT feedback.

3.2 Experimental Section

Chemicals. Ferrocenemethanol ($FcCH_2OH$), LiCl and KCl purchased from Aldrich, tetraethylammonium chloride (TEACl), chlorotrimethylsilane, and 1,2-dichloroethane (DCE) from Sigma were used as received. Solutions of $FcCH_2OH$ and KCl were prepared daily and buffered to pH 4 with 20 mM acetic acid (Baker). Hexaammineruthenium (III) chloride and ammonium hexachloroiridate (IV) were purchased from Strem Chemicals and used without further purification. Ferrocene (Fc; 98%, Aldrich) was sublimed twice. Tetrabutylammonium tetrakis(4-chlorophenyl)borate (TBATPBCl) was prepared by metathesis of KTPBCl and TBACl, as described previously.[23] The ionic liquid, 1-methyl-3-octylimidazolium-bis(tetrafluoromethylsulfonyl)imide ($C_8mimC_1C_1N$), was generously provided by Prof. Takashi Kakiuchi (University of Kyoto, Japan). All aqueous solutions were prepared from deionized water (Milli-Q, Millipore Corp).

Substrate preparation. Recordable compact disks (CDs) were stripped of their protective layer by dipping them into concentrated nitric acid for several minutes until the layer peeled off completely. This bath also removed the metallic layer from aluminum-coated CDs. CDs were then rinsed with deionized water. Gold CDs were thoroughly cleaned by dipping them in a concentrated ethanol solution of potassium hydroxide for 5 minutes and then rinsed several times with deionized water. Electronic microcircuits (wafers and microchips) were obtained as a gift from Ms. Mary Westermann (IBM Corporation, East Fishkill, NY). A portion of the wafer that contained the area of interest was carefully cut using a glass cutter and glued to a glass microscope slide.

Electrodes and Electrochemical Cells. Polished Pt working electrodes (50 – 200 nm radius) were prepared by pulling micrometer-sized Pt wires into a glass capillaries and polishing under video microscopic control, and characterized as described previously.[11,21] The overall success rate for the tip preparation is ~80%. A two-electrode setup was used with a 0.25-mm-diameter Ag wire coated with AgCl serving as a reference electrode. When $(NH_4)_2IrCl_6$ was used as a redox mediator, a commercial glass-enclosed Ag/AgCl reference electrode was employed to prevent direct contact of Ag with the oxidizing hexachloroiridate (IV) solution. CD substrates were either glued with Torr Seal epoxy (Varian, Lexington, MA) to the bottom of a glass cell or a rectangular glass cell was built on the substrate itself by attaching four pieces of glass slide to it. In some experiments, imaging was carried out in a drop of aqueous solution placed on a hydrophobic substrate surface, and the Ag/AgCl reference electrode was inserted inside the drop. The substrate was secured onto (but kept electrically insulated from) a steel SECM stage with the help of strong magnets.

The nanopipettes were made from quartz capillaries (length of 10 cm, OD/ID = 1.0/0.70 mm; Sutter Instrument Co., Novato, CA) using a laser-based pipette puller (P-2000, Sutter Instrument Co.), as described previously.[22] The pipettes were filled with organic solution from the rear, using a small (10-25 μL) syringe. A Ag/AgTPBCl ($TPBCl^-$ is tetrakis(4-chloro-phenyl)borate) reference was inserted into each pipette from the rear. The inner glass wall of a pipette was silanized to render it hydrophobic. This was done by dipping the pipette tip into chlorotrimethylsilane for ~5-7 seconds. This was crucial because the external aqueous solution gets drawn inside a pipette if its inner surface is hydrophilic. Before imaging, the pipette radius was evaluated by steady-state voltammetry and the stability of its response was checked by immersing it into a 0.6 mM aqueous solution of tetraethylammonium chloride (TEACl) and

passing the diffusion limiting current of TEA^+ transfer. The pipette was deemed suitable for imaging if the current changed by <3% during 20 min.

SECM instrument and procedures. The schematic diagram of our home-built SECM instrument is shown in Fig. 3.1. As described previously,[11] the tip current was measured and its potential was controlled by the EI-400 four-electrode potentiostat (Cypress Systems). The SECM stage was bolted onto a vibration insulated optical table (Newport).

A National Instrument data acquisition card DT-EZ installed on a Dimension 9200 (Dell) computer that was used to operate the EI-400 potentiostat. The substrate was always unbiased. The same computer also handled the tip positioning via an 8200 Inchworm motor controller

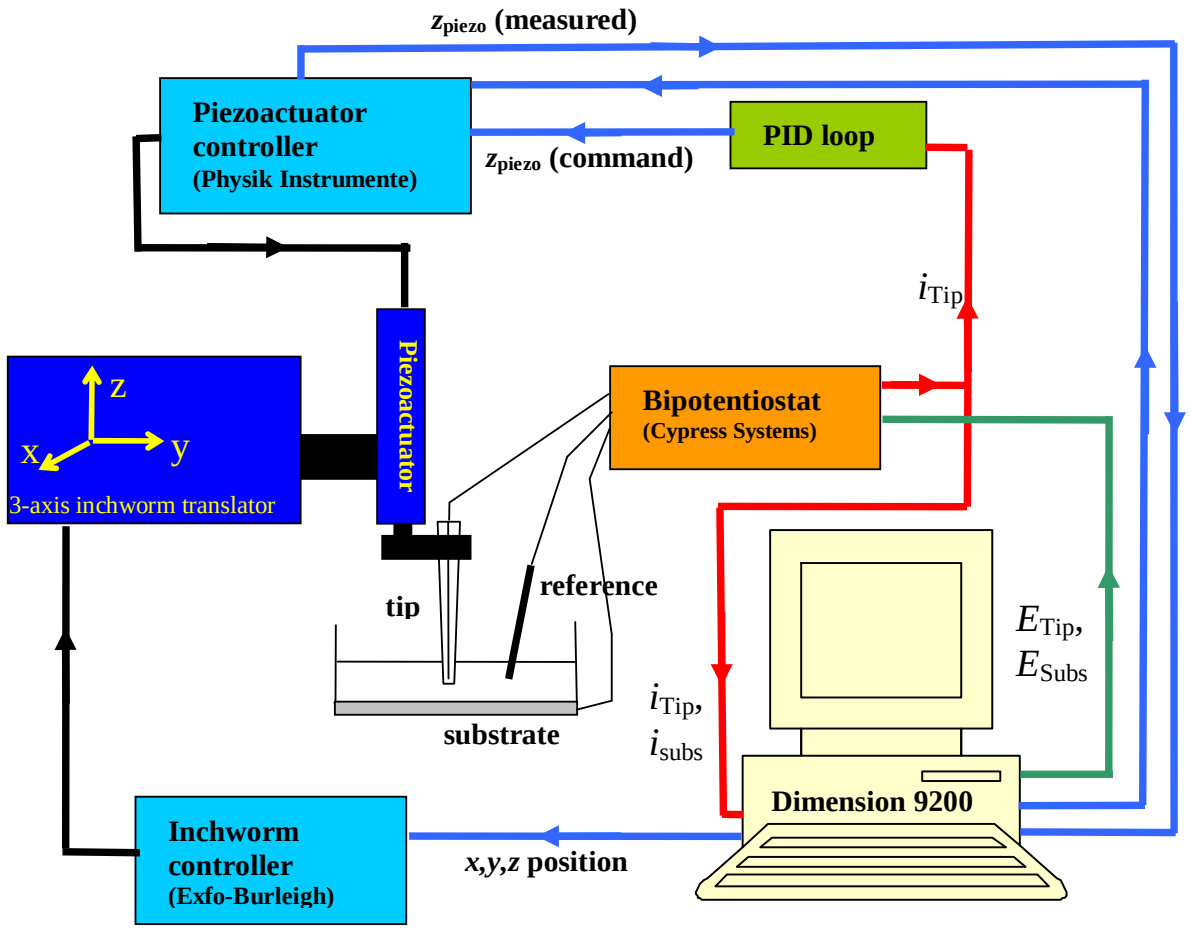

Figure 3.1. Scheme of the SECM instrument with a feedback PID loop.

(EXFO-Burleigh) and three motors (TSE-820) with 20 nm resolution optical encoders in a closed loop. This configuration was used for constant height imaging. For higher z-axis position resolution (0.1 nm) during constant current imaging, a PI-843.60 piezoactuator (Physik Instrumente) controlled by an E-500 position controller (Physik Instrumente) was used. The probe was attached to the moving part of the piezoactuator and the static part of the piezoactuator was fastened onto the 3D inchworm stage. During constant current imaging, the computer could read the tip position via the E-500 controller.

A home-built digital proportional-integral-derivative (PID) loop controller using tip current as input signal and tip position as output signal was constructed to control the vertical position of the tip during constant current imaging. The input signal (i.e., the voltage analog of the tip current) was digitized using a 16 bit analog-to-digital converter (ADS8505, Texas Instruments), then processed with a microcontroller (PIC24HJ256GP610, Microchip), and an output, z_{piezo}, was generated with a 16 bit digital-to-analog converter (DAC8820, Texas Instruments). The output of the PID loop was fed to the analog input of the E-500. The input signal was filtered by summing up a number of samples over a 16.7 ms period (60 Hz). This procedure nearly completely eliminates 60 Hz noise coming from the power line. The bandwidth of the feedback loop was 60 Hz.

To monitor the initial approach of the SECM tip to the substrate, we used binocular lenses focused a few tens of microns above the substrate surface. The tip was moved slowly toward the substrate until it appeared in focus. During the final approach, the tip was brought closer to the substrate while monitoring the current, as described previously.[21] All experiments were carried out at room temperature (23 ± 2 °C) inside a Faraday cage.

3.3 Results and Discussion

Imaging compact disks in aqueous solutions. Once chemically stripped from its protective, metallic, and dye layers, the surface of a rewritable aluminum CD exhibits one spiral groove, which microscopically appears as a series of ~1-μm spaced parallel stripes (Fig. 3.2A). Fig. 3.2B shows an SECM image of a 7 μm × 7 μm portion of CD surface obtained with a 140-nm-radius Pt electrode with RG = 10 ($RG = rg/a$, where rg is the radius of the insulating sheath, and a is the Pt disk radius) in a 5 mM ammonium hexachloroirridate(IV) aqueous solution. The tip was scanned in a horizontal plane above the substrate at a scan rate v = 1 μm/s to obtain a constant-height SECM image. The lateral resolution, which is determined by the tip radius[1] (i.e., ~140 nm), was sufficiently high to clearly image the CD surface pattern. A current vs. distance curve (Fig. 3.2C) obtained with the same tip approaching the insulating CD surface exhibits negative feedback. The theoretical $i_T - d$ curve in Fig. 3.2C (solid line) was obtained from Eq. (3.1)[22b]

$$i_T = i_{T,\infty}\left(0.7449932 + \frac{0.7582943}{d/a} + 0.2353042\exp\left(\frac{-1.683087}{d/a}\right)\right) \qquad (3.1)$$

where $i_{T,\infty}$ is the tip current in the bulk solution (far from the substrate) and a is the tip radius. The experimental curve (symbols) fits the theory for $d \gtrsim 50$ nm and deviates from it at shorter distances. This can be expected because the width of the disk groove is comparable to the tip diameter and its depth is of the order of 50 nm.

Because of the non-linear relationship between the tip current and the tip/substrate distance Eq. (3.1), the constant-height SECM image does not directly represent the topography of the substrate. Using Eq. (3.1), the current map shown in Fig. 3.2B was converted to the topographic image (i.e., the dependence of the tip/substrate separation distance vs. the tip

position). One should note that the tilt angle (~0.7º; the inclination of ~80 nm over a 7 µm distance is due to the imperfect tip/substrate alignment in *y* direction) is reversed in Fig. 3.2D as compared to that in

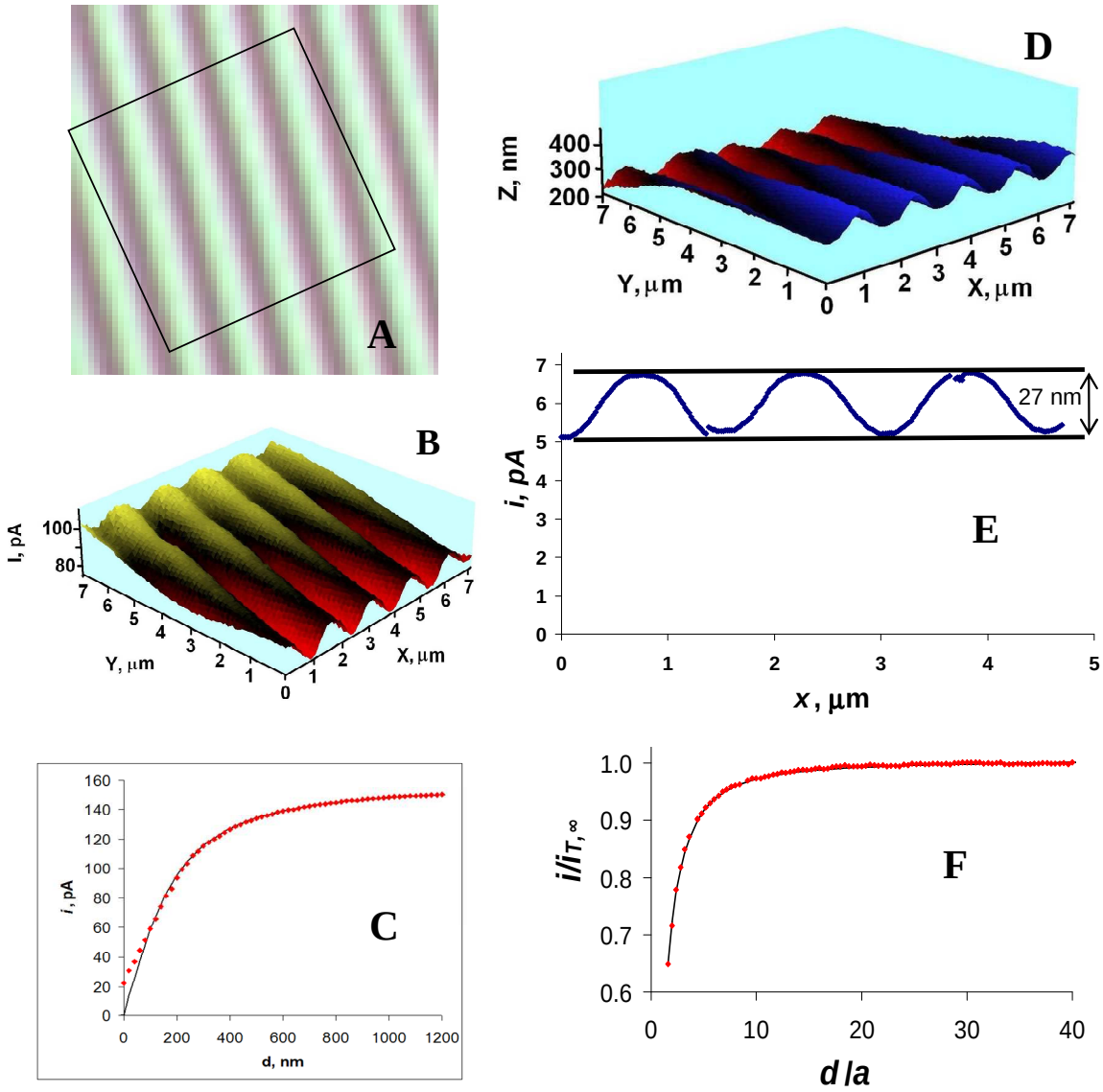

Figure 2. (A) Optical micrograph of CD surface. The 7 µm × 7 µm imaged area is indicated by the black square. (B) SECM image of a 7 µm × 7 µm portion of CD surface obtained with a 140 nm radius Pt electrode. ν = 1 µm/s. (C) and (F) Experimental (symbols) and theoretical (solid line; computed from Eq. 1) current - distance curves for 140 nm (C) and 50 nm (F) tips approaching the CD surface. (D) Topographical image remapped from the constant height SECM image in panel B. (E) Lateral line scan obtained with a 50 nm tip. Small current discontinuities are an artifact caused by piezo clicks. Aqueous solutions contained 250 mM KCl and either 5 mM $(NH_4)_2IrCl_6$ (B) – (D) or 1 mM $FcCH_2OH$ (E), (F). The tip potential was 100 mM (B) – (D) or 500 mV (E), (F) vs. Ag/AgCl reference.

Fig. 3.2B. The ridges appearing on the current map (Fig. 3.2B) are also inverted and look like valleys in Fig. 3.2D. The remapped topographic image eliminates the $i_T - d$ non-linearity, so that the ridge/valley distance appears essentially constant over the entire image.

Higher resolution and more detailed topographic information can be obtained by using a smaller tip. A line scan of the same CD (Fig. 3.2E) was obtained with a 50-nm tip. Using the corresponding current-distance curve (Fig. 3.2F) for distance calibration, one can determine the depth of the groove to be 27 nm.

The metallic layer in old rewritable CDs ("gold CDs") was Au rather than Al. The nitric acid treatment in this case strips the protective coating off, but leaves a thin gold layer intact. The exposed gold surface was previously used as a platform for sensor fabrication.[24] Fig. 3.3A shows an AFM image of a 5 μm × 5 μm portion of the gold CD surface.[24] The image reveals ~1.2-μm-wide plateaus separated by ~300-nm-wide valleys. The SECM feedback obtained at a gold CD substrate (Fig. 3.3B) is positive due to the electrochemical activity of gold.

The constant-height SECM image of a 2.5 μm × 7 μm portion of the Au CD surface (Fig. 3.3C) was obtained with a 140-nm-radius Pt electrode in a 1 mM $FcCH_2OH$ aqueous solution. This image clearly reproduces the plateau/valley surface topography visualized by AFM (Fig. 3.3A). However, on top of the well-defined CD pattern one can see significant local variations in the tip current. These variations could not be caused by topographic features of the CD surface because the nanoscale flatness of Au plateaus is evident from the AFM image. Instead, they are due to the non-uniform electrochemical reactivity of the grainy Au film. Unlike vapor-deposited Au films on glass, whose electrochemical reactivity is uniform and sufficiently high to yield

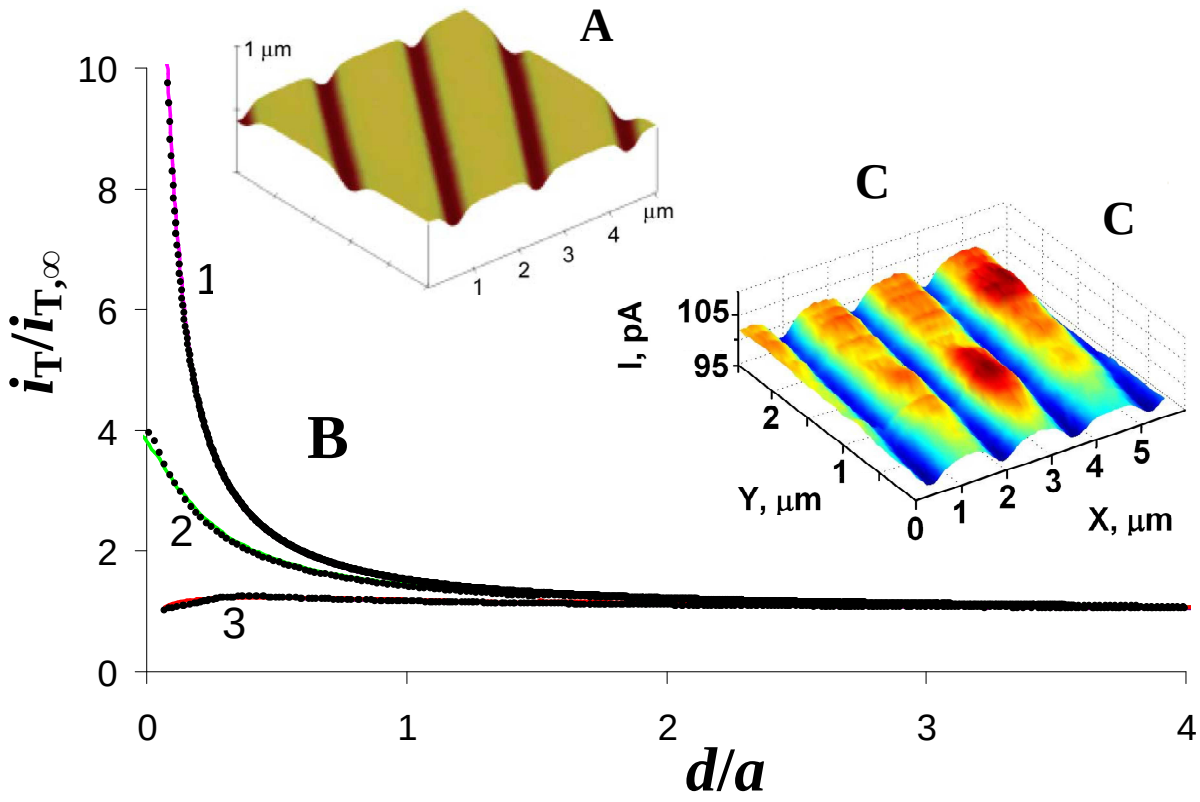

Figure 3.3. (A) AFM image of a 5 μm × 5 μm portion of Au CD surface.[24] (B) Experimental (symbols) and theoretical[25] (solid lines) current-distance curves for different SECM tips approaching a gold CD substrate. The tip radius was 12.5 μm (1), 1 μm (2), and 150 nm (3). (C) Constant-height SECM image of a 2.5 μm × 7 μm portion of gold CD surface obtained with a 140 nm Pt tip. v = 300 nm/s. (B, C) Solution contained 1 mM $FcCH_2OH$ and 250 mM KCl and was buffered with acetic acid to pH = 4. The tip potential was 500 mV vs. Ag/AgCl.

diffusion-controlled SECM feedback at any tip size (e.g., $a \geq 13$ nm[21a]), the finite heterogeneous kinetics can be measured at the gold CD surface using sufficiently small SECM probes. The i_T vs. d curves in Fig. 3.3B were obtained with three tips of different radii. With a large tip (a = 12.5 μm; curve 1), the process is diffusion controlled, and the corresponding current-distance curve fits well the theory for the pure positive feedback (solid pink curve calculated from Eq. (8) in ref. 22b). SECM images of gold CDs obtained with a tip of this size (not shown) do not

contain any features associated with non-uniform surface reactivity. At a smaller tip (e.g., a = 1 µm; curve 2), the higher mass-transfer coefficient[1] results in the mixed diffusion/kinetic control of the mediator regeneration at the substrate, which corresponds to the lower magnitude of the positive feedback. The apparent heterogeneous rate constant found from the fit of the experimental approach curve to the theory (solid green curve calculated from Eq. (6) in ref. 25) was k = 0.45 cm/s. A similar rate constant value, k = 0.50 cm/s was obtained with a much smaller tip (a = 150 nm; curve 3). This value corresponds to the local rate of the mediator regeneration at the microscopic portion of the CD surface facing the tip electrode. Fig 3.3C presents a nanoscale map of the electrochemical reactivity.

Imaging in ionic liquid. All aforementioned images were obtained in aqueous solutions. However, various applications may require SECM imaging to be done in non-aqueous media, e.g., in ionic liquids whose use as solvents in electrochemical systems is on the rise.[26] Although the SECM has been employed in ionic liquids,[27] a major challenge in imaging experiments is slow diffusion rate in these viscous media. The time required for the diffusion-controlled current flowing at a disk electrode to reach the steady state can be roughly estimated as $t_{ss} \cong 50a^2/D$,[28] where D is the diffusion coefficient of redox species in solution. In an aqueous solution, D is ~10^{-5} cm^2/s, and t_{ss} is ~0.05s for a 1 µm-radius tip. Such a tip can be scanned over the substrate surface at a reasonably high speed (a few µm/s) without significant deviations from the steady state. In contrast a typical D value in a moderately viscous ionic liquid (like $C_8mimC_1C_1N$ used in our experiments) is ~10^{-7} cm^2/s, and so t_{ss} ~ 5s (for a 1 µm-radius tip) is too large for feedback mode SECM imaging. This problem can be overcome by using smaller tips; e.g., under the same experimental conditions, t_{ss} is ~0.05s for a = 100 nm. Fig. 3.4 shows a constant-height SECM image obtained with a 190 nm Pt tip in $C_8mimC_1C_1N$ containing 50 mM Fc. v = 500 nm/s is

within the range of scan rates employed for imaging in aqueous solutions (cf. Figs. 3.2B and 3.3C). The surface pattern is essentially identical to that in Fig. 3.3 demonstrating that high viscosity of $C_8mimC_1C_1N$ does not affect the SECM image. A portion of the CD surface imaged in Fig. 3.4 exhibited relatively uniform reactivity—only minor variations can be detected. In other images obtained in $C_8mimC_1C_1N$ (not shown), larger local variations in surface reactivity were evident.

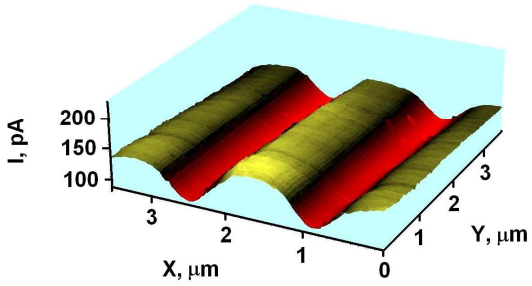

Figure 3.4. Constant-height SECM image of the 3.5 ?m × 3.5 ?m portion of the gold CD surface obtained with a 190 nm Pt tip in ionic liquid. $C_8mimC_1C_1N$ solution contained 50 mM Fc. The lateral scan rate was 500 nm/s.

Microcircuit imaging. Microcircuits are generally built on silicon wafers by locally diffusing doping species, selectively etching parts of the wafer, and electrodepositing copper or aluminum interconnects. Computer microchips and wafers possessing very rough surfaces with small, sharp features are much harder to image than CDs whose surfaces exhibits relatively flat, regular patterns. The first microcircuit substrate used in our imaging experiments was an erasable programmable read-only memory (EPROM) of a Motorola 68HC05 chip containing micrometer-sized features. To match an SECM image with an optical picture of the substrate, one has to obtain an electrochemical map of a relatively large (i.e., tens of microns) area. Constant-height

imaging of a large area with a nanotip scanned laterally in the x-y plane above the substrate is not straightforward because of the practically unavoidable small (e.g., ~0.7º in Fig. 3.2B) tip/substrate misalignment. If the lateral scan length is incomparably larger than *a*, the tip/substrate separation distance changes significantly, and the tip is likely to hit one of the taller surface features of the microcircuit. By keeping the tip current constant (constant-current mode; if the feedback is either pure positive or negative, *d* remains essentially constant for the entire image[15b,16]) one can reduce the chances of the tip crash.

Figure 3.5 shows an optical image of the EPROM of a Motorola 68HC05 chip (A) and a constant-current SECM image of the 57 μm × 57 μm portion of the same area (B). The constant-current SECM image was acquired in a 1 mM aqueous solution of $FcCH_2OH$ with a 100 nm Pt tip held ~200 nm away from the surface. An external digital feedback control loop was implemented to maintain the constant i_T value during the *x* - *y* scan (see Materials and Methods). The output signal from the E-500 piezo controller was used to monitor the absolute *z*-axis tip position. A constant-distance SECM image is therefore a direct picture of the substrate topography. The substrate surface exhibits a maximum height differential of ~2 μm, which corresponds to ~20 times the tip radius; therefore this image could not have been obtained in a constant-height mode without crashing the tip. An unambiguous verification of a chip pattern produced by SECM was obtained by superimposing it on the optical micrograph (Fig. 3.5C). A very close correspondence can be seen between micrometer-sized features in the optical and electrochemical images. The lateral resolution that can be obtained with an SECM nanotip is higher than that attainable in conventional optical microscopy (i.e., ~0.5 μm). This cannot be seen in Fig. 3.5 because the smallest EPROM feature is greater than 1 μm. We used

IBM wafers built with the 90 nm process technology as a “real world” sample with a smaller feature size. Fig. 3.6A shows an

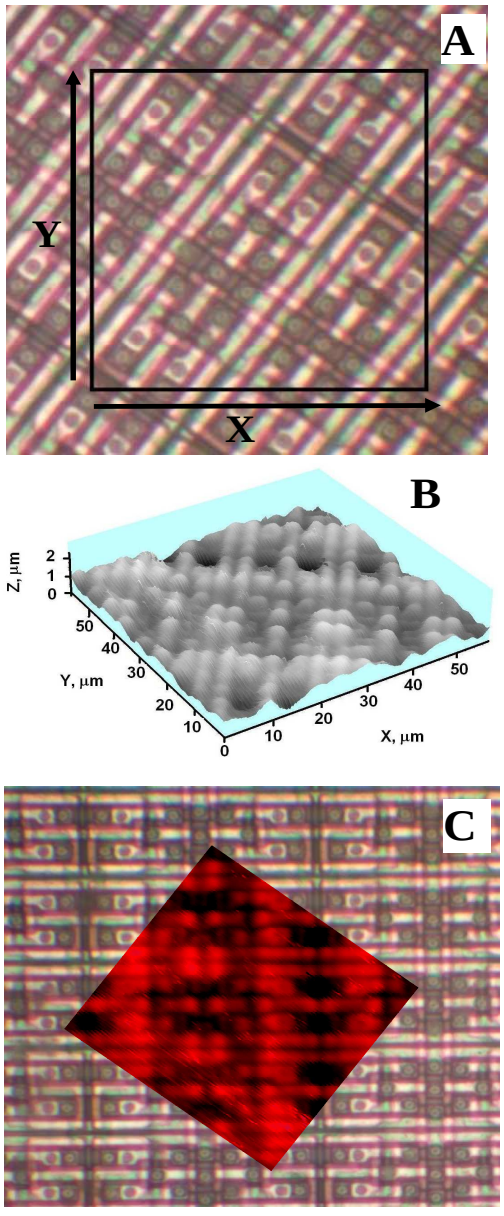

Figure 3.5. Optical image of the EPROM of the Motorola 68HC05 chip (A) and constant-current SECM image (B) of the 57 µm × 57 µm area delimited by the black square in A. The SECM image was obtained in 1 mM $FcCH_2OH$ aqueous solution with a 100 nm Pt tip. The tip substrate distance was ~200 nm, and the current was set at 21 pA (70% or the bulk value). The imaging time was 20 min at the 3 µm/s scan rate. (C) The SECM image (panel

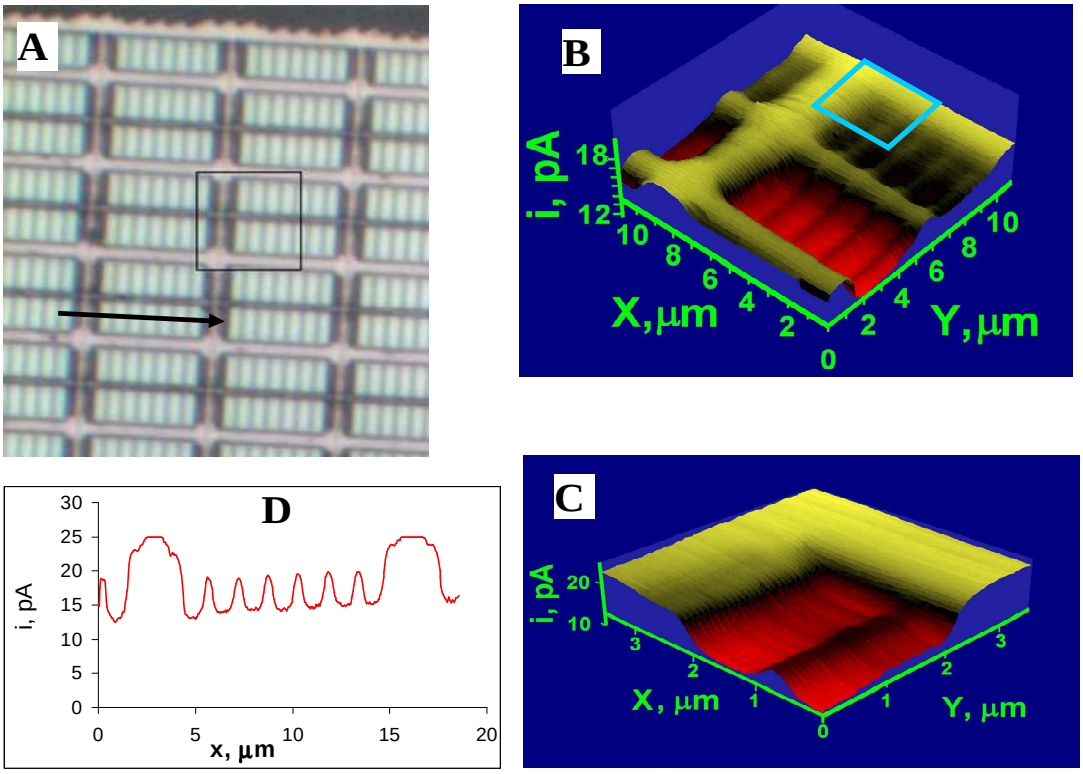

Figure 3.6. Optical (A) and SECM (B) – (D) images of an IBM wafer. (B) Constant-height SECM image of the 12 µm × 12 µm area delimited by a black rectangle in A. (C) 3.5 µm × 3.5 µm constant-height image of the area marked by the blue square in B. (D) Lateral line scan of the tip over the wafer surface shown by the arrow in panel A. Aqueous solution contained 250 mM KCl and 1 mM $FcCH_2OH$. *a* = 55 nm. ν = 600 nm/s (B) and 200 nm/s (C).

optical image of an electroinactive area of the wafer located inside a microcircuit. Fig. 3.6B is a 12 µm × 12 µm constant-height SECM image of the region delimited by the black rectangle that was obtained with a 55-nm Pt tip. The electrochemical image reproduces well the features discernable on the optical image. The small size of the tip allowed us to zoom in onto a 3.5 µm × 3.5 µm portion of the surface (Fig. 3.6C) represented by the blue square in Fig. 3.6B.

A potentially useful application of high-resolution SECM imaging is to detecting small defects in the wafers. Figure 3.7A shows an optical micrograph of an electroinactive region separating microcircuits on the wafer. A microscopic defect appears as a faint pinkish spot in the lower left corner of the image area delimited by the black rectangle. The geometric pattern of

the wafer surface (i.e., a square array of submicrometer-sized, pyramidal bumps) is completely intact in the defect area. A 9 μm ×8 μm constant-current SECM image (Fig. 3.7B) corresponding to the black rectangle area in Fig. 3.7A shows a square pattern in accordance with the optical image. A striking difference is that Fig. 3.7B exhibits a large "dip" in the area corresponding to a barely visible defect in Fig. 3.7A. Clearly, this "dip" is not a topographic feature (such a feature would have been visible in Fig. 3.7A), but a spot of increased surface reactivity. Unlike the rest of the surface, which exhibits pure negative feedback, some regeneration of the redox mediator occurs at this spot and produces a dip-like feature in the constant-current SECM image (i.e., the tip is moved closer to the surface to maintain the set current value).

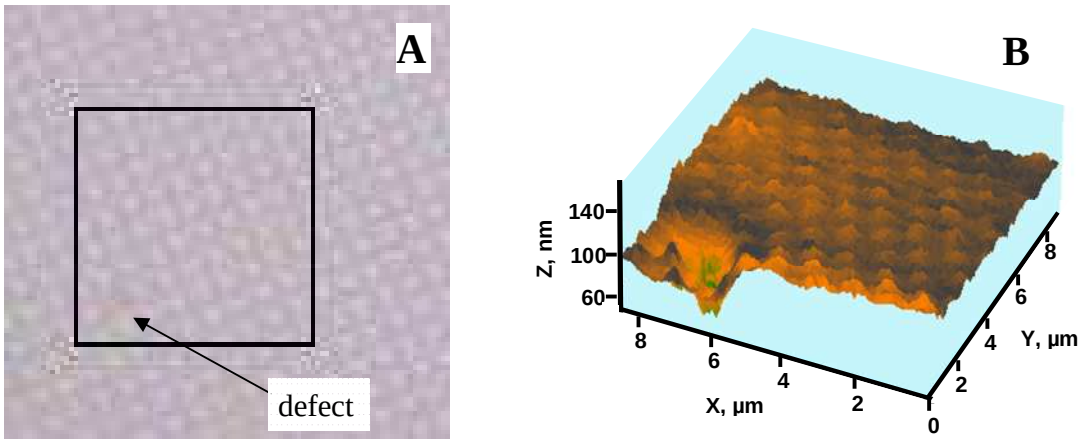

Figure 3.7. (A) Optical image of an IBM wafer showing a microscopic defect and (B) constant-current SECM image of the 9 μm × 8 μm region delimited by the black rectangle in A. Solution contained 5 mM $Ru(NH_3)_6Cl_3$ and 250 mM KCl. a = 190 nm. v = 500 nm/s

3.4 Conclusion

We have demonstrated that different modes of the SECM operation can be used to image surface topography on the nanoscale. Since the spatial resolution of the SECM is governed by the tip radius, the use of nanometer-sized probes allows one to attain the lateral resolution in the range

of tens of nanometers. The smallest feature size in the employed samples (~200 nm) was significantly larger than the spatial resolution attainable with our smallest tips. The ultimate limit for the later resolution of SECM should be ~5 to 10 nm; while the z-axis resolution can be as high as ≤1 nm.[21a] An additional advantage of nm-sized amperometric probes is the fast mass transfer, which allows SECM imaging to be done under steady-state conditions in viscous media such as ionic liquids.

Unlike previous studies, where submicrometer-sized SECM probes were employed to image soft substrates (e.g., biological cells[11] or liquid-filled pores[18]), here we imaged "real-world" solid samples with irregular surface features—e.g., electronic microcircuits—without tip/substrate collisions that would have resulted in tip crashes. This was possible in part because of the well defined geometry of our flat, polished tips, which allowed accurate evaluation of *d* form the tip current. The constant-current mode of the SECM imaging was especially useful for acquiring images of large areas of non-flat and tilted substrates.

Another advantage of well characterized disk-type nanotips is the possibility of quantitative data analysis. In the case of either pure positive or negative feedback, the obtained current map can be converted to the topographic image, as it was done in Fig. 3.2D. If the tip current is limited by finite rate of mediator regeneration at the substrate, SECM can be used for nanoscale mapping of surface reactivity, and local heterogeneous kinetics can be determined from the current vs. distance curves.

Chapter IV

Adsorption/Desorption of Hydrogen on Pt Nanoelectrodes: Evidence of Surface Diffusion and Spillover

4.1 Introduction

The electrolysis of water, which was first observed by Volta in the beginning of the nineteenth century, is probably the best studied electrochemical process. At a Pt working electrode, water can be either oxidized at positive potentials to produce oxygen or reduced at negative potentials to produce hydrogen. Extensive studies of both hydrogen and oxygen evolution reactions focused on their kinetics,[1] catalysis,[2] and numerous applications including energy storage.[3] Adsorption of hydrogen and oxygen species occurs at less negative (hydrogen) and positive (oxygen) potentials than their evolution processes. Voltammetry in acidic solution is a standard technique used for electrode characterization, and a typical cyclic voltammogram (CV) at a large (i.e., millimeter-sized) Pt electrode exhibits several pairs of peaks corresponding to adsorption/desorption of hydrogen and oxygen-containing species (Fig. 4.1A).[4] The characteristic value of charge density associated with a monolayer of hydrogen adsorbed on polycrystalline platinum (210 $\mu C/cm^2$) is widely used to determine the true (microscopic) surface area of Pt electrodes.[5] The ratio of the microscopic surface area to the geometric area (A_m/A_g) gives the roughness factor (ρ).[6]

An important process related to hydrogen adsorption is the spillover, i.e., migration of the chemisorbed hydrogen from the metal electrode (or catalyst) onto the support surfaces. Known for decades,[7] this phenomenon recently attracted significant attention because of its implications for hydrogen storage.[8] The mechanisms of hydrogen spillover onto various amorphous and

crystalline substrates surfaces including oxides,[9] activated carbon,[10] zeolites,[11] and metal organic frameworks[12] have been investigated, however little is known about its spillover in glass.

Here we employ nanometer-sized Pt electrodes to probe hydrogen adsorption/desorption processes. An electrode of this type with a radius, $a \geq 5$ nm can be produced by pulling a Pt microwire into a glass capillary with the help of a laser pipette puller.[13a] After pulling, the metal wire is completely sealed into glass, and its nm-sized tip can be exposed by gentle polishing under video microscopic control. The geometry of polished nanoelectrodes was thoroughly characterized by combination of voltammetry, scanning electron microscopy and scanning electrochemical microscopy (SECM). It was shown that the radius value determined from steady-state voltammetry is close to the effective radius of the conductive disk. The absence of detectible solution leakage through the glass seal was also demonstrated.[13] An important advantage of well characterized disk-type nanotips is the possibility of quantitative data analysis.

A fundamental question in nanoelectrochemistry is whether any unexpected phenomena may occur at nano-interfaces that cannot be observed in macroscopic electrochemical systems.[13c-15] Below we report unusual features of hydrogen adsorption/desorption processes, which could be observed at Pt nanoelectrodes—but not at macroelectrodes—due to the very small surface area of the metal/solution interface.

4.2 Experimental Section

Chemicals. Ferrocenemethanol ($FcCH_2OH$, 97%) from Aldrich (Milwaukee, WI) was recrystallized twice from acetonitrile. Hexaammineruthenium (III) chloride ($Ru(NH_3)_6Cl_3$, 99%) was obtained form Strem Chemicals (Newburyport, MA). H_2SO_4 from Aldrich (Milwaukee, WI), $CuSO_4$ from Mallinckrodt Inc. (Paris, KY), KCl from Fisher Scientific Co. (Fair Lawn, NJ)

were used as received. Aqueous solutions were prepared from deionized water (Milli-Q, Millipore Co.).

Electrodes and electrochemical cells. The fabrication of the laser-pulled Pt nanoelectrodes was described previously.[13a] Briefly, an annealed 25-μm Pt wire (Goodfellow) was pulled into a borosilicate capillary (Drummond; 1.0-mm o.d, 0.2-mm i. d.) under vacuum with the help of a Sutter P-2000/G laser pipet puller. The pulled electrodes were polished on 50 nm lapping tape under video microscopic control, and washed by distilled water. The effective radius of an electrode was evaluated from steady-state voltammetry, and only electrodes producing well-shaped sigmoidal voltammograms of 1 mM $FcCH_2OH$ at a scan rate, v = 50 V/s were used for experiments. A Ag/AgCl reference electrode was used for $FcCH_2OH$ and $Ru(NH_3)_6Cl_3$ voltammetry. Experiments in H_2SO_4 and $CuSO_4$ solutions were performed with a coated-wire Ag/Ag_2SO_4 reference to avoid the contact of Pt surface with Cl^-.

Instrumentation and procedures. Chronoamperometric and SECM measurements were performed using a home-built SECM instrument that includes an EI-400 bipotentiostat (Ensman Instruments, Bloomington, IN).[17] Cyclic voltammograms were obtained using either an EI-400 bipotentiostat or a BAS-100B electrochemical analyzer (Bioanalytical Systems, West Lafayette, IN). To remove oxygen, the solutions were purged with high-purity nitrogen before and during the experiments. Unless otherwise specified, CVs of hydrogen adsorption/desorption show the second or subsequent potential cycles, which are essentially indistinguishable from each other (steady-state response), but different from the first potential sweep.

4.3 Results and Discussion

Figure 4.1B shows a CV of 0.5 M H_2SO_4 solution at a 103-nm-radius Pt electrode. With the well-defined hydrogen, double layer, and oxygen regions, the CV shape is quite similar to that in

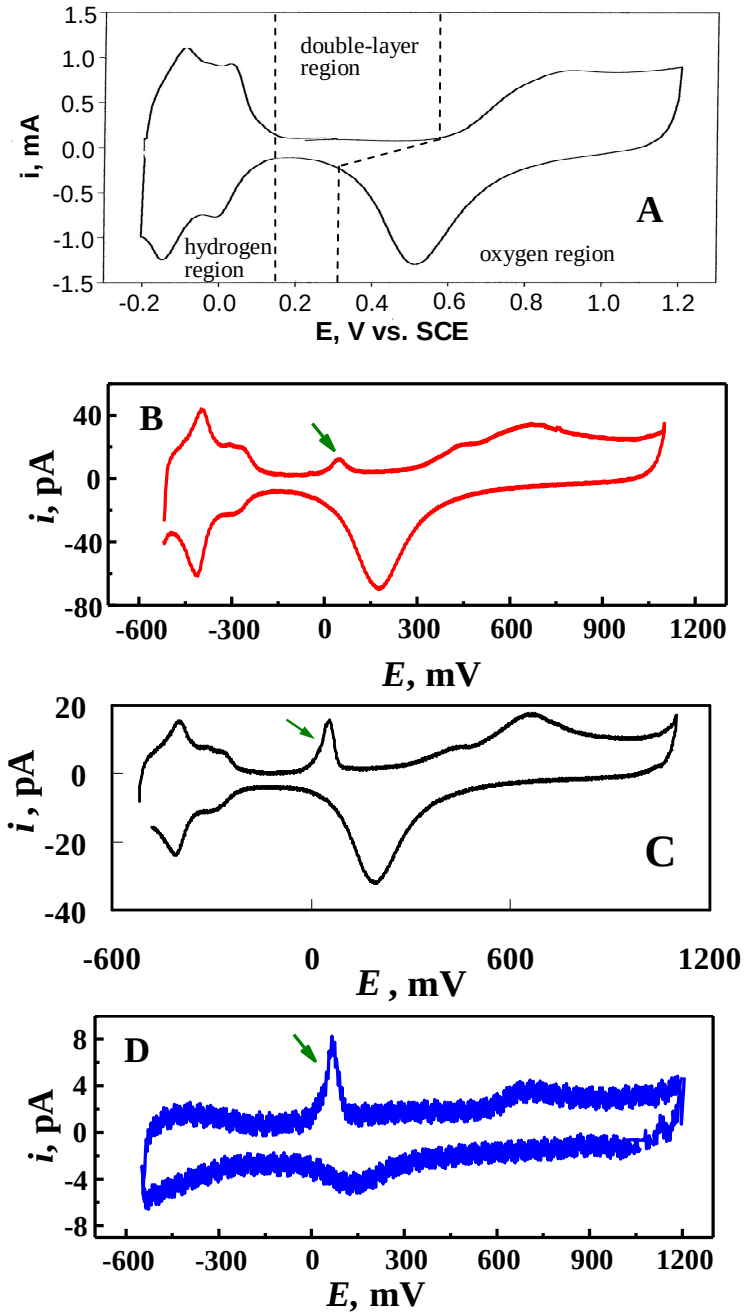

Figure 4.1. Cyclic voltammograms obtained in 0.5 M H_2SO_4 solution at (A) a macroscopic Pt electrode (A_m = 5.47 cm^2)[4] and (B) – (D) Pt nanoelectrodes. a = 103 nm (B), 52 nm (C), and 11 nm (D). ν, mV/s = 100 (A) and 500 (B - D).

Fig. 4.1A, which was obtained at a mm-sized electrode.[4] However, the measured pA-range current is much higher than expected for a = 103 nm and the potential sweep rate, ν = 500 mV/s. The electrode surface area, $A_m = 7.8 \times 10^6$ nm^2 was found by integrating the reduction current in the hydrogen adsorption region. The corresponding effective roughness factor, RF = 234 is incomparably larger than the intrinsic roughness factor, $\rho \approx 2$, typical of polished Pt electrodes.[6]

Assuming cylindrical geometry of the sealed in glass Pt wire, the length of the portion of the wire at which the oxidation/reduction of water takes place must be $l \approx 12$ μm to account for the apparent surface area of 7.8×10^6 nm^2.

Another surprising feature in Fig. 4.1B is a small anodic peak in the double layer region marked by the green arrow (the peak potential, $E_p \cong 50$ mV vs. Ag|Ag_2SO_4 reference; below it is referred to as "DL peak" because of its location in the double layer region). The smaller the electrode radius the more prominent this peak becomes in comparison to other voltammetric waves (cf. Figs. 4.1B, 4.1C, and 4.1D). The effective *RF* value also increases with decreasing *a* (see below).

A simple explanation for the unrealistically large *RF* values found for laser-pulled Pt nanoelectrodes would be solution leakage through the Pt/glass seal. However, the experiments conducted with various redox species dissolved in solution showed no evidence of leakage. Fig. 4.2 (inset) shows two CVs of 1 mM $FcCH_2OH$ at the same 52-nm electrode, which was also used to obtain a CV in Fig. 4.1C. The difference between the voltammograms obtained at ν = 50 mV/s (pink) and 50 V/s (blue) is only in a larger charging current observed with a higher scan

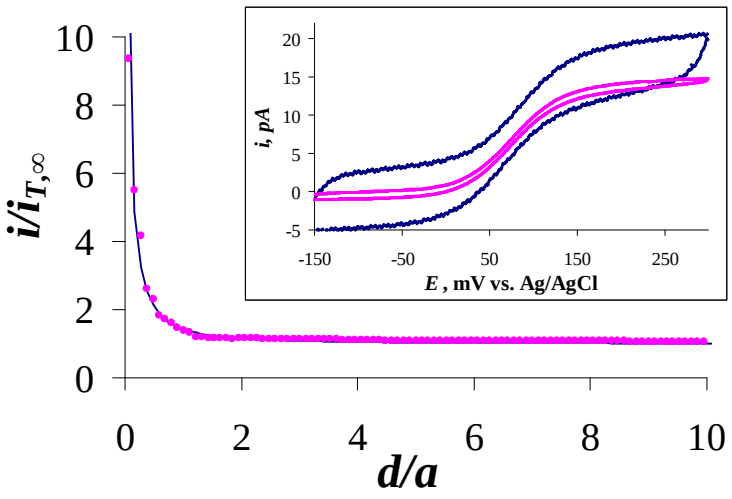

Figure 4.2. Experimental (symbols) and theoretical (solid line) approach curves for a 52 nm Pt electrode approaching an evaporated Au substrate. The tip current is normalized by its value in the bulk solution ($i_{T,\infty}$). The insert shows CVs at the same electrode; ν = 50 mV/s (pink) and 50 V/s (blue). Solution contained 1 mM $FcCH_2OH$ and 100 mM NaCl.

rate. There is no indication of a peak that would be expected if a narrow solution-filled cavity existed inside the glass sheath. Similar fast scan voltammograms were obtained for a number of polished Pt nanoelectrodes; but no peak-shaped CVs were obtained even with much higher concentrations of redox species (e.g., 25 mM $Ru(NH_3)_6^{3+}$; not shown).

Additional evidence against electrode leakage comes from the SECM approach curves (Fig. 4.2), which show an excellent agreement between the experimental data (symbols) and the theory (solid curve) even at very close tip/substrate separation distances (d; e.g., the shortest distance in Fig. 4.2 is $d \cong 0.1a$ = 5.2 nm). Importantly, the fit was obtained with the same a = 52 nm that was found from the CV (pink curve in the Fig. 4.2 inset). Such an agreement would not be possible if the insulating glass sheath were leaking. This conclusion is in accordance with ref. 16, where no leakage was revealed by extensive characterization of glass-sealed Pt nanoelectrodes, and with our previous results.[13]

Since the shape of the entire nanoelectrode CV (including the peaks present in both hydrogen and oxygen regions; Figs. 4.1B and 4.1C) is very similar to that of the CV obtained at a large Pt electrode (Fig. 4.1A), one has to conclude that the A_m value is the same for both hydrogen adsorption/desorption and oxide formation/reduction processes. This is in agreement with the notion that the same redox species—water—participates in both processes.[18] Unlike $FcCH_2OH$ and $Ru(NH_3)_6Cl_3$, water molecules adsorb on Pt surface[19] and can travel on it via surface diffusion.[20] The surface diffusion of water along the Pt/glass boundary results in a the formation of an aqueous film covering a micrometer-long portion of the Pt wire; hence a dramatic increase in the A_m and RF values obtained from Figs. 4.1B – 4.1D. In the absence of this effect (e.g., when surface diffusion is negligibly slow or the insulated portion of the metal surface is chemically passivated), the nanoelectrode surface area found from oxidation/reduction

of the adsorbed molecular monolayer is similar to the area calculated from the diffusion current of redox species dissolved in solution.[21]

The unusual DL peak in Figs. 4.1B – 4.1D can be recorded by scanning the electrode potential between the double-layer region (e.g., ~200 mV vs. Ag/Ag_2SO_4) and hydrogen region, as shown in Fig. 4.3; therefore it is not related to oxide formation/reduction. However, this peak does not appear unless the negative limit of the potential scan is in the hydrogen region (i.e., the switching potential, $E_\lambda \lesssim$ -250 mV).

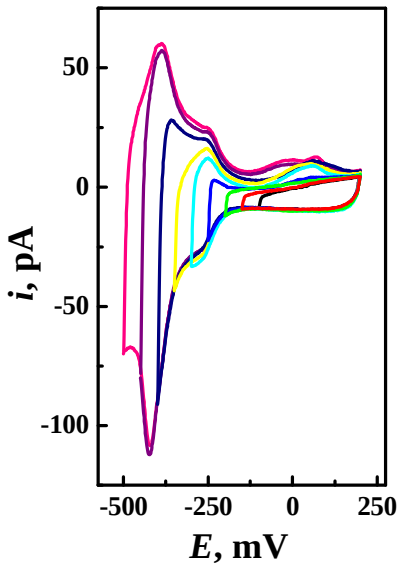

Figure 4.3. Effect of the negative potential scan limit on CVs of hydrogen adsorption/desorption at a 140-nm Pt electrode in 0.5 M H_2SO_4 solution. The potential was swept between +200 mV and different values of E_λ (mV): -500 (pink), -450 (purple), -400 (dark blue), -350 (yellow), -300 (turquoise), -250 (blue), -200 (green), -150 (red), and -100 (black). ν = 200 mV/s.

One may notice some similarity between the DL peak and a sharp peak that appeared on voltammograms of Pt (111) electrodes in H_2SO_4 and H_3PO_4 solutions and was attributed to anion adsorption.[22] However, the adsorption peaks in ref. 22 were reversible, in contrast with the totally irreversible DL peak. Another important difference is that the DL peak appears only after the Pt electrode potential was made sufficiently negative to induce hydrogen adsorption. The DL peak was also present in CV's recorded in perchlorate solutions (not shown), in which no anion adsorption peak was observed.[22]

Table 4.1 presents additional evidence that the DL peak is due to hydrogen desorption. For three different nanoelectrodes, the cathodic charge corresponding to hydrogen adsorption (Q_a) is larger than the Q_d value found by integrating the anodic current in the hydrogen region. However, a very close agreement between the adsorption and desorption charges—within 5%—can be obtained by adding the Q_{DL} value (i.e., the integral of the current under the DL peak) to Q_d. To our knowledge, the DL peak has not been observed at macroscopic electrodes, and it becomes more prominent as *a* decreases (Figs. 4.1B – 4.1D and Table 4.1). This irreversible peak (there is no corresponding cathodic peak) can be attributed to hydrogen desorption at the Pt/glass interface.

Table 4.1. Anodic and cathodic charges and effective roughness factors obtained from CVs of hydrogen adsorption/desorption (0.5 M H_2SO_4) and stripping of underpotentially deposited copper (10 mM $CuSO_4$ + 0.5 M H_2SO_4) at Pt nanoelectrodes.

Process / Electrode	Hydrogen adsorption/desorption					UDP of copper	
	a, nm	Q_a, pC	Q_d, pC	Q_{DL}, pC	RF_H	Q_{Cu}, pC	RF_{Cu}
1	38	7.9	5.7	1.9	829	15.9	855
2	86	24.5	21.8	2.1	503	45.3	473
3	140	64.1	59.2	6.3	491	113.9	448

In all voltammograms discussed above (Figs. 4.1B – 4.1D and 4.3), the successive potential cycles (starting with the second cycle; the first potential sweep is always somewhat different) produced almost indistinguishable current responses. This indicates that the Pt surface area covered by the water monolayer was essentially constant and time-independent. The corresponding steady-state *RF* can be expressed as

$$RF = A_m/A_g = (\pi a^2 + 2\pi al)/\pi a^2 = 1 + 2l/a \quad (4.1)$$

and, thus, the effective length of the Pt wire covered by the water film is

$$l = a(RF - 1)/2 \quad (4.2)$$

Although Eq. (4.2) does not take into account the roughness of Pt surface, it should still provide a realistic estimate for l because the RF values of several hundred are incomparably larger than $\rho \approx 2$ expected for polished Pt.[6] From RF values for hydrogen adsorption in Table 4.1 one obtains $l = 25 \pm 8$ μm. This distance may represent the length of the wire portion sealed in glass. The oxidation/reduction of water at the Pt/glass interface was observed recently.[23] The variations in l in Table 4.1 are quite significant (within the factor of 2), and they may be even larger for nanoelectrodes prepared using different fabrication methodologies or different pulling programs.

Micrometer-range l values indicate that the effect of surface diffusion of water should be observable not only at nanoelectrodes, but also at μm-sized electrodes (assuming $l = 25$ μm, one obtains $RF = 11$ for $a = 5$ μm and $RF = 1.05$ for $a = 1$ mm). To check this hypothesis, we obtained CVs of hydrogen adsorption/desorption at a 12.5-μm-radius glass-sealed Pt disk electrode produced by using standard procedures for microelectrode fabrication (i.e., heat-sealing without pulling[24]). The obtained RF value of 18 shows that the surface diffusion effect is indeed significant for μm-sized electrodes. $l \approx 100$ μm calculated from Eq. (4.2) for this electrode was comparable to the microscopically observed length of the glass-sealed portion of the Pt wire.

CVs of hydrogen adsorption/desorption at micrometer-sized Pt electrodes were presented previously in ref. 18. The charge found by integrating the cathodic current in the hydrogen region of the CV obtained at the 5-μm-radius Pt disk electrode (Fig. 2 in ref. 18) corresponds to $A_m \approx 4 \times 10^3$ μm^2 and $RF \approx 50$. Other CVs in ref. 18 yield similar RF values. (The A_m values are

not reported in ref. 18, which is largely concerned with the effect of pH on hydrogen peak potentials).

Underpotential deposition (UPD) of copper at Pt nanoelectrodes has been widely employed to comparision of the A_m and *RF* values, we obtained CVs of the copper stripping from the same nanoelectrodes that were employed in hydrogen adsorption/desorption measurements (Table 4.1). Unlike hydrogen adsorption/desorption processes, which produce steady-state CVs without preaccumulation, the height of the copper stripping peak increases significantly if the electrode is

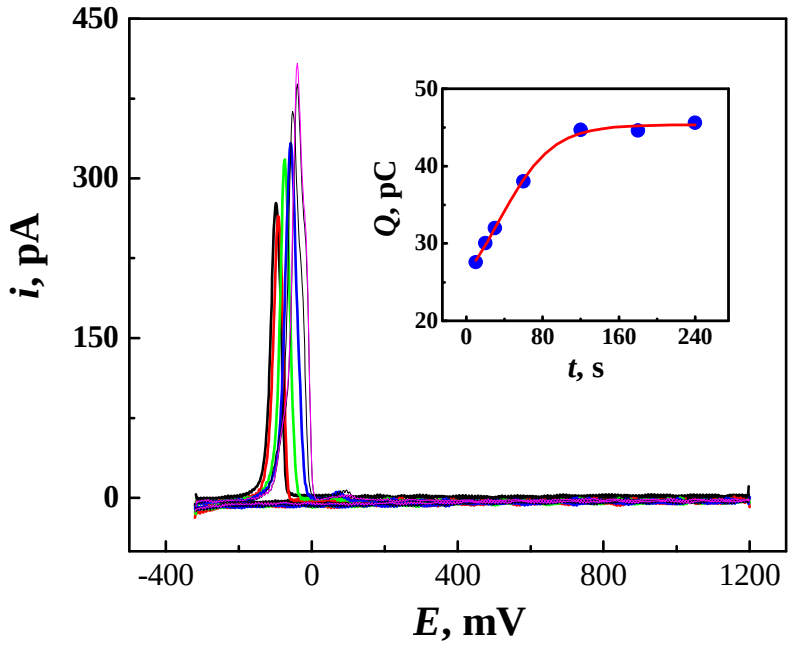

Figure 4.4. CVs of stripping of underpotentially deposited Cu from 86-nm-radius Pt electrode. Before stripping, the electrode was held at -320 mV vs. $Ag|Ag_2SO_4$ for (from bottom to top): 10 s, 20 s, 30 s, 1 min, 2 min, 3 min and 4 min. ν = 500 mV/s. The insert shows the charge obtained from each stripping peak as a function of holding time. Solid curve is shown as a guide.

held at a potential sufficiently negative to induce UPD of Cu before the anodic scan. Several stripping voltammograms shown in Figure 4.4 were obtained at the same 86-nm-radius Pt electrode after holding it at -320 mV vs. $Ag|Ag_2SO_4$; the holding time (t) was varied between

10 s and 4 min. The corresponding charge (i.e., the area under the stripping peak plotted in the inset as a function of *t*) initially increased with *t* and leveled off at $t \cong 120$ s. Thus, it takes ~2 min to form a complete monolayer of copper adatoms on the entire Pt surface. Similar behavior was reported by Elliott *et al.*[26] In their experiments, up to 5 min holding time was required to achieve complete coverage of the nanostructured Pt microelectrode surface by underpotentially deposited Cu; while it took only a few seconds for nearly complete coverage of a polished Pt macroelectrode. This difference was attributed to the hindered transport of Cu^{2+} ions through the porous nanostructure.[26] In our case, the deposition time required to attain the complete coverage is determined by the rate of surface diffusion of copper adatoms on the Pt/glass interface. Unlike

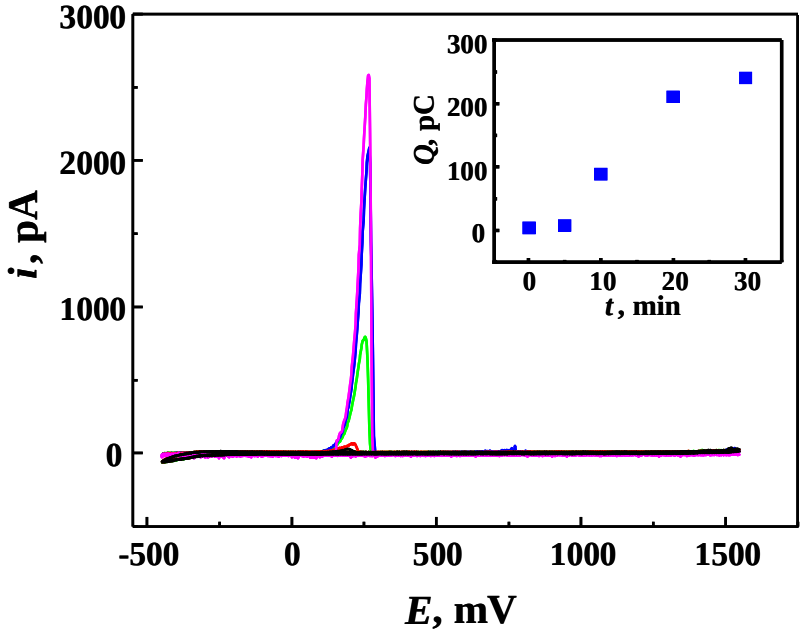

Figure 4.5. CVs recorded in 0.5 M H_2SO_4 solution after holding a 38-nm Pt nanoelectrode at -450mV vs. $Ag|Ag_2SO_4$ quasi-reference. *t*, min (from bottom to top): 0.1, 5, 10, 20, 30. ν = 500 mV/s. Insert: dependence of the anodic charge vs. *t* obtained from the same CVs.

Cu adatoms that have to be generated *in situ* by holding a Pt electrode at a negative potential, an aqueous monolayer is formed on the Pt surface immediately after its immersion in solution.

The charge (Q_{Cu}) and corresponding RF_{Cu} values in Table 4.1 were obtained from copper stripping voltammograms recorded after two-minute long deposition at E = -320 mV. The

remarkably close agreement (within <10%) between the *RF* values obtained from hydrogen and copper voltammograms at each nanoelectrode suggests that the same surface area (A_m) was covered by both species. Nevertheless, major differences between these processes became

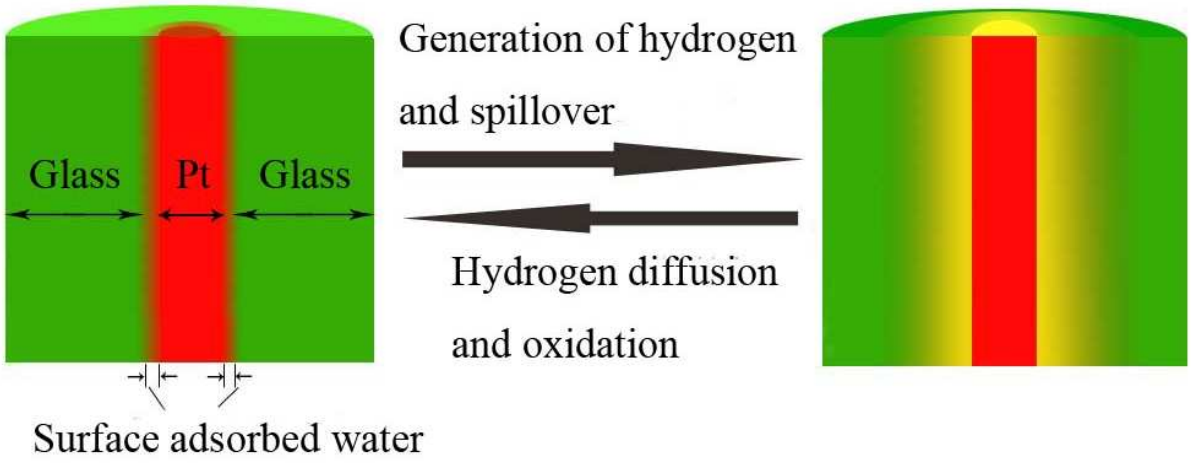

Figure 4.6. Schematic representation of hydrogen generation in the adsorbed water film on the negatively the biased Pt surface, its spillover into glass, diffusion within the glass phase, and oxidation on Pt surface at positive potentials.

apparent when we tried to preaccumulate hydrogen by holding the electrode potential at -450 mV before obtaining a CV (Figure 4.5).

The most prominent feature in Fig. 4.5 is a very large DL peak, whose height increased with holding time, *t*. A very high peak current (at *t* = 30 min, it was >100 times higher than without preaccumulation) obscures other voltammetric features whose magnitude was essentially independent of *t*. Unlike Cu UPD, the *Q* vs. *t* dependence (the inset in Fig. 4.5; obtained by integrating the anodic current in the hydrogen and double-layer regions) has not leveled off after two minutes. The very large charge values in Fig. 4.5 (inset) and its continuing increase even at *t* ≥30 min cannot be attributed to adsorption/desorption of a monolayer of hydrogen. The data in

Fig. 4.5 suggest that most of hydrogen generated when the electrode was held at -450 mV was transferred into the glass phase via spillover from the Pt surface. During the subsequent potential sweep in the positive direction, the accumulated hydrogen diffuses to the Pt surface and gets reoxidized on it (Figure 4.6). This process is responsible for the DL peak. The DL peak cannot be recorded at a conventional-size Pt electrode because of its large surface area and high

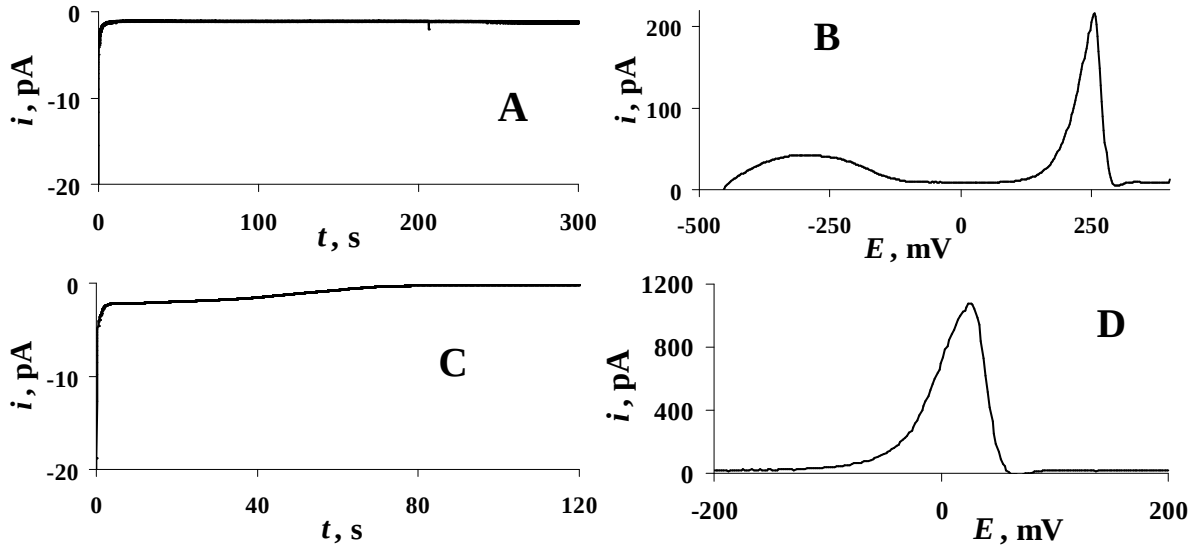

Figure 4.7. Chronoamperograms of hydrogen adsorption (A) and copper UPD (C), and anodic voltammograms of hydrogen (B) and copper stripping (D) recorded at the same 129-nm-raduis Pt electrode. Solution contained 0.5 M H_2SO_4 and (C, D) 10 mM $CuSO_4$. The potential was stepped from +200 mV to -450 mV (A) and from +200 mV to -320 mV (C) vs. $Ag|Ag_2SO_4$. (B, D) ν = 500 mV/s.

Faradaic and charging currents flowing at the metal/solution interface. This peak becomes apparent when the electrode radius is smaller than ~200 nm (Fig. 4.1B).

To test this model, we compared the charges corresponding to accumulation and oxidation cycles of hydrogen and copper at the same nanoelectrode. The integration of chronoamperometric reduction current (Figure 4.7A) recorded over the 5 min period after stepping the Pt nanoelectrode potential from 200 mV to -450 mV yielded Q_a = 354 pC. This

number is ~10 times larger than the total hydrogen desorption charge ($Q = Q_d + Q_{DL}$ = 14.2 pC + 24.6 pC = 38.8 pC) obtained from Fig. 4.7B. The ~90% loss of the accumulated hydrogen results from its spillover from Pt and bulk diffusion into the glass phase. The UPD/stripping of copper on the same nanoelectrode (Figs. 4.7C and 4.7D) produced completely different results: the stripping charge (110.9 pC) was very similar to the charge obtained from the deposition transient (114.8 pC), as expected in the absence of spillover effects.[5]

Apparently, the spillover of hydrogen from Pt onto glass is a spontaneous process, which is driven not only by concentration gradient, but also by the free energy of hydrogen chemisorption on glass. The reverse process is not spontaneous, and because of its overpotential the DL peak appears at significantly more positive potentials than regular hydrogen desorption peaks. The observed spillover of adsorbed hydrogen is different from physicosorption of H_2 gas on glass. The latter process would not produce a significant shift in desorption peak potential.

4.4 Conclusion

We used nanoelectrochemical approaches to reinvestigate the well studied processes—hydrogen adsorption/desorption at polycrystalline Pt. A very small surface area of a nanoelectrode exposed to solution allowed us to observe unusual features of these reactions, which would not be accessible by conventional-size electrochemical probes. In the case of glass-sealed electrodes, a monolayer of adsorbed species can form at the metal/glass interface thus greatly increasing the effective surface area. This effect was demonstrated for a monolayer of adsorbed water and for copper underpotentially deposited on Pt. The spillover of hydrogen adatoms from the Pt/glass interface results in accumulation of hydrogen inside the glass phase. The subsequent oxidation of the spilled hydrogen at Pt during the anodic potential sweep results in the appearance of an unusual peak in the double layer region.

Chapter V

Electrochemistry through Glass

5.1 Introduction

An intriguing aspect of nanoelectrochemical experiments is a possibility of using a nanometer-sized electrode to observe processes and phenomena, which are not accessible by macroscopic probes.[1] Examples include single molecular events,[2] unusual transport phenomena[3] and electrical double layer effects.[4] The subject of this article—electrochemistry through glass—may sound like an oxymoron because glass is commonly used as an insulating material in electrode fabrication. However, ~100 nm-thick layers of glass turned out to be sufficiently conductive for electrochemical measurements.

The propagation of an electrical signal through thin glass membranes has been extensively studied since the beginning of the twentieth century due to its relevance to the potentiometric glass pH electrode.[5] Since the potential of the glass electrode is a linear function of solution pH, it is intuitive to assume that the voltage drop across the membrane is determined by the proton transfer. However, numerous experiments employing ^{3}H isotope and other methods showed that protons do not cross the glass membrane.[6,7] The potentiometric response of the pH electrode originates in the ion-exchange equilibrium on the glass surface, and the diffusion of protons and water is essentially confined to a nanometer-thick surface layer of hydrated gel. This gel forms on both sides of the membrane when it is soaked for several hours in acidic aqueous solution.[8] This response mechanism was established for electrodes with micrometer-thick sensing membranes (the typical thickness is ~100 μm). The behavior of nm-thick glass layers is substantially different.

We employed nanometer-sized Pt electrodes to investigate the permeability of glass in aqueous and non-aqueous solutions. An electrode of this type with the conductive core radius, *a* $\geq$ 5 nm can be produced by pulling a Pt microwire into a borosilicate glass capillary with the help of a laser pipette puller.[9] After pulling, the metal wire is completely sealed into glass, and its nm-sized tip can be exposed by gentle polishing under video microscopic control. The geometry of polished nanoelectrodes was characterized by combination of voltammetry, scanning electron microscopy and scanning electrochemical microscopy (SECM). It was shown that the effective radius value (*a*) determined from steady-state voltammetry is close to the geometric radius of the conductive disk. The absence of detectible solution leakage through the glass seal was also demonstrated.[9] By selecting suitable pulling parameters, the thickness of glass at the tip could be varied between a few tens of nanometers and several micrometers. The pulled Pt probes encased in submicrometer-thick glass were used in experiments described in this article.

5.2 Experimental Section

Chemicals. Ferrocenemethanol ($FcCH_2OH$, 97%) from Aldrich (Milwaukee, WI) was recrystallized twice from acetone. Hexaammineruthenium (III) chloride (99%) was obtained from Strem Chemicals (Newburyport, MA). KNO_3, Li_2SO_4 and KCl (99+%, Aldrich) were used as supporting electrolytes. Aqueous solutions were prepared from deionized water (Milli-Q, Millipore Co.). Twice distilled HPLC grade DCE (Sigma-Aldrich) was used to prepare organic solutions. Potassium hexachloroiridate (III) from Alfa Aesar (Ward Hill, MA), H_2SO_4 from Aldrich, and $CuSO_4$ from Mallinckrodt Inc. (Paris, KY) were used as received.

Electrodes. To prepare a "dry" glass-covered nanoelectrode, an annealed 25-μm Pt wire (Goodfellow) was pulled into a borosilicate capillary (Drummond; 1.0-mm o.d., 0.2-mm i. d.) under vacuum with the help of a Sutter P-2000/G laser pipet puller, as described previously.[9,22]

To form hydrated gel, a glass-covered Pt nanoelectrode was allowed to soak in 6 M HCl solution overnight. An electrode removed from HCl solution was rinsed with water before measurements. To improve reproducibility, such electrodes were stored in aqueous solution between experiments. However, it was found that the formed hydrated gel remains on the electrode surface even after keeping it for several days in the oven at ~100 ºC. A two-electrode configuration was employed for voltammetry and chronoamperometry with either a commercial Ag/AgCl reference electrode or a Ag quasi-reference (DCE solutions).

Instrumentation and procedures. Cyclic voltammograms were obtained using either an EI-400 bipotentiostat (Ensman Instruments, Bloomington, IN) or a BAS-100B electrochemical analyzer (Bioanalytical Systems, West Lafayette, IN). All experiments were carried out at room temperature (23 ± 2 °C) inside a Faraday cage. Unless otherwise specified, CVs obtained at glass-covered electrodes show the second or subsequent potential cycles, which are essentially indistinguishable from each other (steady-state response), but different from the first potential sweep. pH measurements were carried out in the following solutions: HCl/KCl (pH 1), phthalate buffers (pH 2 to 4), acetate buffers (pH 3 to 6), phosphate buffers (pH 7 and 8), and carbonate buffers (pH 9 and 10). SEM images were obtained using a field emission scanning electron microscope (Zeiss Supra 55 VP) with no conductive coating applied to nanoelectrodes.

5.3 Results and Discussion

Figure 5.1A shows cyclic voltammograms (CVs) obtained at two glass-covered Pt nanoelectrodes in 0.5 M H_2SO_4 solution. Curve 1 obtained at an electrode with a thicker glass sheath exhibits very low charging current and no cathodic or anodic waves within a wide potential window (±3 V). This response could be expected since the conductive Pt core is completely buried in borosilicate glass, which is often used as an insulating material in

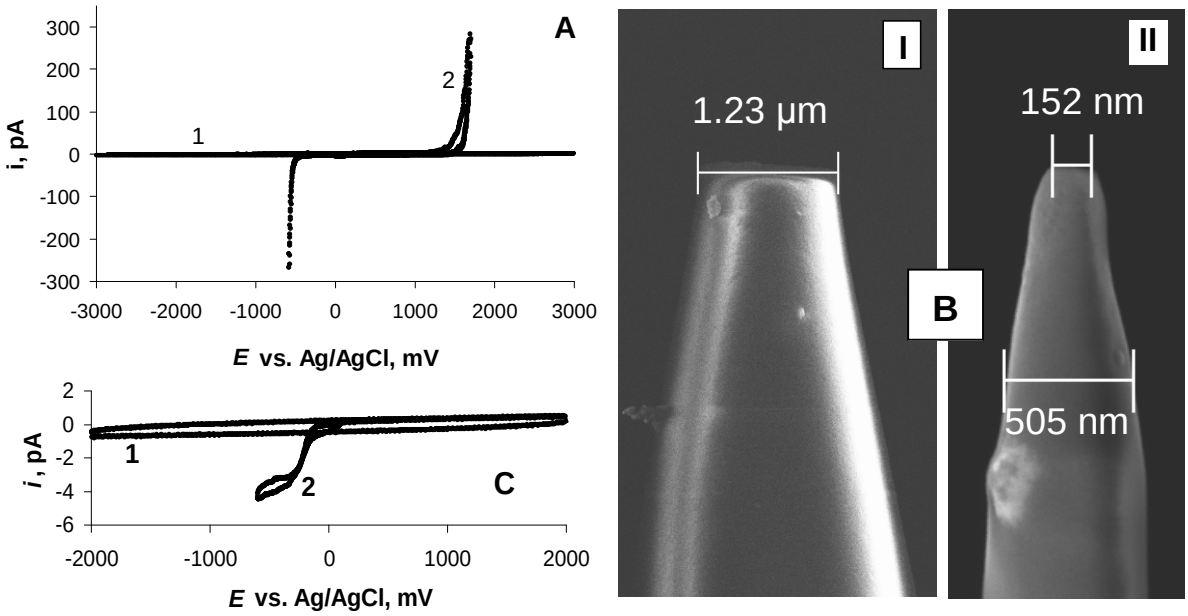

Fig. 5.1. Characterization of glass-covered nanoelectrodes. (A) Voltammograms obtained in 0.5 M H_2SO_4 solution at Pt nanoelectrodes with a thicker (1) and thinner (2) insulating glass sheath. (B) SEM images of a thick-glass (I) and a thin-glass (II) electrode. (C) Voltammograms of 20 mM $Ru(NH_3)_6Cl_3$ in 1 M KNO_3 at two thin glass covered electrodes without (1) and with (2) a nm-sized pinhole. Potential sweep rate was v = 500 mV/s

microelectrode fabrication. Curve 2 was obtained at the Pt electrode buried inside a significantly thinner glass sheath (cf. images I and II in Fig. 5.1B). This CV shows well defined anodic and cathodic currents at the electrode potentials, $E \gtrsim +1.5$ V and $E \lesssim -0.5$ V vs. Ag/AgCl reference, respectively. These currents, which increase exponentially with applied potential and can reach relatively high values (nA), are clearly due to the electrochemical oxidation/reduction processes. The only redox species present in our system that can be reduced or oxidized within the above potential range are water and molecular oxygen. The current in curve 2 was essentially unaffected by oxygen removal, thus suggesting that the anodic and cathodic processes are oxidation and reduction of water. The difference between the onset potentials of the cathodic and anodic waves in curve 2 (~2 V) is somewhat larger than the theoretical minimum voltage required for the water electrolysis (1.23 V).

To eliminate the possibility that water molecules diffuse to the Pt surface through microscopic cracks or pinholes in the glass sheath, we obtained voltammograms of hydrophilic (e.g., $Ru(NH_3)_6^{3+}$; curve 1 in Fig. 5.1C) and relatively hydrophobic (e.g., $FcCH_2OH$; not shown) redox species at glass-covered Pt electrodes. The complete absence of a reduction wave observed with the $Ru(NH_3)_6^{3+}$ concentration as high as 20 mM suggests that the Pt core is completely covered by glass. The sensitivity of this test to extremely small pinholes in glass insulator can be seen from Eq. (5.1) for the diffusion limiting current to a disk-shaped electrode:

$$i_d = 4FDac^* \qquad (5.1)$$

where F is the Faraday constant, $D = 6.5 \times 10^{-6}$ cm^2/s is the diffusion coefficient of $Ru(NH_3)_6^{3+}$,[6] and c^* is its concentration in solution. Assuming that a 1-nm-radius Pt disk is exposed to the solution due to the presence of a pinhole, one obtains i_d = 5 pA for c^* = 20 mM. Curve 2 in Fig. 5.1C is an example of the pinhole detection. A well defined reduction wave of $Ru(NH_3)_6^{3+}$ corresponds to the a value as small as 0.7 nm. The actual defect size may be somewhat larger because the measured current is affected by diffusion of redox species through the pore in the glass film. However, the smallest current measurable by our instrument (≤50 fA) is two orders of magnitude lower than that in Fig. 5.1C, and therefore any microscopic defect in glass should be detectible.

The currents in Fig. 5.1A cannot be attributed to diffusion of sodium in glass, because water has to physically cross the membrane in order to be reduced or oxidized at the Pt surface. To further prove this point we monitored the generation of hydrogen (Fig. 5.2) and oxygen (not shown) at sufficiently high cathodic and anodic potentials. Biasing a glass-covered

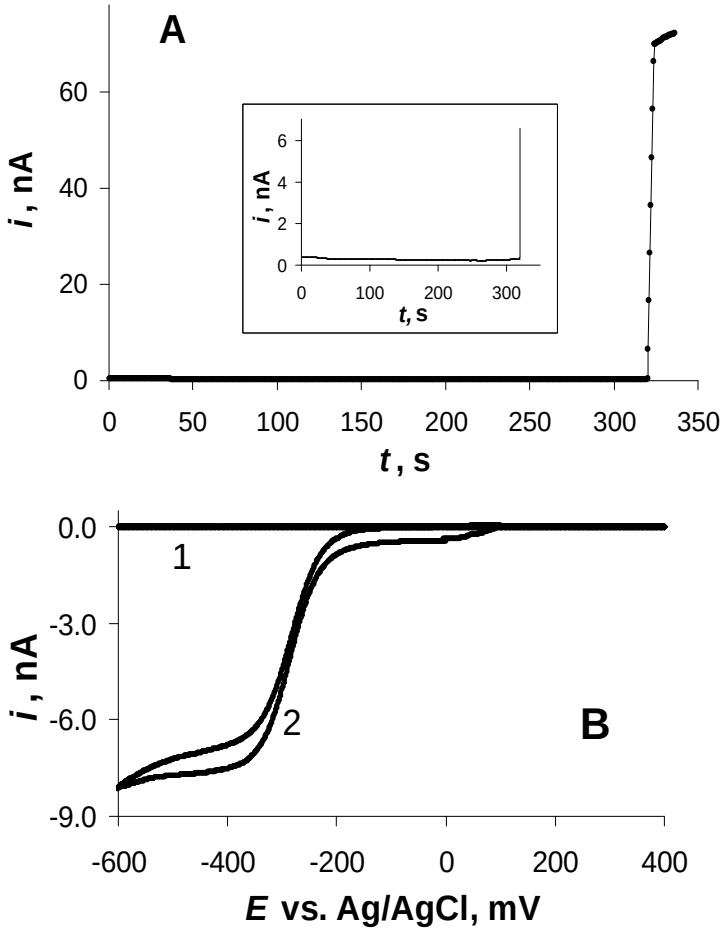

Fig. 5.2. Hydrogen evolution via through-glass electrolysis of water. (A) Current vs. time dependence. The electrode potential was -900 mV. The inset shows the initial portion of the curve (up to the t ≈ 320 s when the insulating sheath was broken) at higher current sensitivity. (B) Voltammograms of 20 mM $Ru(NH_3)_6^{3+}$ obtained before (1) and after (2) hydrogen evolution transient shown in (A).

nanoelectrode at -900 mV in 0.5 M H_2SO_4 produced ~300 to 500 pA current of hydrogen reduction (the inset in Fig. 5.2A). After ~5 min, the pressure of generated hydrogen became high enough to break the insulating sheath and expose Pt surface to solution; hence a dramatic increase in the cathodic current. Fig. 5.2B shows that the reduction of $Ru(NH_3)_6^{3+}$, which did not occur at this electrode before the hydrogen evolution experiment (curve 1), produced a pronounced voltammetric wave after the rupture of insulating glass (curve 2).

Fig. 5.3 shows the response of a glass-covered nanoelectrode to water dissolved in an aprotic organic solvent (1,2-dichloroethane, DCE). The voltammogram obtained with no water added to twice distilled DCE is essentially flat and contains neither anodic (Fig. 5.3A) nor cathodic

(Fig. 5.3B) waves. In contrast, several anodic and cathodic waves appear in the curves obtained with different water concentrations added to DCE (c_{H_2O}; from 1 mM to 130 mM, as shown by the color code in Figs. 5.3A and 5.3B). The height of all waves increases with c_{H_2O}. A more prominent anodic peak is observed at ~3.3 V, which actually represents two closely spaced peaks, as can be seen in the yellow curve. The dependence of this peak current (i_p) vs. c_{H_2O} is essentially linear (Fig. 5.3C).

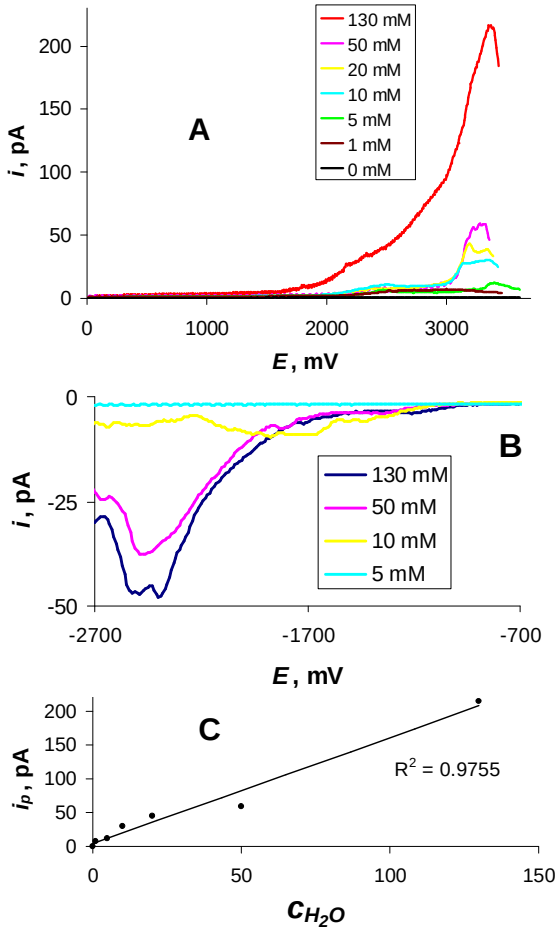

Fig. 5.3. Oxidation/reduction of water in DCE at glass-covered electrodes. (A) Anodic and (B) cathodic voltammograms obtained in DCE solutions containing different concentrations of H_2O. v = 500 mV/s. (C) Dependence of the second anodic peak current in A on c_{H_2O}. Supporting electrolyte was 0.1 M tetrabutylammonium perchlorate.

The behavior of the glass-covered electrode changes dramatically after soaking in acidic solution for a few hours, which is known to result in glass swelling and the formation of a hydrogel surface layer. Fig. 5.4A shows CVs of 0.5 M H_2SO_4 at a glass-covered nanoelectrode

before (1) and after (2) it was kept overnight in 6 M HCl solution. In contrast to curve 1, curve 2 exhibits well-defined hydrogen, double layer, and oxygen regions. This curve is quite similar to voltammograms of water oxidation/reduction obtained at macroscopic Pt electrodes (inset in Fig. 5.4A[10]). The current was stable in time and reproducible; the two subsequent potential cycles shown in Fig. 5.4A produced essentially identical responses.

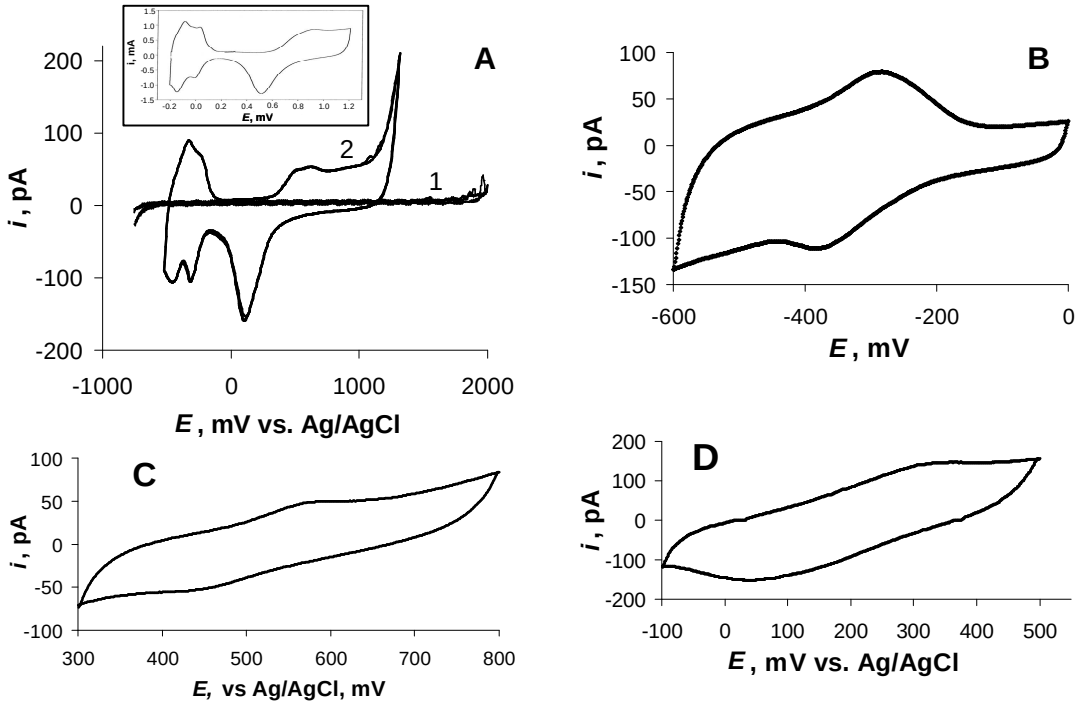

Fig. 5.4. Effect of acid pre-treatment of glass-encased nanoelectrodes on their voltammetric responses. CVs obtained in 0.5 M H_2SO_4 solution before (1) and after (2) an electrode was soaked overnight in 6 M HCl (A); and CVs of 20 mM $Ru(NH_3)_6Cl_3$ in 1 M KNO_3 (B), 15 mM K_3IrCl_6 in 0.2 M KCl (C), and 2 mM $FcCH_2OH$ in 0.25 M KCl (D) at the glass-covered electrode after pretreatment with 6 M HCl. v (mV/s) = 500 (A) and 50 (B – D). The inset in A shows a CV obtained in 0.5 M H_2SO_4 with a macroscopic Pt working electrode (5.47 cm^2) and SCE reference; v = 200 mV/s.[10]

After the acid treatment, a glass-coated electrode responds to redox species other than water. Fig. 5.4B shows a voltammogram of $Ru(NH_3)_6^{3+}$, which (unlike curve 1 in Fig. 5.1C obtained at a dry glass-coated electrode) contains both cathodic and anodic waves. The voltammograms of anionic $IrCl_6^{3-}$ (Fig. 5.4C) and neutral $FcCH_2OH$ (Fig. 5.4D) are not so well shaped.

Fig. 5.5A shows a voltammogram of Cu electrodeposition in hydrated glass. The shape of the curve with a characteristic cathodic peak appearing after the potential sweep reversal and a sharp anodic peak of Cu stripping is typical of metal nucleation/growth processes.[11] In a chronoamperometric experiment (Fig. 5.5B), the electrode potential was stepped to -600 mV to deposit a larger amount of copper. The cathodic current was almost constant during the first 8 s (the inset in Fig. 5.5B) and then it increased sharply by the factor of >400 (the highest current of 10 nA in Fig. 5.5B corresponds to the overflow of the potentiostat amplifier). The growth of copper beyond the hydrogel limits and the formation of a micrometer-sized metal electrode was confirmed voltammetrically (not shown), and deposited Cu was observed by optical microscopy and SEM.

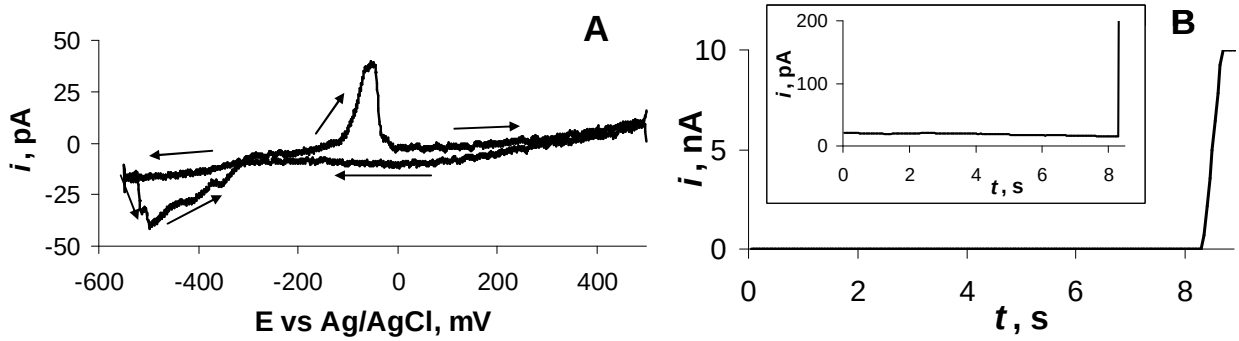

Fig. 5.5. CV (A) and chronoamperogram (B) of copper deposition on the Pt nanowire buried in hydrated glass from 20 mM $CuSO_4$ solution. (A) ν = 50 mV/s. (B) The electrode potential was stepped to -600 mV vs. Ag/AgCl. The inset shows the initial portion of the current transient at higher current sensitivity.

The potentiometric response of the hydrated glass nanoelectrode to solution pH is shown in Figure 5.6. After soaking a glass-covered Pt electrode overnight in 6 M HCl, its potential was measured in ten buffer solutions of different pH. The linear pH dependence (r^2 > 0.99) of the electrode potential over the range of pH from 1 to 10 exhibits a slightly sub-Nernstian slope of 52 mV/pH.

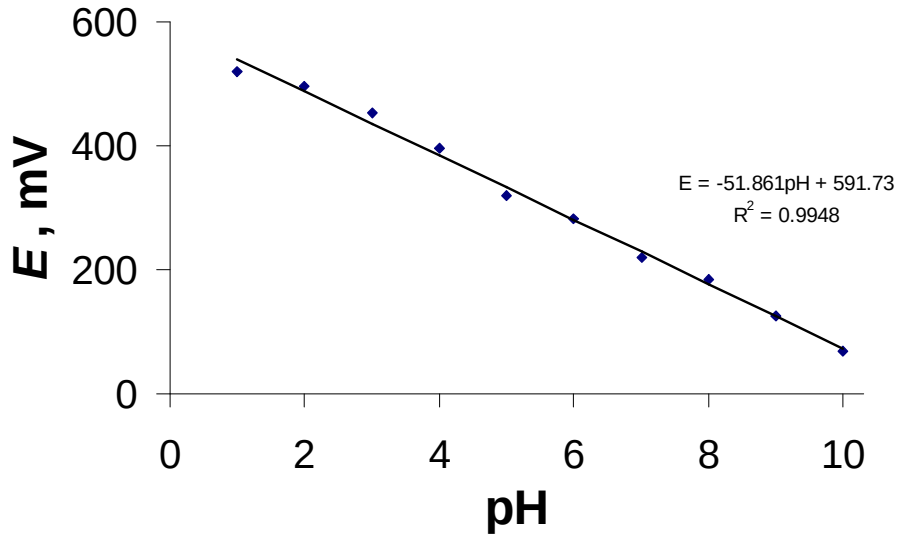

Fig. 5.6. Potentiometric response of a glass-covered Pt nanoelectrode to solution pH. Potential was measured vs. Ag/AgCl reference electrode

Using nanometer-sized probes, we were able to observe oxidation/reduction reactions at electrodes buried inside borosilicate glass—something that should not be possible according to conventional wisdom. Nanometer-thick layers of glass are sufficiently permeable to observe oxidation/reduction of water in either aqueous or organic media. From Fig. 5.1A one can see that the through-glass oxidation/reduction of water occurs with the total tip diameter of ~150 nm (curve 2), but not observed when it is ~1 μm (curve 1). The rupture of the insulating sheath by evolved hydrogen (Fig. 5.2) or oxygen unequivocally confirms the diffusion of water molecules through the film, and a very sensitive voltammetric test (Fig. 5.1C) provides strong evidence against the possibility of microscopic pores or cracks in the glass layer. So far, no other electroactive species—either hydrophilic or hydrophobic, ionic or neutral—were found to cross the dry glass barrier.

Voltammetry in organic solutions (Fig. 5.3) provides additional evidence for molecular diffusion through glass (as opposed to solution permeation through defects) since organic

solution does not spontaneously enter nanometer-sized holes in hydrophilic glass.[12] Importantly, no waves appeared within the entire potential range from -3 V to +3 V when no water was added to distilled DCE. The dependence of the peak current vs. c_{H_2O} for the peak occurring ~3.3 V (Fig. 5.3C) is linear for the entire range of concentrations from 1 mM to 130 mM (the latter corresponds to water-saturated DCE[13]). The linearity of the calibration curve and the detection limit of ~0.5 mM attained without any optimization suggest that voltammetry at glass-covered nanoelectrodes may become an alternative to the well known Karl Fisher titration technique[14] for determination of water in organic solvents. Obvious advantages of the nanoelectrochemical approach include an extremely small sample size and not using additional reagents.

A hydrated gel layer can be formed by soaking a glass-covered nanoelectrode in acidic solution. Unlike conventional glass pH sensors, whose thick (~0.1 μm) membrane remains largely dry when immersed in an aqueous solution, ~100-nm-thick glass covering our electrodes seems to be largely (if not completely) converted to hydrated gel. The voltammograms of water oxidation/reduction before and after the formation of hydrated gel are completely different. The hydrogen and oxygen evolution currents in Figs. 5.1 – 5.3 were produced by diffusion of water molecules through the nm-thick layer of dry glass. The currents corresponding to these processes can be recorded immediately after immersing a glass-covered nanoelectrode in aqueous solution. The response is stable and essentially time-independent on the time scale of several minutes, which is too short for the slow process of glass swelling. In contrast, hydrated gel is an aqueous environment, in which a monolayer of adsorbed water forms on the Pt surface. Accordingly, curve 2 in Fig. 5.4A exhibits characteristic voltammetric peaks corresponding to adsorption/desorption of hydrogen and oxygen and similar to those obtained at macroscopic Pt

electrodes in acidic solutions (cf. inset in Fig. 5.4A). Such peaks are not present in curve 1 obtained at a "dry" glass electrode.

$Ru(NH_3)_6^{3+/2+}$ species, which were completely blocked by dry glass (curve 1 in Fig. 5.1C), yielded a pair of well-defined cathodic and anodic peaks at a hydrated glass electrode (Fig. 5.4B). An increased peak separation, ΔE_p = 95 mV, points to a significant resistance of the hydrated glass layer that varies for different electrodes (as does the ΔE_p value). The resistive potential drop apparently depends on the thickness of the hydrogel and the surface area of Pt exposed to it. In Fig. 5.4B, the ~35 mV increase in peak separation (the peak separation expected for a reversible CV unaffected by the resistive potential drop is ~59 mV) corresponds to the glass layer resistance of ≥100 MΩ.

An unusual combination of the low (pA) current typical of nanoelectrodes and a peak-shaped CV that is normally obtained at macroelectrodes can be attributed to considerable viscosity (and, thus, low diffusion coefficients of $Ru(NH_3)_6^{3+/2+}$), which results in non-steady-state diffusion within a thin layer of hydrated gel. The time at which the diffusion in a thin layer approaches a steady state is of the order of d^2/D,[15] where d is the layer thickness. Assuming the film thickness of 100 nm and noticing that the experimental time scale in Fig. 5.4B of ~1 sec, the apparent D value is $\leq 10^{-10}$ cm^2/s.

The hydrated glass film exhibits permselectivity: in comparison with cationic $Ru(NH_3)_6^{3+}$, voltammograms of anionic $IrCl_6^{3-}$ (Fig. 5.4C) and neutral, more hydrophobic $FcCH_2OH$ (Fig. 5.4D) exhibit larger peak separations and less defined faradaic waves. The electrode surface modification by nm-thick hydrated glass may provide new opportunities for sensor preparation, protection of electrocatalysts from fouling and inhibitors, and other electrochemical applications. Another interesting possibility—electrodeposition of metals within

the glass matrix—is exemplified by nucleation and bulk deposition of Cu in hydrated gel (Fig. 5.5).

The pH response of nm-thick borosilicate glass is due to the formation of the hydrogel layer during a few hours of treatment with acidic solution. The high resistance of hydrated gel and very slow diffusion in it are consistent with the development of membrane potential across this layer. The strong dependence of the nanoelectrode potential on pH and excellent linearity of the calibration curve (Fig. 5.6) suggest that these electrodes can serve as all solid-state pH nanoprobes. The electrodes containing a buffer solution—presently the most common type of pH sensors[16]—have many disadvantages including storage problems, pressure and temperature dependence, mechanical instability, relatively large size, and fabrication cost.[17] Numerous efforts to produce solid-state pH electrodes based on iridium oxide,[18] conductive polymer composites,[19] and other sensing strategies have met with limited success.

The main advantages of a glass-coated Pt pH electrode—its microscopic size and biocompatibility—make it potentially useful for cell biology applications and other experiments in small volumes. The attainable tip size (tens of nm) is comparable to or smaller than that of the existing nanopipet-based potentiometric probes.[20] It may also be employed as a scanning probe for pH microscopy,[21] where its small size can help to significantly improve spatial resolution. At the same time, glass nanosensors are not likely replace conventional pH electrodes in routine analytical measurements because of their fragility and limited lifetime.

Borosilicate glass used in this work may not the best material for a pH sensor since its composition is different from conventional pH glass (e.g., Corning 0150 glass), and it would not be suitable for fabrication of macroscopic pH probes. A relatively slow response (minutes) can probably be improved by using more suitable glass for preparation of pH nanosensors.

Chapter VI

Atomic Force Microscopy of Electrochemical Nanoelectrodes

6.1 Introduction

The development of nanometer-sized electrodes made possible studying processes and phenomena that would not be accessible by larger electrochemical probes.[1] Nanoelectrodes were used to study electrochemistry of single molecules[2] and single nanoparticles,[3] investigate mass transport processes on the nanoscale,[4] measure rapid kinetics,[5-7] and perform quantitative experiments inside living cells.[8] Several unusual phenomena such as electrochemistry through glass,[9] surface diffusion of adsorbed redox species at the Pt/glass interface,[10] and the effects of partially formed electrical double layer[11] could only be observed in nanoscale systems.

Experiments at nanoelectrodes are often hindered by visualization difficulties. The knowledge of the electrode shape and size is essential for quantitative experiments; and significant shape irregularities (e.g., the recession of the conductive surface into the surrounding insulator) may cause very large errors in the determined kinetic parameters.[12] Neither optical nor electron microscopy provide adequate means for visualization of nanoelectrodes. The SEM resolution is not sufficiently high to characterize electrodes smaller than ~50 nm radius; moreover, insufficient z-axis resolution makes it hard to distinguish between flat, recessed, and protruding nanoelectrodes. TEM can provide a side view of a very small (e.g., $\leq$ 3 nm radius[13]) electrode, but it gives no information about the exposed metal surface. Additionally, it is not easy to use either SEM or TEM for in-situ monitoring electrochemical processes.

In most publications on nanoelectrochemistry, a nanoelectrode was assumed to be disk-shaped and flush with the surface of surrounding insulator, and its radius (a) was evaluated from the diffusion limiting current

$$i_d = 4nFDc^*a \tag{6.1}$$

where n is the number of transferred electrons, F is the Faraday constant, D and c^* are the diffusion coefficient and the bulk concentration of the redox species, respectively, and a is the disk radius. Estimating a from Eq (6.1) is problematic because steady-state voltammograms provide no information about nanoelectrode geometry, which is never perfect (see below) and has to be checked independently. The visualization issue is even more pressing in studies of surface reactions at nanoelectrodes. For instance, to investigate nucleation/growth processes, one has to relate the current response to both the initial electrode size/geometry and the change resulting from electrodeposition of metal.[14] Without a means for independent verification, such analysis can be ambiguous.

The size and geometry of a nanoelectrode can be evaluated by using it as a probe in the scanning electrochemical microscope (SECM).[15] While high SECM feedback (e.g., the tip current increasing by the factor of ~10 near the conductive surface) can provide strong evidence that a nanoelectrode is essentially flat and well polished,[7,11] a lower feedback often observed in current-distance curves is hard to interpret. Possible origins of such a response include either recessed or protruding tip geometry, surface contamination, or poor tip/substrate alignment. One should also notice that only a sharp nanoelectrode with a very thin insulating sheath can be used as an SECM probe. In this Letter we present a direct method for visualizing nanoelectrode surfaces by atomic force microscopy (AFM).

6.2 Experimental Section

Chemicals. Ferrocenemethanol ($FcCH_2OH$, 97%) from Aldrich (Milwaukee, WI) was sublimed before use. Other chemicals were used as received. Aqueous solutions were prepared from deionized water (Milli-Q, Millipore Co.).

Electrodes and electrochemical cells. Pt and Au nanoelectrodes were fabricated as described previously.[7] Briefly, an annealed 25-μm Pt or Au wire (Goodfellow) was pulled into a glass capillary under vacuum with the help of a Sutter P-2000/G laser pipet puller. The pulled electrodes were polished either on 50 nm alumina lapping tape or 100-nm diamond lapping tape (Precision Surfaces International) under video microscopic control. Pt wires were sealed into borosilicate glass, and Au wires—into soda-lime glass capillaries (Drummond; 1.0-mm o.d., 0.2-mm i.d.). Electrochemical AFM images and voltammograms were obtained in a commercial liquid cell (Park Systems), which was mounted on the stage of XE-120 scanning probe microscope, using an EI-400 potentiostat (Ensman Instruments). In a two-electrode setup, a Ag-wire was used as a quasi-reference. Current images were obtained with the nanoelectrode biased to a potential corresponding to diffusion-limited oxidation of $FcCH_2OH$, and the current was plotted as a function of lateral position of the AFM probe. SECM measurements were performed using a previously described home-built SECM instrument.[7,8]

AFM imaging. An XE-120 scanning probe microscope (Park Systems) was employed to image the nanoelectrodes in a non-contact, intermittent or contact mode, either in air or in solution; and PPP-NCHR and PPP-CONTSCR AFM probes (Nanosensors) were used for non-contact and contact imaging, respectively. An ~4.5 cm long nanoelectrode was mounted vertically with its polished surface facing the AFM probe using a homemade sample holder (Fig. 6.1) attached to

XY piezo positioning stage. The cantilever was positioned above the nanoelectrode with the help of an optical microscope. A different custom-made holder was used for liquid phase imaging. In a non-contact mode, the tip was brought within a close proximity of the sample using the approach function, and then the nanoelectrode was moved laterally in 200 nm steps to bring the AFM

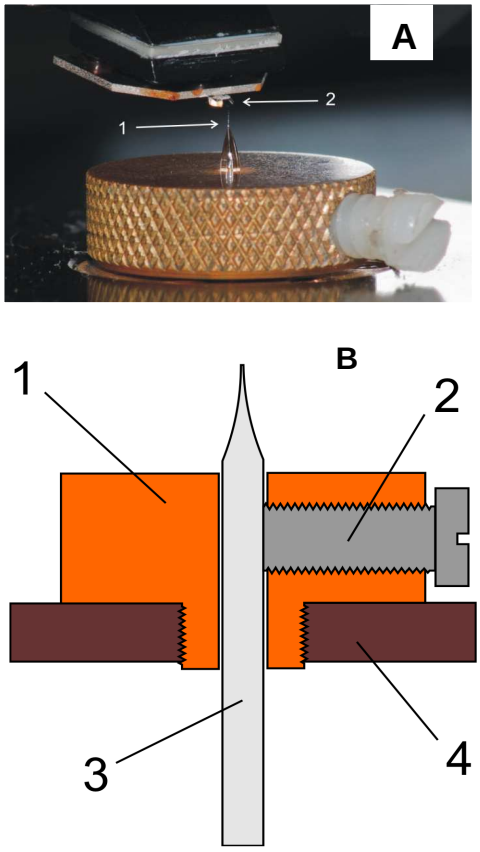

Figure 6.1. Experimental setup used for AFM imaging of nanoelectrodes in air. (A) A glass-sealed, polished nanoelectrode (1) is positioned under the AFM probe (2). (B) A scheme of the nanoelectrode holder. 1 – brass base, 2 – plastic screw, 3 –nanoelectrode, 4 – XY piezo positioning stage

probe to its apex. (In XE-120 the tip travels along z-axis, and the sample is moved in the x-y plane). The travel direction was selected to effect z-axis retraction of the piezo actuator in a close-loop mode. This corresponded to sliding of the slanted tip surface along the edge of the glass insulating sheath of the electrode. When the piezo approached its upper limit, the z-stage motor was retracted by 1 µm to maintain the z-axis piezo actuator within its range (12 µm). This

approach allows imaging of sharp objects, including needle-like SECM tips with a nm-scale thickness of the insulating sheath at the tip.

6.3 Results and Discussion

Non-contact topography imaging is very convenient for preliminary characterization of nanoelectrode geometry. An image (Fig. 6.2) was obtained in air with no direct contact between the AFM probe and the nanoelectrode and, thus, no possibility of damage or contamination of the sample surface. The electrode in Fig. 6.2A has a 25-30 nm effective radius and appears to be ~5 nm recessed into the glass insulator. The steady-state diffusion limited current to such an electrode can be calculated from Eq. (6.2)[16]

$$i_l = i_d/(1.0354 + 1.2621H + 0.01155lnH) \qquad (6.2)$$

where H is the recess depth normalized by the effective disk radius (l/a)

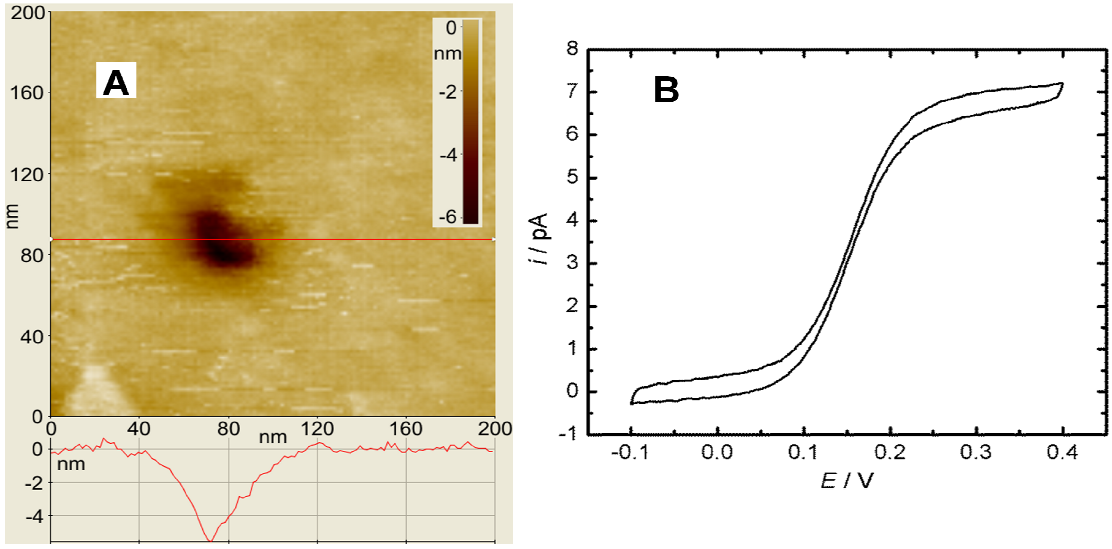

Figure 6.2. Non-contact topographic image of a polished Pt nanoelectrode in air (A) and a steady-state voltammogram of 1 mM $FcCH_2OH$ obtained at the same electrode in 0.2 M KCl solution (B). (A) The scan rate was 0.5 Hz. The red line corresponds to the shown cross-section. (B) The potential sweep rate was v = 50 mV s^{-1}.

The triangular shape of the cross-section in Fig. 6.2A is due to the convolution of the tip shape

and the sample geometry. It is possible that the tip did not reach the bottom of the cavity, and its actual depth could be somewhat larger. However, a good agreement between the AFM and voltammetric results indicates that non-contact imaging provides a reliable estimate for the effective recess depth. This slightly recessed electrode (H = 5 nm/28 nm = 0.18) is suitable for

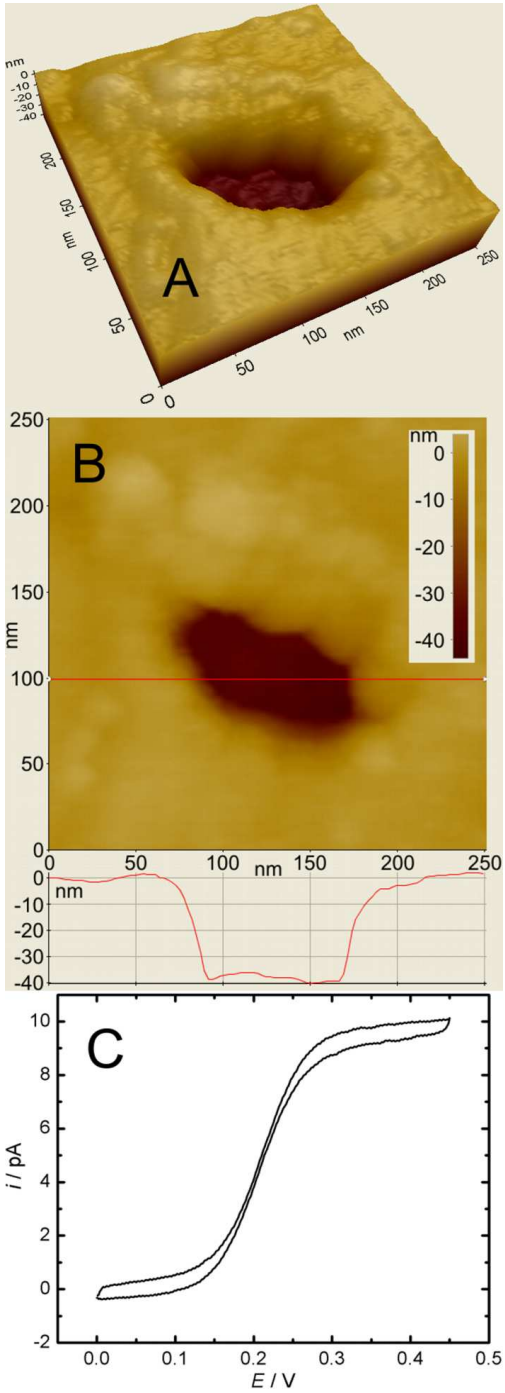

Figure 6.3. Non-contact topographic image of a recessed Pt nanoelectrode in air in 3D (A) and 2D (B) and a steady-state voltammogram of 1.2 mM $FcCH_2OH$ (C). For other parameters, see Fig. 6.2.

quantitative nanoelectrochemical experiments, but some deviations from the theoretical response could be expected if it was used for measuring electron transfer kinetics. One should notice that no existing electrochemical or microscopic technique could provide equally detailed information about nanoelectrode geometry. An image of a considerably recessed electrode is shown in Fig. 6.3A. The diffusion limiting current (~9 pA) measured in 1.2 mM $FcCH_2OH$ (Fig. 6.3C) is in good agreement with i_l = 9.4 pA calculated from Eq. (6.2) with $l \approx$

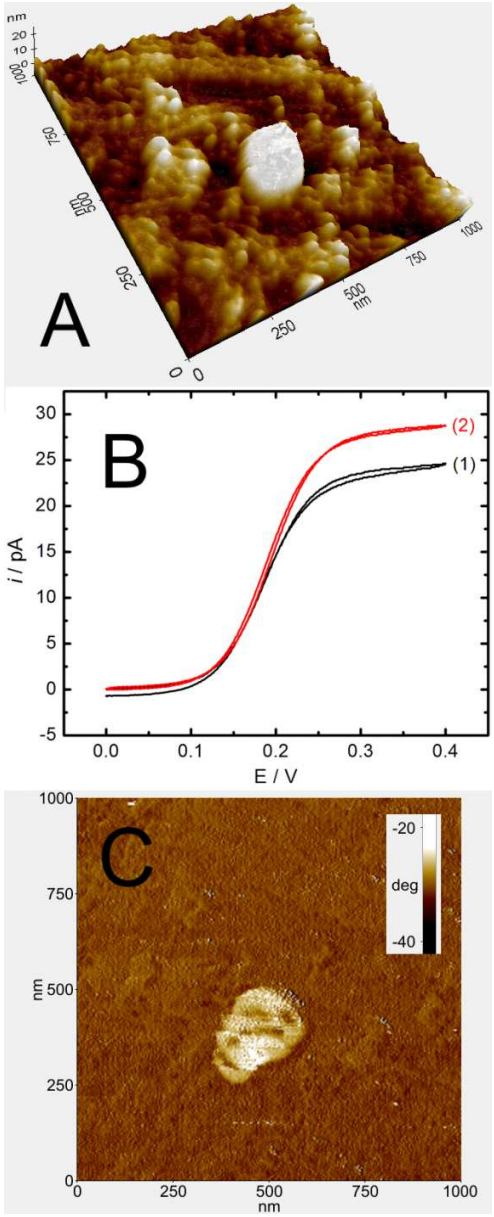

Figure 6.4. Intermittent contact mode topography (A), and phase shift (C) AFM images of a protruding annealed platinum nanoelectrode, and cyclic voltammograms (B) obtained before (1) and after (2) annealing at 120 °C for 1 hour. For other parameters, see Fig. 6.2.

40 nm, $a \approx 52$ nm found from Fig. 6.3B. From the voltammogram in Fig. 6.3C, one would not be able to tell that this electrode is recessed. The effective radius calculated from Fig. 6.3C without taking into account the recessed geometry would have been as small as 20 nm. Moreover, kinetic experiments (and other geometry-sensitive experiments) at such an electrode could yield misleading results. Recessed nanoelectrodes have been employed for different types of experiments, including measurements in ultra-small volumes.[11] AFM characterization of recessed probes can greatly improve the reliability of such experiments. In the case of a deeply recessed nanoelectrode (i.e., $l > a$), a sharper AFM probe (e.g., a carbon nanotube probe) should be used for more accurate measurement of l.

An electrode with the conductive core protruding from the glass sheath can also be characterized by AFM. The electrode imaged in Fig. 6.4A has $a \approx 83$ nm and height, $h \approx 20$ nm. The glass roughness in this case is relatively high, and to clearly distinguish between the conductive Pt surface and the surrounding glass one can compare the topographic image (Fig. 6.4A) to the phase shift image of the same electrode (Fig. 6.4C) obtained in the intermittent contact mode. The contrast in the latter is due to different interactions of the AFM probe with Pt and glass surfaces. Contact mode imaging provides better resolution than the non-contact mode, but positioning a more flexible AFM contact probe above the nanoelectrode apex is more difficult.

An essentially "perfect" flat electrode whose conductive surface is flush with the surface of surrounding insulator can be hard to visualize by non-contact AFM. A well-polished electrode in Fig. 6.5 exhibits extremely low roughness (~1 nm over a 1 μm^2 surface area) of both Pt surface and glass. The electrode active area is undetectable in the topographic image (Fig. 6.5A), whereas the voltammogram in Fig. 6.5C yields the effective radius, $a = 37$ nm. As

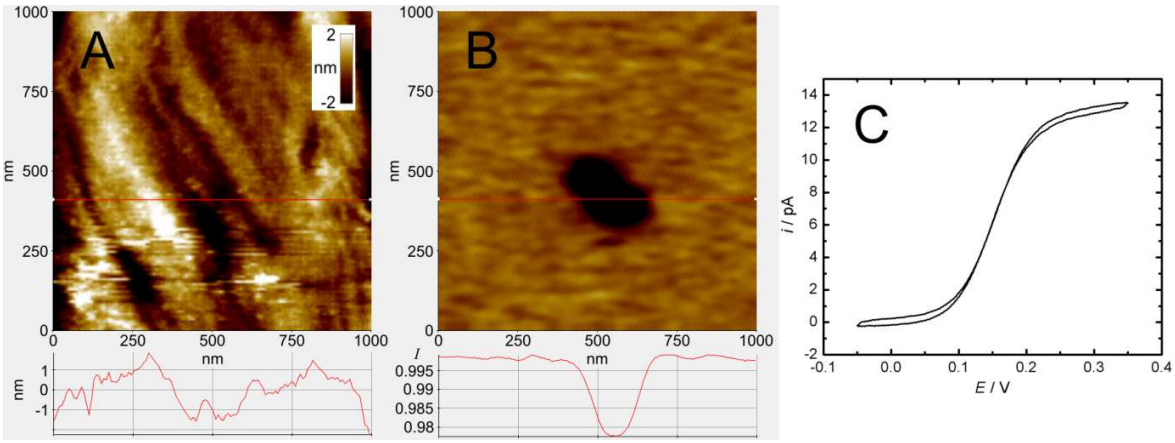

Figure 6.5. Topography (A), and substrate current (B) AFM images recorded simultaneously during non-contact imaging of a Pt nanoelectrode ($a \approx 37$ nm) with cross sections shown below images for fast scan axis direction. Scan rate: 0.5 Hz. Cyclic voltammogram (C) of the sample at 50 mV s^{-1}. AFM images and voltammogram recorded in 1.2 mM $FcCH_2OH$ in 0.2 M KCl.

discussed above, an electrode of this kind can be visualized either by phase shift imaging in a tapping mode or by lateral force imaging. Another interesting way to locate the active electrode surface is by AFM imaging in solution containing a redox mediator with simultaneous recording of the faradaic current. Burt *et al.*[17] showed that the diffusion to a micrometer-sized electrode is hindered by a non-conductive AFM probe during imaging. This effect, which is much stronger for a nanoelectrode, can be used to *in-situ* map the electrochemical activity of the surface (Fig. 6.5B). The area of decreased faradaic current in Fig. 6.5B is larger than the sample size expected from Fig. 6.5C because of the diffusion broadening effect (i.e., the effective radius of the quasi-hemispherical diffusion layer of the redox species at the nanoelectrode is $>a$) and a relatively large physical size of the AFM tip. The effective radius value, a = 37 nm, obtained from Fig. 6.5C is reliable because the electrode is flat and flush with the insulator surface (Fig. 6.5A) and

its surface reactivity is uniform (Fig. 6.5B). One should also notice that the topography of a nanoelectrode can be imaged in solution before and immediately after an electrochemical experiment, which is essential for visualization of nanoelectrochemical processes (e.g., electrodeposition of metals at nanoelectrodes[18]).

6.4 Conclusion

In summary, AFM imaging of a nanoelectrode in air and in solution can provide detailed information about its geometry and surface reactivity that would be hard to obtain by any other technique. This information is essential for reliable interpretation of nanoelectrochemical experimental data. The nanoelectrodes characterized by AFM are not damaged; they can be employed in electrochemical experiments and as SECM probes. Our experiments also revealed surprising effects of the low-temperature annealing, which can result in the recession of the Au electrode surface into glass, protrusion of Pt nanoelectrodes, and formation of nanoscale surface structures.

Chapter VII

Electrodeposition at Nanoelectrodes

7.1 Introduction

Recent progress in nanoelectrochemistry [1,2] spurred, the development of several techniques for preparation of nanometer-sized electrochemical probes with desired properties. The nanoelectrodes of various geometries, such as disks, bands, cones and recessed electrodes have been reported.[3] Most of them were made of Pt or Au by partially insulating either etched or pulled microwires or thin metal films.[4-15] For instance, Fan et al. insulated etched wires with Apiezon wax to produce conical nanoelectrodes.[7] The Unwin group fabricated Pt nanoelectrodes by coating etched wire with an electrophoretic paint.[9] Glass-sealed nanoelectrodes were prepared in White's[10b] and Zhang's[14] laboratories. We reported recently the preparation and characterization of the disk-type, polished Pt [15a] and Au [15b] nanoelectrodes with a radius, $a \geq 5$ nm. A small *RG* value (i.e., the ratio of the insulating sheath radius to *a*) of ≤ 10 allowed such electrodes to be used as tips in scanning electrochemical microscopy (SECM).[15c]

The nanoelectrodes made of metals other than Pt and Au could be potentially useful for a wide range of applications such as sensors, studies of electrocatalysis, bioelectrochemical experiments, kinetic measurements, and stripping analysis. The preparation of such electrodes is not straightforward: in some cases, the starting material (e.g., microwire) is not available; for other metals (e.g., Hg) the established fabrication techniques would not work. In this article, we report the preparation of Hg and Pt nanoelectrodes by electrodeposition of these metals on Pt and Au. Electrodeposition of a liquid metal (Hg) is a good model system for exploring feasibility of

the electrodeposition at nanoelectrodes and developing methodology to control the size and shape of the deposit. The electrodeposition of mercury on Pt and other noble metals from Hg_2^{2+} solutions is a well studied process that involves 3D nucleation/growth of essentially hemispherical droplets.[16] Unlike solid metals, the Hg surface is uniform, and defect-free; its growth is not accompanied by the formation of dendrites and other complications. Although Hg can penetrate into bulk Pt, this very slow process with the effective diffusion coefficient of ~10^{-17} cm^2/s [17b] should not affect our experiments. The electrodeposition approach was used by several groups to produce micrometer-sized Hg electrodes.[18]

Few examples of electrodeposition on nanoelectrodes have been reported to date. [19] This process may be substantially different from three-dimensional (3D) nucleation/growth phenomena at macroscopic (or micrometer-sized) electrodes, which have been extensively studied since 1950's. [20] After the application of an appropriate potential to the underlying macroscopic metal electrode, a number of essentially hemispherical nuclei form on special active sites, [21] which have been identified as various surface defects including step edges.[22] These nuclei first grow independently, then their diffusion fields begin to overlap, and eventually the growing clusters merge and form a continuous phase of electrodeposited metal. It was also suggested that only one nucleus can form and grow at a micrometer-sized electrode [23] because of the limited active site density and the existence of exclusion zones around growing crystals.[24] Thus, multiple nucleation at a nanoelectrode substrate is highly unlikely.[25] Here, the current measured at a nanoelectrode is attributed to the growth of a single metal crystal. A mechanistic study of electrodeposition at nanoelectrodes is underway in our laboratory.[26]

One of the hardest tasks in nanoelectrochemical experiments is the characterization of fabricated nanoprobes. In addition to evaluating the electrode size and geometry, one has to

show that its electrochemical response conforms to the theory and is free from artifacts, e.g., solution leakage through the metal/insulator seal. The unique features of nanoelectrode behavior can further complicate its characterization. For instance, even in the absence of leakage, the effective surface area of a nanoelectrode determined from the adsorption/desorption charge can be much larger than the geometrical area of metal exposed to solution because of the surface diffusion of adsorbed species along the metal/insulator interface.[27] Unlike our regular nanotips, the electrodes obtained by electrodeposition at polished nanoelectrodes are no longer flat or polishable. The deposited metal may be porous, thus allowing the solution species to diffuse to the underlying metal surface. Here, we used the nanoelectrodes as SECM tips to evaluate their dimensions from the approach curves.[15a, 28] The combination of these experiments with voltammetry of catalytic and non-catalytic electrochemical processes and SEM imaging provided sufficient information about geometric and electrochemical properties of prepared nanoelectrodes. Smaller metal clusters can also be produced and characterized in a similar manner.

In addition to its fundamental significance, electrodeposition of metals is at the core of various industrial applications from gold and chromium plating to fabrication of interconnects in electronic circuits to preparation of electrocatalysts for energy storage[29]. The key to control the morphology of deposited metal is to understand the mechanism three-dimensional nucleation and growth—the initial stages of many electrodeposition processes[30]. The random nature of nucleation and the difficulties in quantitative analysis of the signal, which is produced by a large number of growing crystals interacting with each other, impeded electrochemical studies of these processes. Despite the development of approximate analytical models [31-33], more exact numerical simulations[34,35] and statistical analysis [36,37], the extraction of numerous kinetic,

thermodynamic and transport parameters from experimental data is not straightforward. Open questions remain about the nature and density of the insipient nucleation sites on the surface [38], the time lag [37], the dimensions of an "exclusion zone", i.e., the area around a growing crystal where no new nuclei can be formed [39], and the growth rate of a nm-sized nucleus [40].

An intriguing possibility is to study nucleation/growth of metals at a microscopic electrode surface, on which only a single nucleus can be formed, and to use imaging techniques to facilitate the interpretation of the electrochemical data. In earlier studies, the assumption was that a micrometer-sized electrode is sufficiently small to observe the formation and growth of a single nucleus[41,42]. More recent studies showed that two nuclei can form within a submicrometer distance from each other [43]. Moreover, the possibility of multiple nucleation at extremely small (e.g., >5 nm) carbon electrodes was suggested [44]; however, with no adequate characterization of such electrodes, this claim is hard to validate.

Here we used electrochemical techniques and AFM to investigate nucleation/growth of silver on well characterized nanometer-sized Pt electrodes. AFM was used previously to image metal nuclei formed on step edges of graphite surfaces [45], monitor the formation of bimetallic micro- and nanoparticles[43] and study the growth of metal nuclei as a function of time and overpotential[46]. The combination of AFM with nanoelectrodes allowed us to probe nucleation/growth of nanocrystals on individual active sites.

7.2 Experimental Section

Chemicals. Mercury (I) nitrate dihydrate was obtained for Sigma Aldrich. Hexaammineruthenium (III) chloride (99%) was from Strem Chemicals. **.** Silver Sulphate was obtained from Sigma Aldrich. Ferrocene (Fc, 98%; Aldrich) was sublimed twice before use. Tetrabutylammonium perchlorate (Fluka) was used as supporting electrolyte. KNO3 and KCl

(99+%, Aldrich) were used as supporting electrolytes. H_2SO_4, $HClO_4$, HCl and hydrogen hexachloroplatinate (IV) hydrate from Aldrich were used as received. Acetonitrile (Aldrich) was used to prepare organic solutions. Aqueous solutions were prepared from deionized water (Milli-Q, Millipore Co.).

Electrodes and electrochemical cells. The fabrication of the laser-pulled Pt nanoelectrodes was described previously.[15] Briefly, an annealed 25-μm Pt wire (Goodfellow) was pulled into a borosilicate capillary (Drummond; 1.0-mm o.d, 0.2-mm i.d.) under vacuum with the help of a Sutter P-2000/G laser pipet puller. The pulled electrodes were polished on 50 nm lapping tape under video microscopic control, and washed by distilled water. The effective radius of an electrode was evaluated from steady-state voltammetry. Recessed Pt electrodes were prepared as discussed in ref. 29a. The two-electrode setup with a Ag/AgCl reference electrode was used for voltammetry, chronoamperometry, and SECM experiments, except for Hg deposition experiments, where a mercury pool was used as a quasi-reference to avoid an effect of Cl^- on this process.

Instrumentation and procedures. SECM measurements were performed using a previously described home-built SECM instrument.[15] Chronoamperometric and cyclic voltammetric experiments were carried out using either an EI-400 bipotentiostat (Ensman Instruments, Bloomington, IN) or a BAS-100B electrochemical analyzer (Bioanalytical Systems, West Lafayette, IN). To remove oxygen, the solutions were purged with high-purity nitrogen before and during the experiments. All experiments were performed at room temperature ($23 \pm 2\ ^oC$) inside a Faraday cage. SEM images were obtained using a field emission scanning electron microscope (Zeiss Supra 55 VP at CCNY electron microscopy facility) with no conductive coating applied to nanoelectrodes.

AFM imaging. An XE-120 scanning probe microscope (Park Systems) was employed for imaging nanoelectrodes and electrodeposited silver. PPP-NCHR AFM probes (Nanosensors) were used for non-contact imaging in air. Imaging in solution was performed with PPP-NCH AFM probes (Nanosensors).

The procedures for AFM imaging of nanoelectrodes either in air or in solution were developed recently (*22*). Briefly, a nanoelectrode was mounted vertically with its polished surface facing the AFM probe using a homemade sample holder, and the cantilever was positioned above it with the help of an optical microscope. In a non-contact mode, the tip was brought within a close proximity of the sample using the approach function, and then the nanoelectrode was moved laterally in 200 nm steps to bring the AFM probe to its apex. The travel direction was selected to effect z-axis retraction of the piezo actuator in a close-loop mode. This corresponded to sliding of the slanted tip surface along the edge of the glass insulating sheath of the electrode. When the piezo approached its upper limit, the z-stage motor was retracted by 1 µm to maintain the actuator within its range (12 µm).

Electrodeposition of silver for imaging on the electrode was carried out in a commercial liquid cell (Park Systems), which was mounted on the stage of the XE-120 scanning probe microscope. A Pt nanoelectrode was inserted in solution containing Ag_2SO_4 and 0.1 M H_2SO_4. After conditioning the working nanoelectrode at +200 mV for several seconds to remove traces of Ag, its potential was stepped to -90 ± 10 mV vs. Ag reference (slightly different potential values were used in different experiment, depending on the electrode size and other conditions) using Multi Clamp 700B. After each deposition experiment, a non-contact mode topographic AFM image of the nanoelectrode was obtained in situ. Then, the silver deposit was striped by

biasing the electrode at +200 mV vs Ag wire reference, and another AFM image of the same electrode was obtained

7.3 Results and Discussion

Hg deposition. Cyclic voltammograms (CVs) of Hg deposition at polished Pt nanoelectrodes were obtained to characterize this process and select suitable experimental conditions for bulk deposition. A typical CV obtained at 55-nm-radius Pt electrode in 50 μM $Hg_2(NO_3)_2$ solution (Fig. 7.1) exhibits a characteristic hysteresis appearing after the potential sweep reversal and a sharp anodic peak of Hg stripping; both features are typical of metal nucleation/growth CVs.[47] The presence of the reverse cathodic wave points to the hemispherical-type geometry of the growing nucleus, whose surface area continues to increase with time after the change in the potential sweep direction. No such feature would be observed for two-dimensional (layer-by-layer) electrodeposition. The potential of the Hg quasi-reference in a 50 μM $Hg_2(NO_3)_2$ solution was found to be +0.462 mV vs. Ag/AgCl. The cathodic diffusion limiting current region in Fig. 7.2 ($E \lesssim$ -150 mV vs. Hg quasi-reference) corresponds to $E \lesssim$ 300 mV vs. Ag/AgCl.

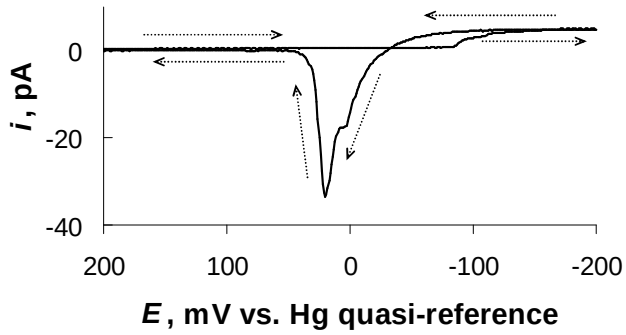

Figure 7.1. Cyclic voltammogram of electrodeposition/stripping of Hg at a 55-nm radius Pt electrode. Solution contained 50 μM $Hg_2(NO_3)_2$ and 0.125 M $HClO_4$. The potential sweep rate, ν = 50 mV/s. Arrows show the potential sweep direction.

Accordingly, in chronoamperograms of Hg deposition obtained by stepping the electrode potential to -100 mV vs. Ag/AgCl (Fig. 7.2A), the current is essentially proportional to $t^{1/2}$ (Fig. 7.2B), as expected from Eq. (1) that describes diffusion-controlled growth of a single hemispherical nucleus [48]

$$i = 2^{3/2}\pi nFD^{3/2}c^{3/2}V_M{}^{1/2}t^{1/2} \qquad (7.1)$$

where n is the number of transferred electrons, D and c are the diffusion coefficient and bulk concentration of ions, V_M is the molar volume of the deposited metal, and $t = 0$ is the time at which the nucleus was born. The analysis of the more complicated initial portion of the current transient will be presented elsewhere. [26] Electrodeposition of Hg at micrometer-sized electrodes involved the formation of multiple nuclei, which subsequently coalesced until a full hemisphere was formed. This process produced sharp features in the current-time deposition curves.[18b] The absence of such discontinuities in Fig. 7.2 is consistent with the growth of a single nucleus at a nanoelectrode.

The volume of the deposited metal can be found from the charge (Q), obtained by integrating the chronoamperometric current

$$V = QV_m/nF \qquad (7.2)$$

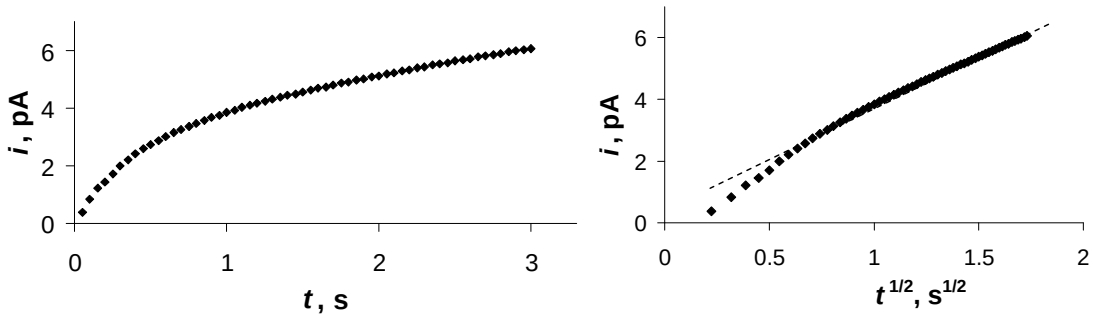

Figure 7.2. Potentiostatic transient of Hg deposition at a 52 nm Pt electrode from 50 μM $Hg_2(NO_3)_2$ solution (A) and the corresponding i vs. $t^{1/2}$ dependence (B). The dashed line in B is shown as a guide.

One should notice that the volume found from Eq. (7.2) is independent of the deposit geometry. Neglecting relatively minor deviations occurring in the short-time region,[26] the radius of a hemispherical nucleus is

$$r = (2DcV_m t)^{1/2} \quad (7.3)$$

and the time required for a nucleus to cover the entire surface of the underlying disk electrode is

$$\tau = a^2/(2DcV_m) \quad (7.4)$$

where a is the disk radius. Clearly, the smaller the electrode, the shorter the timescale of the deposition experiment. With the diffusion coefficient of Hg_2^{2+}, $D = 0.96 \times 10^{-5}$ cm^2/s, [16a] and V_m = 14.86 cm^3/mol, one obtains τ = 30 ms for a = 30 nm and c = 1 mM. The reliability of current–time curves in this case may be compromised by instrumental problems because of the difficulties with measuring low (pA) currents on the ms or sub-ms time scale. To avoid this problem, we will carried out chronoamperometric experiments with low metal ion concentrations in solution (i.e., 10 – 50 μM), thus extending the experimental timescale from the ms range to seconds.

The assumption of the hemispherical shape of a growing nucleus—and the resulting Eqs. (7.1), (7.3) and (7.4)—is a good approximation for electrodeposition at "infinitely large" planar electrodes. [20] However, a nucleus growing on a nanoelectrode surface can reach its edge, i.e., the boundary between the underlying metal and glass insulator. Previous results obtained at micrometer-sized electrodes as well as our data (see below) suggest that hydrophobic mercury droplets do not propagate over the glass surface. When the nucleus is formed near the disk center (which, apparently, was the case in Fig. 7.1), it gradually covers the entire disk surface and continues to grow to form a spherical cap larger than a hemisphere. The corresponding chronoamperogram is well shaped and in accordance with Eq. (7.1). By contrast, a droplet that

forms at the disk periphery gets distorted upon reaching the disk edge. The adjustments in its shape can be detected in the *i* vs. t deposition curve (not shown). Eventually, the deposited Hg attains a hemispherical shape, and the applicability of Eqs. (7.1) – (7.4) can be verified.

We explored several independent ways of checking the size and shape of the Hg deposit. In Figure 7.3, the Pt disk radius (a = 69 nm) was determined from the steady-state voltammogram of 2 mM $Ru(NH_3)_6^{3+}$ obtained before deposition of mercury (blue curve in Fig. 7.3A). Mercury was deposited at this electrode by stepping its potential to –100 mV vs. Ag/AgCl for 3.5 s. According to Eq. (7.4), with c = 50 μM, the time required for the complete coverage of the disk surface is τ = 3.2 s. Thus, the shape of deposited Hg was expected to nearly hemispherical with the effective radius close to 69 nm. The ratio of the limiting currents of $Ru(NH_3)_6^{3+}$ in Fig. 7.3A obtained before (blue curve) and after (pink curve) deposition of mercury is 1.5 in good agreement with the theoretical prediction ($i_{hemisphere}/i_{disk} = 2\pi/4 = 1.57$[49]).

The completeness of the Pt surface coverage by Hg was confirmed by comparison of voltammograms of proton reduction in an acidic solution (Fig. 7.3B) obtained before (blue) and after (pink) the deposition. A significant shift (~0.5 V) of the hydrogen wave in the cathodic direction in the latter voltammogram and the absence of a detectible pre-wave at more positive

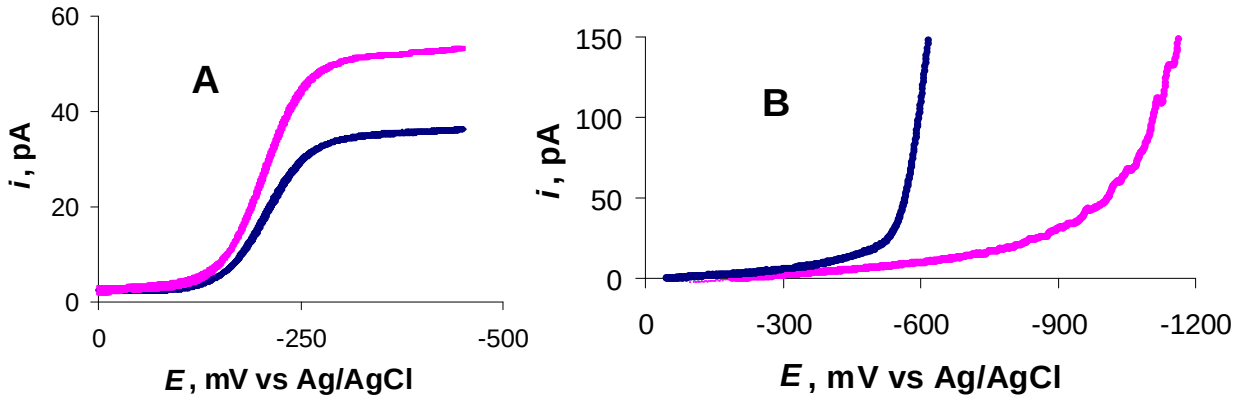

Figure 7.3. Voltammograms obtained in 2 mM $Ru(NH_3)_6Cl_3$ (A) and 0.01 M HNO_3 solutions before (blue) and after (pink) the electrodeposition of Hg on the surface of a 69 nm Pt electrode.

potentials confirm that the catalytic Pt surface was completely screened by Hg.

Figure 7.4 shows an SECM approach curve obtained with the same mercury-covered Pt electrode that was employed for voltammetric experiments in Fig. 4. The experimental current vs. distance curve (symbols) fits well the theoretical curve (green) calculated for a hemispherical electrode, according to ref. 50. The hemisphere radius found from the fit (67 nm) is in a good agreement with the Pt tip radius, a = 69 nm. One should notice that it would be impossible to fit this experimental approach curve to the theory for a disk-shaped tip (blue curve).

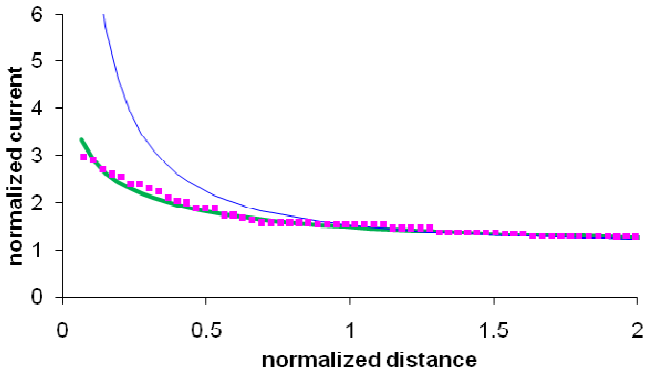

Figure 7.4. Experimental current vs. distance curve (symbols) obtained with a Hg tip approaching a conductive Au substrate. Solution contained 2 mM $Ru(NH_3)_6Cl_3$. The corresponding theoretical curve (green line) was calculated for a 67 nm hemisphere.[33a] Blue curve is the theory for a disk shaped tip.[28]

Additional information about size and shape of Hg nanoelectrodes can be obtained from deposition/dissolution transients. The charge obtained by integrating the Hg deposition chronoamperogram (not shown) obtained at the aforementioned 69-nm-radius Pt electrode (8.2 pA) corresponds to ~20% larger a value of 84.6 nm. The last current value in that i vs. t curve (4.4 pA) is reasonably close to that expected for the steady-state diffusion limiting current of 50 μM Hg_2^{2+} to a 69-nm-radius hemisphere, $i_{hemisphere} = 2\pi zFDca$ = 4.0 pA.

Major differences can be expected between nucleation/growth processes occurring on nanoelectrodes and on micrometer-sized electrodes. The reported values of the active site density on metal surfaces (N_0) are in the range $10^4 < N_0 < 10^{10}$ cm^{-2}, [51] and typically N_0 does not exceed ~10^8 cm^{-2}. Thus, the expected number of active sites on the surface of a ~30-nm-radius electrode is <<1. Thus, our

research is aimed at investigating the feasibility and mechanism of electrodeposition of metals at nanoelectrodes.

The results indicate that Hg can be electrodeposited at nanoelectrodes of this size with two possibilities: either an Hg droplet still nucleates in the absence of an active site, or it starts growing on the entire surface of the nanodisk forming a spherical cap. A simple theory assuming diffusion-controlled quasi-steady-state growth (i.e., steady-state diffusion to the growing Hg surface) was developed for these two cases.[50] The main difference between the two dimensionless current–time working curves is that the initial current value for the growing nucleus is close to zero, while in the spherical cap model it is equal to the diffusion limiting current of Hg_2^{2+} to the nanodisk surface. Figure 7.5 shows an example of two different growth

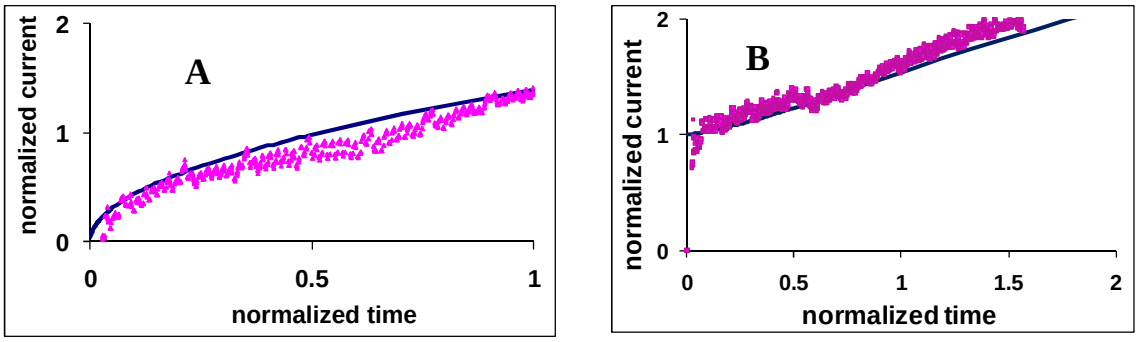

Figure 7.5. Theoretical (blue) and experimental (pink) current - time curves for a growing hemispherical nucleus (A) and a spherical cap (B) obtained at 60 nm radius Pt electrode in 100 µM of $Hg_2(NO_3)_2$ and 0.1M HNO_3. The potential is stepped to -50mV and -200mV vs Hg quasi-reference in A and B respectively. [5]

mechanisms of Hg at a Pt nanoelectrode at different over potentials. The adjustable parameter used to fit the data to the theory is the electrode radius.

The study of the formation and growth of single Hg nuclei should yield answers to fundamental questions about the initial steps of electrocrystallization at nanoelectrodes. For example, what is the rate-limiting step of this process? It was recently suggested that the kinetics of the early stage electrodeposition at macroscopic electrodes is controlled by surface diffusion

and adsorption.[6] In contrast, at a nanoelectrode, the surface diffusion control is possible only on the extremely short time scale (i.e., μs). Using the developed methodology, it should be possible to prepare 5–10 nm-radius electrodes and study the catalytic properties of such clusters.

Ag deposition. we used electrochemical techniques and AFM to investigate nucleation/growth of silver on well characterized nanometer-sized Pt electrodes. AFM was used previously to image metal nuclei formed on step edges of graphite surfaces[54], monitor the formation of bimetallic micro- and nanoparticles[52], and study the growth of metal nuclei as a function of time and overpotential[55]. The combination of AFM with nanoelectrodes allowed us to probe nucleation/growth of nanocrystals on individual active sites.

A cyclic voltammogram (CV) of Ag electrodeposition at the 100-nm-radius polished Pt electrode (Fig. 7.6A) shows a characteristic hysteresis appearing after the potential sweep reversal and a sharp anodic peak of Ag stripping; both features are typical of metal nucleation/growth CVs at macroscopic electrodes[56]. The potentiostatic transient of Ag deposition (Fig. 7.6B) was induced by stepping the potential of the same nanoelectrode from 300 mV to -120 mV vs. Ag quasi-reference. After the initial charging current spike, the current increased proportionally to the square root of time, according to Eq. (7.5)

$$i = \pi zF(2Dc)^{3/2}V_M^{1/2}(t-\tau)^{1/2}\left[1-\exp(\frac{zF\eta}{RT})\right]^{3/2} \qquad (7.5)$$

where z = 1 is the ionic charge, F is the Faraday constant, D and c are the diffusion coefficient and bulk concentration of Ag^+, V_M is the molar volume of silver, η is the overpotential, t is the time, and τ is the time at which the nucleus birth[57]. Eq. (7.5) describes diffusion-controlled growth of a hemispherical nucleus. The agreement between the experimental transient (black curve in Fig. 7.6B) and theoretical curve (red curve) is surprisingly good, keeping in mind the

absence of adjustable parameters in Eq. 7.5 and inevitable imperfections in a solid Ag nucleus, which cannot grow as a perfect hemisphere.

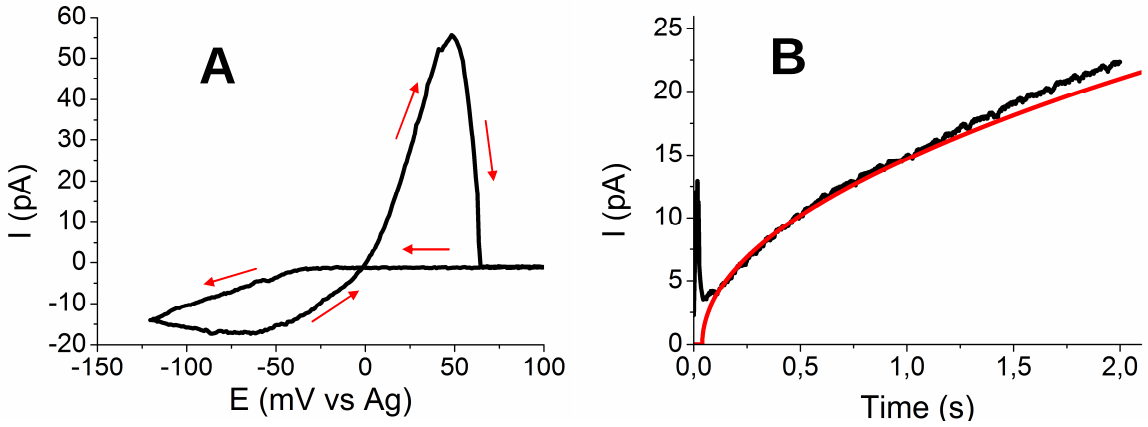

Figure 7.6. Cyclic voltammogram (A) and potentiostatic transient (B) of Ag electrodeposition at a 100-nm-radius Pt electrode. Solution contained 100 μM Ag_2SO_4 and 0.1 M H_2SO_4. (A) The potential sweep rate, ν = 50 mV/s. Arrows show the potential sweep direction. (B) Theoretical curve (red) was calculated from Eq. (1) with D = 1.5 x 10^{-5} cm^2/s [58].

The low concentration of silver ions (200 µM) resulted in a relatively long deposition time, i.e., ~1.5 s required for the nucleus radius to reach the value of 100 nm corresponding to the effective radius of the underlying Pt electrode. The recorded current transient is due to a single Ag nucleus whose growth is controlled by diffusion of Ag^+ in solution. This finding can be compared to the results in ref. 25, where TEM was used to monitor *in-situ* the growth of similarly sized Cu clusters. The growth rate of an individual crystal was evaluated by measuring its size of as a function of time. However, the overlap of the diffusion layers of multiple nuclei growing on a macroscopic electrode surface complicated the data analysis, and discrepancies were found between the growth kinetics measured for individual nanoclusters and the predictions of conventional theory.

Figure 7.7 shows two Ag deposition transients obtained at a much smaller electrode ($a \approx$ 20 nm) by stepping its potential to η = -90 mV. At a higher Ag^+ concentration (20 mM; Fig. 2A), the deposition time for a 20-nm-radius nucleus was only ~2.5 ms. The experimental data fitted to Eq. (7.5) corresponds to the nucleus growth essentially from the moment of its formation (radius, r < 3 nm) until its radius becomes larger than that of underlying Pt surface. With a lower Ag^+ concentration (0.2 mM; Fig. 7.7B), the same process was monitored on a much longer time scale. Overall, Figs. 7.6 and 7.7 show that the electrodeposition of a single Ag nucleus conforms to the classical diffusion-based theory over four orders of magnitude in time. The topographic AFM image obtained before Ag deposition (Fig. 7.7C) shows that the electrode

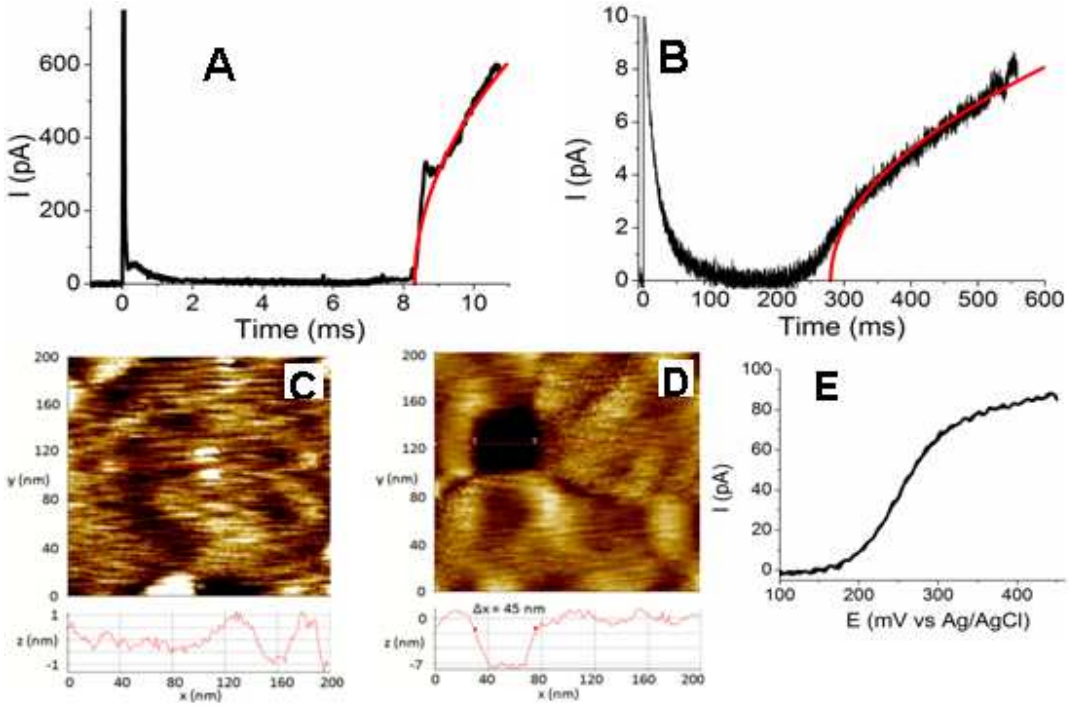

Figure 7.7. Potentiostatic transients of Ag electrodeposition (A,B), topographic AFM images (C,D) and steady-state CV of FcMeOH oxidation (E) obtained at the same ~20-nm-radius Pt electrode. Solution contained 100 μM Ag_2SO_4 and 0.1 M H_2SO_4. (A) The potential sweep rate, ν = 50 mV/s. Arrows show the potential sweep direction. (B) Theoretical curves (red) in (A) and (B) were calculated from Eq. (1).

surface is flat and well polished with ~1 nm roughness. The Pt surface is flush with the surrounding glass insulator and cannot be distinguished from it. [59] To visualize the Pt surface, an ~12-nm-thick layer of Pt was removed electrochemically[60] after the Ag deposit was dissolved. The radius of the resulting recessed electrode (Fig. 7.7D) was ~20 nm in accord with the value calculated from the steady-state voltammogram (Fig. 7.7E).

The comparison of current transients in Figs. 7.6B, 7.7A and 7.7B shows strong dependence of the extent of the nucleation time lag (τ) can vary significantly. The dependence of τ on the electrode size, concentration of Ag^+ and deposition overpotential is shown in Table 1. Overall, the τ values in Table 7.1 are much shorter than the second-scale delay times measured previously at much larger electrodes.[53] The differences can be attributed to much higher noise and equipment limitations preventing low current measurements on a short time scale at macroscopic electrodes.

Table 7.1. The effects of the electrode radius (a), overpotential (η), and Ag ion concentration on the nucleation time lag (τ). Each τ value in the table is the average obtained from 20 transients.

a (nm)	c_{Ag^+} (mM)	τ (ms)		
		η = -50 mV	η = -80 mV	η = -100 mV
20	0.2	1731 ± 204	717 ± 74	173 ± 30
20	20	221 ± 34	36.3 ± 7.1	7.2 ± 2.9
200	0.2	66 ± 19	14.5 ± 1.7	6.7 ± 0.4
200	20	68 ± 35	4.7 ± 1.1	2.0 ± 0.9

As can be expected from previously developed theory, τ decreases with increasing electrode radius, metal ion concentration, and overpotential. A very strong effect of the overpotential can be attributed to the changes in nucleation rate constant (A), active site density (N_0) and the surface concentration of Ag adatoms. All these quantities are supposed to increase exponentially with increasingly negative η[61]; and so the change in η from -50 mV to

-100 mV results in the decrease in τ by the factor of 10 to 30 for all c_{Ag^+} and a values in Table 7.1.

The time lag decrease with increasing c_{Ag^+} should be due to the increasing concentration of Ag adatoms because A and N_0 are independent of ion concentration. The effect of c_{Ag^+} on τ is similar at two higher overpotentials (i.e., η = -80 mV and -100 mV) and somewhat lower at η = -50 mV. Interestingly, this effect is much more significant at a = 20 nm electrode than at the larger (200 nm) electrode. A marked decrease in τ at a larger a can be related to the increased number of nucleation sites; the larger this number the higher the probability of the nucleus formation within a given time period. Typical values reported in the literature for the density of latent nucleation sites vary over a wide range, 10^4 cm^{-2} < N_0 < 10^{10} cm^{-2} (*24*). Even for the largest value, N_0 = 10^{10} cm^{-2}, the expected number of active sites on the surface of a 20-nm-radius electrode is <1. For a 200 nm electrode, the number of sites can be >1. Further insight was obtained by combining nanoelectrochemical nucleation experiments with AFM imaging (Figs. 7.8 and 7.9).

Figure 7.8 shows four pairs of noncontact mode topographic AFM images obtained *in situ* before and after four consecutive Ag electrodeposition experiments. Fig. 7.8A shows a ~50-nm-radius electrode with the Pt surface recessed by 20 nm into glass insulator. This slight recess facilitated the visualization of the Pt surface (cf. Fig. 7.7C and 7.7D) and also resulted in significantly more uniform current distribution near the edge of the conductive surface[62], thus alleviating concerns about possible edge effect on nucleation/growth kinetics. Ag was deposited by stepping the electrode potential from +200 mV to -100 mV vs. Ag quasi-reference in solution containing 5 µM Ag_2SO_4 for ~3 s. A low concentration of Ag^+ resulted in a slow growth of a small ($r \approx$ 10 nm) nucleus, which can be seen in Fig. 7.8B. After stripping the Ag deposit, an

image of the same Pt electrode in Fig. 7.8C was essentially identical to that in Fig. 7.8A. The same deposition protocol was used to deposit a new nucleus (Fig. 7.8D) on the same electrode; and the deposition/dissolution sequence was repeated several times (Figs. 7.8A – 7.8H).

The formation of only one nucleus in every deposition experiment conducted at the 50 nm electrode (Fig. 7.8) is in line with existing theory because the probability of multiple nucleation on the electrode of this size is extremely low[63]. The size of the grown nucleus varied significantly because of the random nature of the nucleation, however, it always formed on the same spot (within ~5 nm uncertainty due to the finite size of the imaged nucleus and limited spatial resolution of AFM images). This finding suggests that only one latent nucleation site existed on the electrode surface. The corresponding effective site density, $N_0 \approx 1.3 \times 10^{10}$ cm^{-2} is higher than the literature values, which is consistent with the presence of only one active site on the electrode surface.

Except for Penner's finding that electrochemical nucleation on graphite surfaces is confined to step edges[54], little is known about the nature of nucleation sites. It is common to assume that such sites can appear and disappear in the course of an electrodeposition experiment. The data in Fig. 7.8 shows clear evidence of a persistent nucleation site that remains active after several deposition/stripping cycles.

Fig. 7.9 shows AFM images representing four deposition/stripping cycles conducted at a larger nanoelectrode (a = 190 nm, d = 12 nm). Similarly to Fig. 7.8, a nucleus growing on the same spot can be seen in Figs. 7.9B, 7.9D, and 7.9H. However, this nucleus is not present in Fig 7.9F, and instead a nucleus formed at a different location, ~200 nm away from the first one, can be seen. Moreover, Fig. 7.9D shows both nuclei growing simultaneously. Apparently, there were two latent nucleation sites on the surface of a 190-nm-radius electrode, and Ag nucleated

randomly either on the first or the second or both sites. The effective site density, $N_0 \approx 8.8 \times 10^8$ cm^{-2} in this case was within the range of literature values.

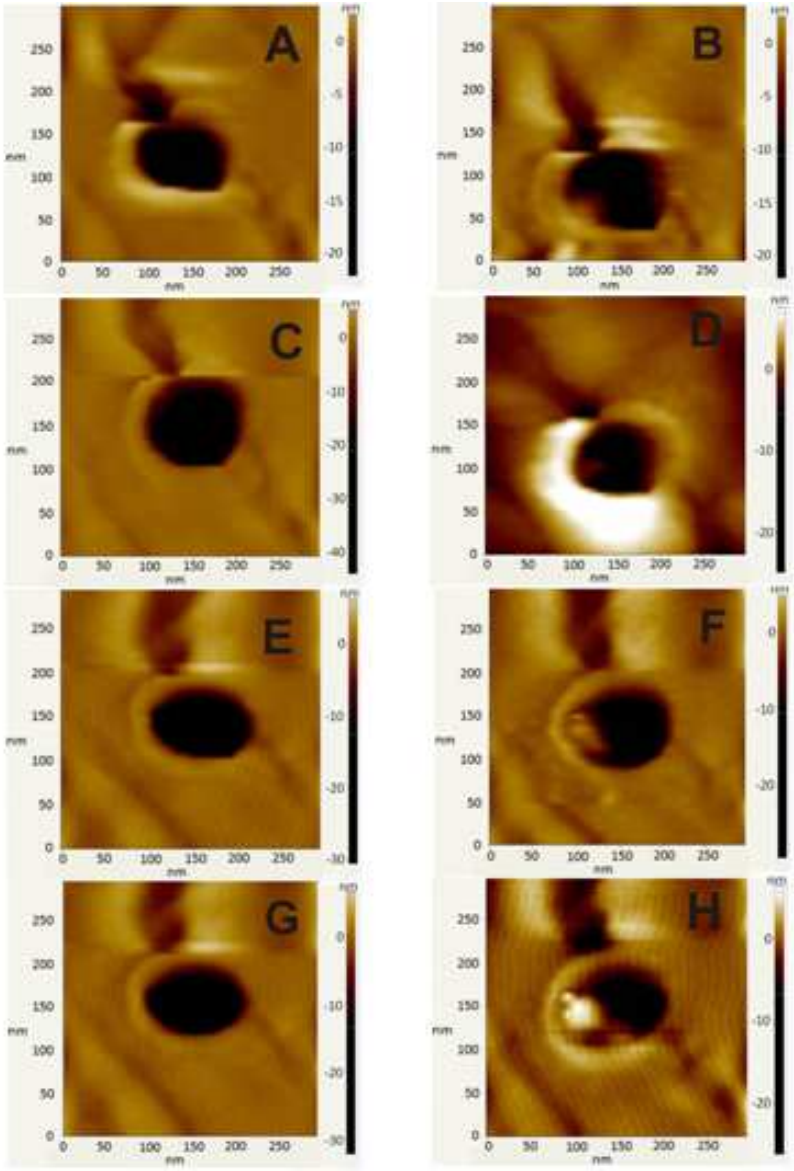

Figure 7.8 *In-situ* AFM images obtained before and after successive electrodeposition experiments at the same 50-nm-radius Pt electrode. Images A, C, E and G were recorded before, and images B, D, F and H - after the 1st, 2nd, 3rd, and 4th depositions, respectively. The deposition potential was -100 mV vs. Ag quasi-reference. Before each deposition, the electrode potential was held at +200 mV to dissolve previously deposited metal.

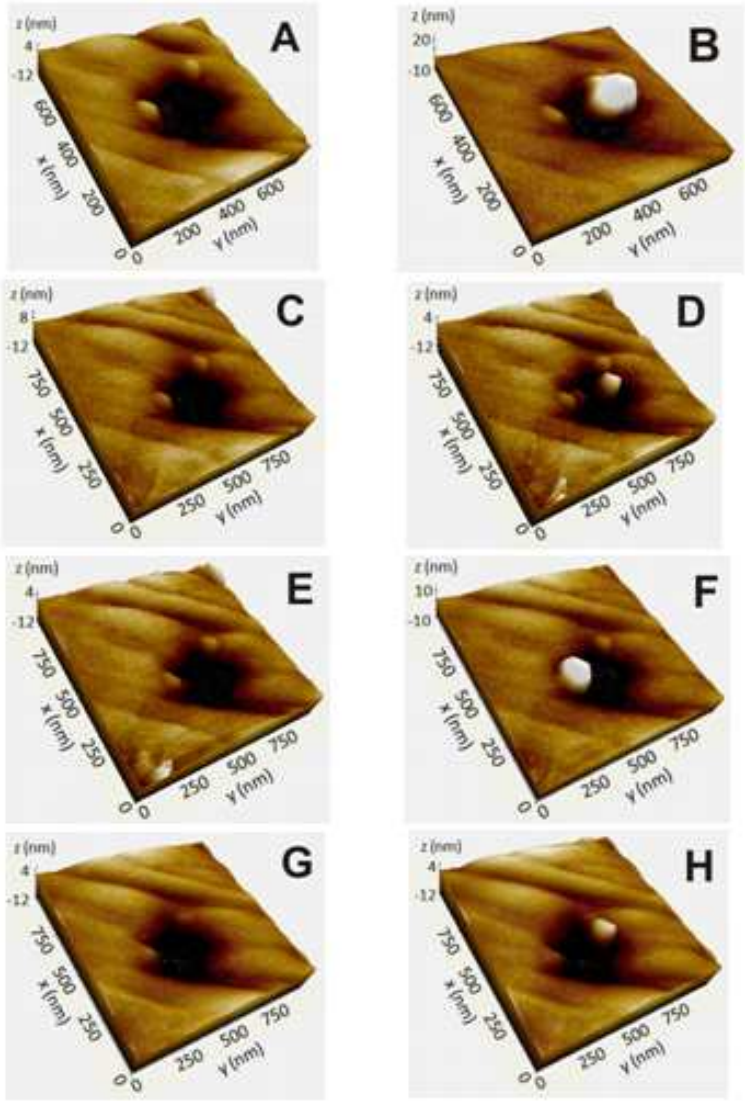

Figure. 7.9. *In-situ* AFM images corresponding to four Ag electrodeposition experiments at the same 190-nm-radius electrode. Images A, C, E, and G were recorded before, and images B, D, F, and H - after the 1st, 2nd, 3rd, and 4th depositions, respectively. Solution contained 1 mM Ag^+ and 0.1 M H_2SO_4. The deposition potential was -85 mV vs. Ag quasi-reference. Before each deposition, the electrode potential was held at +200 mV to dissolve previously deposited metal.

7.4 Conclusion

Electrochemical nanoprobes prepared from metals other than Au and Pt can be useful for a wide range of analytical and physicochemical applications from high sensitivity stripping analysis (Hg) to pH nano-sensors (Ir) to studies of electrocatalysis (Pd, Co, Au, Ni and other electrodes). We have explored several strategies for fabrication of nanometer-sized electrodes

and metal clusters by electrodeposition at flat or recessed nanoelectrodes. While preparation of micrometer-sized electrodes by electrodeposition is relatively straightforward, analogous experiments at nanoelectrodes are more challenging because of the impossibility of optical control and the lack of established methodology for metal deposition on the nanoscale. Well-shaped hemispherical nanoelectrodes were produced by depositing Hg at the surface of flat polished Pt tips. The size and geometry of such electrodes were verified independently by voltammetric, coulometric and SECM measurements.

Although a nanoelectrode produced by deposition of a solid metal can yield well-shaped voltammograms, its geometry is hard to characterize and its surface is not polishable. These problems can be overcome by etching a flat (e.g., Pt) nanoelectrode and filling the resulting nanocavity with a different metal. By selecting suitable deposition time and keeping the metal ion concentration sufficiently low (μM), one can precisely control the amount of the deposited metal to obtain a flat polishable nanoelectrode. Such nanoelectrodes are suitable for quantitative SECM experiments.

Three-dimensional nucleation and growth on active surface sites are important initial stages of electrodeposition of metals. Electrochemical studies of these phenomena are greatly complicated by the formation of multiple crystals interacting with each other. The Ag electrodeposition on the surface of well-characterized, nanometer-sized Pt electrodes and the measured nucleation/growth kinetics of individual Ag crystals by combination of nanoelectrochemistry and AFM was investigated. Basic parameters, including the number of surface active sites, the delay time, and the number of growing nuclei, were directly accessed from current transients and confirmed by in-situ AFM imaging.

Chapter VIII

Nanoelectrodes for Determination of Reactive Oxygen and Nitrogen Species inside Murine Macrophages

8.1 Introduction

Macrophage cells are essential for the performance of the immune system. Their activation, either under normal biological conditions or by specific biochemical activators *in vitro*, results in the production of reactive oxygen and nitrogen species (ROS and RNS) and creation of a large number of vacuoles (phagosomes and phagolysosomes, see Fig. 8.1A).[1-3] These vacuoles play an important role in phagocytosis—a mechanism used by the immune system to remove pathogens and cell debris. A cell (or debris) is engulfed into a vacuole and subjected to an intense oxidative burst,[2] and the indigestible debris and excess ROS and RNS are subsequently evacuated from the macrophage (Fig. 1B).

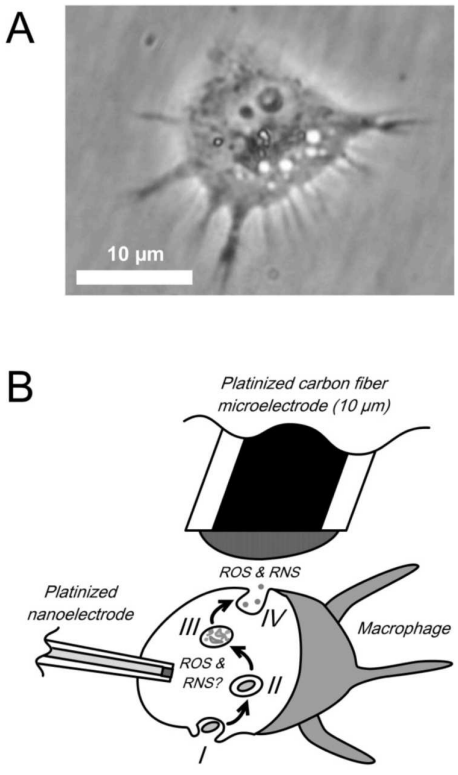

Figure 8.1. Optical micrograph of a macrophage RAW 264.7 activated by interferon-γ and LPS evidencing the presence of phagolysosomes (white spots) (A) and schematic representation of an activated macrophage undergoing phagocytosis (B). I: capture of a cell or debris; II: internalization within phagosome; III: digestion by ROS/RNS within phagolysosomes; IV: expulsion of indigestible material and excess of ROS/RNS. Also shown in B are two configurations used for the detection of ROS/RNS by either a platinized nanoelectrode inside or a microelectrode outside the cell, as discussed in the text.

The changes in oxygen and hydrogen peroxide concentrations during the oxidative burst of a stimulated macrophage cell were detected previously using the scanning electrochemical microscope.[4] Extensive studies with amperometric microelectrodes positioned in the cell proximity showed that the basal release is due to a cocktail composed of several ROS and RNS evolving from the primary production of $O_2^{\bullet-}$ and NO.[5-8] However, the concept that ROS and RNS released inside phagolysosomes may diffuse across the vacuole membrane and leak in the cell cytoplasm remains controversial.[9-12] In fact, NO and the trans-isomer of protonated peroxynitrite ion are capable of crossing biological membranes due to their lipoliphicity.[13,14] This underscores the importance of probing for the intracellular presence of ROS and RNS in activated macrophages.

For electrochemical measurements inside an activated macrophage one needs nanometer-sized electrodes that can be inserted into a living cell without causing irreparable damage to its membrane. Also, the cell membrane must seal around the nanoelectrode to prevent the detection of species penetrating inside. Previously, quantitative electrochemical experiments were performed by inserting glass-sealed, polished Pt nanoelectrodes into cultured human breast cells.[15] The cell membrane formed a tight seal around the penetrating nanotip that prevented the external solution from leaking inside the cell. This allowed the cell to remain alive for the entire time of experiment (>10 min) with a nanoelectrode inside it. However, a polished Pt nanoelectrode is not suitable for the detection of ROS and RNS, which passivate its small surface and diminish the signal. Even micrometer-sized probes used for extracellular measurements of ROS and RNS had to be coated with Pt black to improve the stability of the response.[16] Several approaches to fabricating micrometer and submicrometer-sized Pt electrodes with high surface area are available in the literature.[16-19] For quantitative intracellular measurements, platinized

probes have to be smaller (<1 µm total diameter, including glass sheath), with porous Pt surface flush with the surrounding insulator.

The methodology for fabricating nanoelectrodes by electrodeposition of metals was reported recently.[20] The electrodes were produced by electrodepositing metal into a nanocavity, which was formed by etching away a nm-thick layer of Pt from the glass-sealed, polished Pt nanoelectrode.[21] The amount of deposited metal was controlled by monitoring the charge, and its excess was removed by polishing to yield a flat electrode. This strategy cannot be used to prepare platinized nanoelectrodes because the current efficiency in deposition of Pt black is relatively low and polishing was shown to diminish the electrode response. To overcome these problems, we developed new methodology for fabricating platinized nanoelectrodes under AFM control.

8.2 Experimental Section

Chemicals: All aqueous solutions were prepared from deionized water (Milli-Q, Millipore Corp.). Phosphate buffered saline (PBS; pH 7.4; 0.137 M NaCl, 0.01 M Na_2HPO_4, and 0.003 M KCl) was prepared by dissolving tablets (Sigma) in water and used in experiments with ROS/RNS. Ferrocenemethanol from Aldrich (Milwaukee, WI) was recrystallized twice from acetone. Platinization solution contained 0.087 g hexachloroplatinic acid (Aldrich) and 0.0014 g lead(II) acetate trihydrate (Alfa Aesar) in 1 mL of water to which 36 mL PBS was added. Etching solution was prepared by mixing 60% (by volume) water, 30% 5 M $CaCl_2$, and 10% HCl. DEANONOate and sodium peroxynitrite in alkaline solution were purchased from Cayman Chemical.

Cell culture. The murine macrophage RAW 264.7 (American Type Culture Collection) cell line was cultured at 37°C under a 5 % CO_2 atmosphere in Dulbecco's modified Eagle's medium

(DMEM) containing 1.0 g L^{-1} D-glucose and sodium pyruvate (Invitrogen). The medium was supplemented with 5% fetal bovine serum (Invitrogen) and 20 μg mL^{-1} gentamicin (Sigma). Confluent monolayers of RAW 264.7 cells were resuspended through trypsinisation and plated in tissue culture Petri dishes (Nunc; 35 mm diameter) 24 h prior to electrochemical studies.

Preparation of etched Pt nanoelectrodes. Disk-type, flat nanoelectrodes were prepared by pulling 25-μm-diameter annealed Pt wires into borosilicate glass capillaries with the help of a P-2000 laser pipette puller (Sutter Instrument Co.) and polished under video microscopic control as described previously.[24] The RG (i.e., the ratio of glass radius to that of the Pt tip) varied from 5 to 10. The electrode radius was evaluated from steady-state voltammetry. The electrodes that exhibited good quality voltammetric response were etched with an alternating current of 1.5 V amplitude, 20 MHz frequency (Keithley 3940, multifunctional synthesizer), as described previously.[21] The etched electrode was cleaned by sonication in water during 5 s and imaged by the AFM to determine its radius and the recess depth. The fabrication of 10 μm platinized carbon fiber microelectrodes is described in *SI Appendix*.

AFM imaging and deposition control. An XE-120 scanning probe microscope (Park Systems) was employed for imaging nanoelectrodes and for *in-situ* control of Pt black deposition. PPP-NCHR AFM probes (Nanosensors) were used for non-contact imaging. The procedures for AFM imaging of nanoelectrodes either in air or in solution were developed recently. Briefly, a nanoelectrode was mounted vertically with its polished surface facing the AFM probe using a homemade sample holder, and the cantilever was positioned above it with the help of an optical microscope. In a non-contact mode, the tip was brought within a close proximity of the sample using the approach function, and then the nanoelectrode was moved laterally in 200 nm steps to bring the AFM probe to its apex. The travel direction was selected to effect z-axis retraction of

the piezo actuator in a close-loop mode. This corresponded to sliding of the slanted tip surface along the edge of the glass insulating sheath of the electrode. When the piezo approached its upper limit, the z-stage motor was retracted by 1 µm to maintain the actuator within its range (12 µm).

Electrodeposition of Pt black into the etched cavity was carried out in a commercial liquid cell (Park Systems), which was mounted on the stage of the XE-120 scanning probe microscope. The etched working electrode was biased to -100 ± 30 mV vs. Ag/AgCl reference in the platinization solution using an EI-400 potentiostat (Ensman Instruments). Slightly different potential values were used depending on the initial recess depth to keep deposition time close to 1 min (the larger the recess depth the slower the deposition process). The cavity filling was controlled by line scanning above the central portion of the etched nanoelectrode and monitoring the cavity depth as a function of time.

Voltammetry and electrochemical experiments with macrophages. A two-electrode setup was used for voltammetric experiments with a nanometer-sized Pt working electrode and a commercial Ag/AgCl reference. Steady-state voltammograms of either aqueous ferrocenemethanol or ferrocene in acetonitrile were obtained for electrode characterization using a BAS 100B electrochemical workstation (Bioanalytical Systems). *In-vitro* voltammetry of ROS/RNS was performed using either a BAS 100B or an EA162 Picostat (eDAQ, Australia) with an e-corder 401 system and EChem software.

Experiments with macrophages were performed at room temperature (22 ± 1^{o}C) on the stage of an inverted microscope (Axiovert 135, Zeiss) placed in a Faraday cage. For intracellular detection, the platinized nanoelectrode was moved slowly with a micromanipulator (MHW-103, Narishige) towards the cell until it touched the membrane. It was then further lowered by 500 nm

to penetrate the cell. With the MHW-103 Narishige micromanipulator this last movement could not be performed at a sufficiently slow rate as reported previously.[15] This explains why only ~20% of the insertions provided a perfect seal. In another ~50% experiments the seal seemed to be good, but was not sufficiently tight, as evidenced by a small (a few percent of that recorded in the external solution) $Ru(NH_3)_6^{3+}$ reduction wave obtained inside the cell. In remaining ~30% cases, the cell membrane was ruptured during the nanoelectrode insertion. The transients were recorded until the current attained a constant value corresponding to the baseline.

For extracellular detection of the ROS/RNS release induced by the nanoelectrode insertion, a 10-µm-diameter platinized carbon microelectrode[6-8] was initially positioned ~30 µm above the cell and polarized for 3 min before each measurement. Then, the working microelectrode tip was precisely positioned with the micromanipulator at a fixed distance (5 µm) above the surface of the macrophage. At this point, the nanoelectrode was positioned with the second micromanipulator between the microelectrode platinized surface and the cell and inserted, as described above in the case of intracellular measurements. In both cases, the subsequent release of ROS/RNS was detected in real time by chronoamperometry (AMU130 amperometer, Radiometer Analytical) at +850 mV vs. Ag/AgCl, i.e., sufficiently positive for the oxidation of all H_2O_2, $ONOO^-$, NO, and NO_2^- species. The current transients were recorded using a Powerlab 4SP D/A converter with a Chart 4.2 interface (ADInstruments). The same equipment was used to insert a nanoelectrode into the cell and record current vs. time dependences (digitized at 10 kHz).

In all cases, the total charge (Q), the maximum current (I_{max}) and the half-time width ($t_{1/2}$) were extracted from the response that corresponds to the overall oxidation processes occurring at the measurement potential.

8.3 Results and Discussion

Fabrication of the platinized nanoelectrodes The black curve in Fig. 8.2A is a voltammogram of ferrocenemethanol (FcMeOH) at a polished Pt electrode with the radius, a = 60 nm calculated from the diffusion limiting current. After etching, the diffusion current decreased to ~50% of the original value (red curve in Fig. 8.2A), which corresponds to the formation of a ~40-nm-deep cavity, according to the available theory.[21] After the platinization, the FcMeOH current increased almost ten times (green curve) indicating that the nanopore was significantly overfilled with Pt black. Most excess Pt black was removed by polishing, after which the limiting current (blue curve in Fig.8.2A) was only slightly higher than that obtained at the original polished electrode (black curve) in accordance with an SEM image (Fig. 8.2B) showing the electrode radius of ~80 nm.

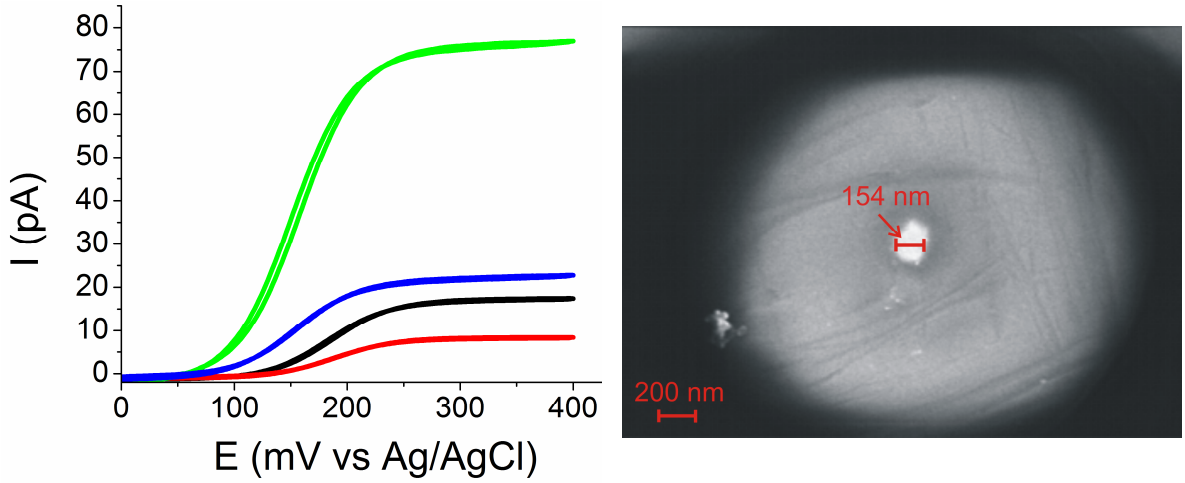

Figure 8.2. (A) Cyclic voltammograms of 1 mM FcMeOH in 0.1 M KCl obtained at a 60-nm-radius polished Pt electrode before etching (black), after etching (red), after platinization at -100 mV vs. Ag/AgCl (green), and after removing excess Pt black by polishing (blue). (B) SEM image of the same electrode after platinization and polishing.

While seemingly successful, the above example shows major difficulties in platinization of nanoelectrodes. With no efficient control, large excess of Pt black was deposited. Although it could be removed, as shown in Fig. 8.2, polished platinized electrodes typically exhibit very low responses to ROS/RNS. Finally, SEM imaging is not a convenient technique for monitoring the fabrication. It cannot be done *in-situ*; has low z-axis resolution, which does not allow one to see whether the Pt electrode is recessed, flat, or protruding; and the imaged electrodes are no longer suitable for electrochemical experiments.

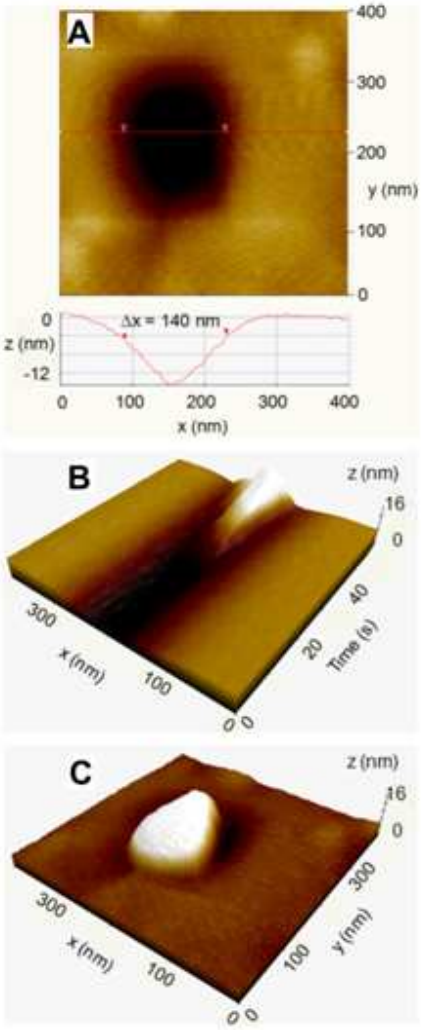

Figure 8.3. Non-contact topographic images of an etched Pt nanoelectrode in solution before (A) and after (C) the deposition of Pt black, and time evolution of a line scan during the electrodeposition process (B). The red line in A corresponds to the shown cross-section. (B) The tip was scanned along the x-axis with the scan rate of 1 Hz. The position of the line scan approximately corresponded to the red line in A.

An alternative approach—electrodeposition of Pt black under the AFM control—is illustrated in Fig. 8. A non-contact topographic image of an etched Pt electrode (Fig. 8.3A) in solution before the platinization shows the effective radius, $a \approx 70$ nm and the cavity depth of ≥20 nm (The triangular shape of the cross-section in Fig. 8.3A suggests that the tip did not reach the bottom of the cavity, and the actual depth could be larger). The deposition of Pt black was done by stepping the electrode potential to -100 mV versus Ag/AgCl, while the AFM tip, immersed in the platinization solution, was scanned in x-direction above the electrode surface. Fig. 8.3B shows a stack of 60 consecutive topographic 1D scans obtained over a 60 s period. Initially, the deposition process was slow, and its rate increased with time, as the cavity depth decreased. The deposition was stopped by stepping the electrode potential to 0 mV after Pt black completely filled the cavity and slightly protruded (by ~15 nm) from the glass sheath, as can be seen from the image of the same electrode obtained after the platinization (Fig. 8.3C).

The above methodology for fabricating Pt black nanoelectrodes, although powerful and reliable, is laborious and requires AFM instrumentation. A simpler approach to platinization makes use of the characteristic shape of the current transient. As noted above, the rate of the deposition process increases greatly when the cavity gets completely filled with metal. The corresponding sharp increase in current can be used to detect the completion of the platinization (Fig. 8.4). The etched electrode (Fig. 8.4A) was imaged in air, and then a current transient (Fig. 8.4B) was obtained in the platinization solution during the Pt black deposition into its cavity. The sharp increase in the slope of the current-time curve indicated that the nanocavity was filled, as can be seen in the image of the platinized electrode (Fig. 8.4C).

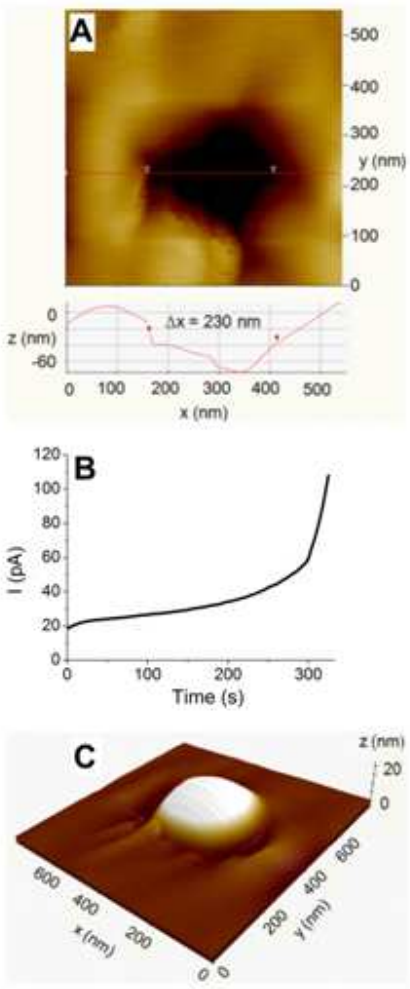

Figure 8.4. A non-contact AFM image of a 115-nm-radius etched electrode in air (A), a current transient of the Pt black deposition (B), and a topographic image of the same electrode after platinization (C).

The capacity of platinized nanoelectrodes for detecting *in vivo* the four typical electroactive ROS/RNS released by macrophages during oxidative bursts has been evaluated *in vitro* using aerated PBS solutions of hydrogen peroxide (H_2O_2), peroxynitrite anion ($ONOO^-$), nitric oxide (NO) and nitrite anion (NO_2^-) (Fig. 8.5A). NO_2^- and H_2O_2 species are stable at biological pH (7.4). Their voltammograms (red and black curves in Fig. 4A) are qualitatively similar to those recorded previously with micrometer-sized electrodes,[6,7] and the calibration curves obtained from the families of such voltammograms (Fig. 4B) are linear (Figs. 8.5C and 8.5D). Conversely, $ONOO^-$ is not stable at pH 7.4, and its voltammogram (blue curve in Fig. 8.5A) was obtained at pH 10.[22] Similarly, due to its rapid reaction with O_2, NO was generated in

situ by controlled decomposition of DEANONOate (see experimental section).[23] The instability of these species was not, however, an issue for *in-vivo* experiments where ROS/RNS are produced and detected on a much shorter experimental time scale (seconds).[6-8]

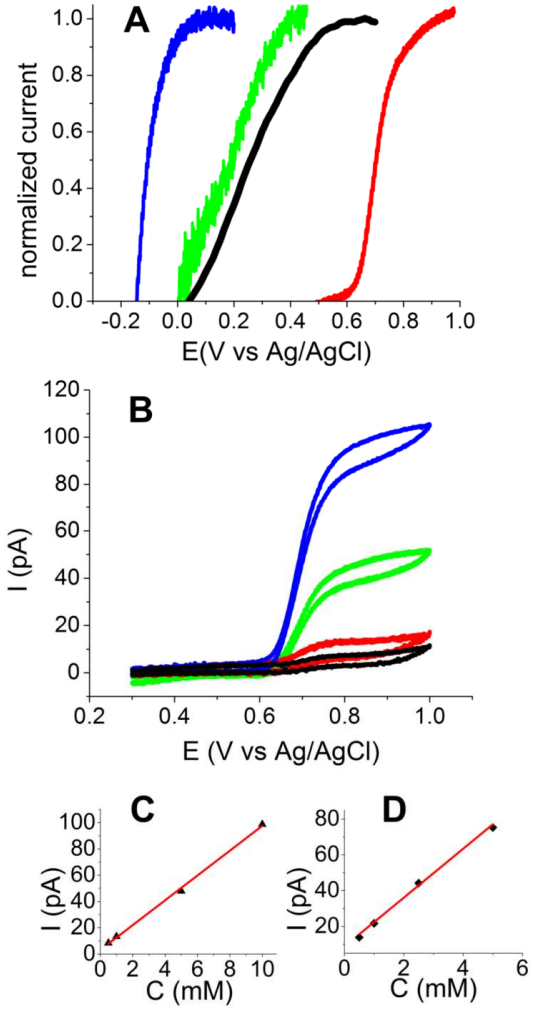

Figure 8.5. *In vitro* voltammetry of ROS/RNS species in aerated PBS. (A) Normalized voltammograms of oxidation of $ONOO^-$ (blue curve; 10 mM, pH 10, see text; the foot of the wave is merged with that of the reduction of dioxygen), NO (green, ~1 mM, see text), H_2O_2 (black; 1mM, pH 7.4), and NO_2^- (red; 5 mM, pH 7.4). Voltammograms were recorded at different platinized nanoelectrodes with the average radius of 60 nm and normalized by their plateau currents. (B) Steady-state voltammograms of NO_2^-, 10 (blue), 5 (green), 1 (red) and 0.5 mM (black) at a platinized nanoelectrode. a = 40 nm. Calibration curves for NO_2^- (C) and H_2O_2 (D) obtained from diffusion limiting currents of steady-state voltammograms.

The next step involved the characterization of the global release of the above four ROS/RNS inside activated murine macrophages (RAW 264.7 line). In these experiments, we took advantage of the previous observation that the penetration of the cell membrane by a sub-micrometer tip activates it and induces fast oxidative burst release.[6,7] Hence, a platinized nanoelectrode was inserted inside a macrophage (Fig. 8.6A) with the purpose of eliciting its response. The intensities of oxidative bursts elicited by the nanoelectrode insertion were

monitored outside the macrophage cells with a classical 10 µm platinized fiber electrode (polarized at 850 mV vs. Ag/AgCl) following a previously reported protocol (Fig. 8.6B).[6,7] The inserted nanoelectrode was also polarized at 850 mV vs. Ag/AgCl and used for monitoring the amount ROS/RNS released intracellularly (Fig. 8.6C).

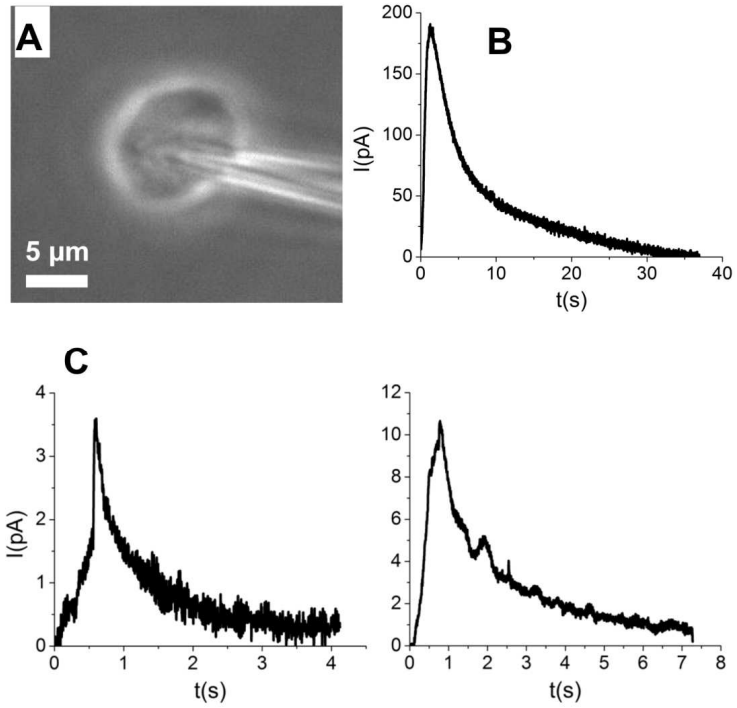

Figure 8.6. Monitoring ROS/RNS release induced by the mechanical stimulation of a macrophage. (A) Optical microscopic micrograph of a nanoelectrode (*a* = 75 nm; 800 nm O.D.) inside a macrophage. (B) Amperometric detection of ROS/RNS outside the macrophage at the 10 µm platinized carbon fiber electrode polarized at 850 mV vs. Ag/AgCl; the oxidative burst was elicited by the penetration of a platinized nanoelectrode through the macrophage membrane. (C) Two typical amperometric current traces of the ROS/RNS release inside a macrophage induced by the insertion of a platinized nanoelectrode (left: *a* = 50 nm, 700 nm O.D.; right: *a* = 40 nm, 900 nm O.D.); *E* = 850 mV vs. Ag/AgCl.

The comparison of Figures 8.6B and 8.6C shows that the responses monitored outside and inside are completely different, the outside response being more intense and lasting longer time (Table 8.1). It was then essential for us to ensure that the cell membrane formed a tight seal around the nanoelectrode shaft to eliminate a possibility that the response monitored inside the cell resulted from traces of ROS/RNS released outside and leaking into the cell. For this purpose, a series of experiments were performed with macrophages bathed in PBS containing 1 mM $Ru(NH_3)_6Cl_3$ (Fig. 8.7). The complete absence of the $Ru(NH_3)_6^{3+}$ reduction wave inside the cell, which was observed in ~20% of these experiments, provided evidence for a perfect seal.[15] The similarity of $Ru(NH_3)_6^{3+}$ voltammograms obtained before (black curve in Fig. 8.7) and after

(green curve) cell penetration indicates that the nanoelectrode capacity to respond to this species has not significantly diminished during the entire experiment. The typical current transients of ROS/RNS shown in Figure 8.6C were recorded only in cells that have exhibited no solution leakage through the membrane/glass seal.

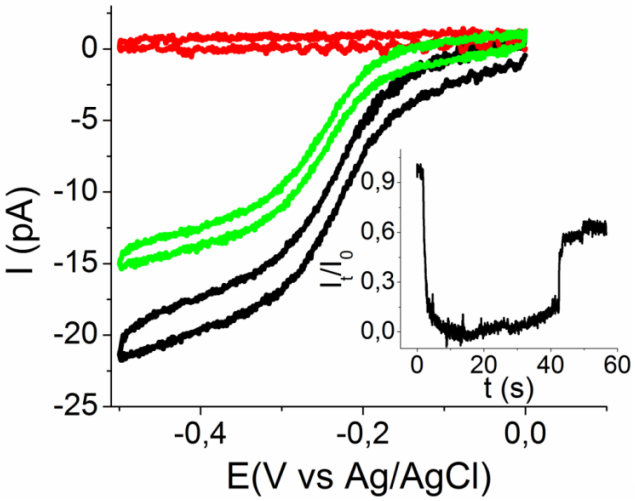

Figure 8.7. Voltammetric reduction of $Ru(NH_3)_6^{3+}$ in solution and inside a macrophage. Voltammograms were obtained before cell penetration (black), inside the cell (red) and after the removal (green) of a platinized nanoelectrode (a = 60 nm) from the cell in a solution of PBS containing 1 mM $Ru(NH_3)_6Cl_3$. The inset shows a current-time trace corresponding to the nanoelectrode insertion into the cell and its subsequent retraction to the external solution; E = -400 mV vs. Ag/AgCl.

Table 8.1. Average parameters of oxidative bursts produced by RAW 264.7 macrophages detected inside or outside the cells by different platinized electrodes.

Detection	**Electrode**	I_{max} **(pA)**	$t_{1/2}$ **(s)**	Q **(pC)**
Intracellular (n = 10)	platinized Pt nanoelectrode	11.7 ± 6.4	0.5 ± 0.1	7.7 ± 3.5
Extracellular (n = 8)	10 µm platinized carbon fiber	86 ± 23	5.8 ± 1.8	703 ± 200

Macrophages were stimulated mechanically by insertion of a platinized nanoelectrode (60 nm average radius). The potential of the detecting electrode was 850 mV vs. Ag/AgCl. All values are reported as a mean ± SEM with the corresponding number of experiments (n) indicated in parentheses.

8.4 Conclusions

In summary, the presented data supports the hypothesis of the ROS/RNS leakage from phagolysosomes. It also shows that a macrophage can avoid oxidative damage by rapidly reducing ROS/RNS concentration levels in its cytoplasm. One should notice that in our experiments the oxidative stress response was induced by mechanical stimulation of a macrophage in its rest state. However, if the efficiency of the ROS/RNS removal in activated macrophages performing phagocytosis is similar to that observed in this study, no cell damage should occur due to the leakage of ROS/RNS outside phagocytotic vacuoles.

Chapter I References and Notes

(1) (a) Wightman, R. M.; Wipf, D. O. In Electroanalytical Chemistry; Bard, A. J., Ed.; Marcel Dekker: New York, 1989; Vol. 15, p 267. (b) Forster, R. J. Chem. Soc. Rev. 1994, 289. (c) Amatore, C. In Physical Electrochemistry: Principles, Methods, and Applications; Rubinstein, I., Ed.; Marcel Dekker: New York, 1995; p 131.

(2) Bard, A. J.; Abrun˜a, H. D.; Chidsey, C. E.; Faulkner, L. R.; Feldberg, S. W.; Itaya, K.; Majda, M.; Melroy, O.; Murray, R. W.; Porter, M. D.; Soriaga, M. P.; White H. S. J. Phys. Chem. 1993, 97, 7147.

(3) de Levie, R. In Advances in Electrochemistry and Electrochemical Engineering; Gerischer, H., Tobias, C. W., Eds.; Interscience: New York, 1984; Vol. 13, p 1.

(4) Fan, F.-R. F.; Bard, A. J. Science 1995, 267, 871.

(5) Penner, R. M.; Heben, M. J.; Longin, T. L.; Lewis, N. S. Science 1990, 250, 1118.

(6) Morris, R. B.; Franta, D. J.; White, H. S. J. Phys. Chem. 1987, 91, 3559.

(7) Pendley, B. P.; Abrun˜a, H. D. Anal. Chem. 1990, 62, 782.

(8) Mirkin, M. V.; Fan, F.-R. F.; Bard, A. J. Science 1992, 257, 364.

(9) Wong, D. K. Y.; Xu, L. Y. F. Anal. Chem. 1995, 67, 4086.

(10) (a) Menon, V. P.; Martin, C. R. Anal. Chem. 1995, 67, 1920. (b) Martin, C. R., private communication, 1995. J. Chen, K. Aoki, *Electrochem. Commun.* **2002**, *4*, 24-29.

(11) (a) Bond, A. M.; Oldham, K. B.; Zoski, C. G. Anal. Chim. Acta 1989, 216,177. (b) Oldham, K. B.; Zoski, C. G. J. Electroanal. Chem. 1988, 256, 11.

(12) R. J. White, H. S. White, *Anal. Chem.* **2005**, *77*, 214A-220A.

(13) (a) Baranski, A. S. J. Electroanal. Chem. 1991, 307, 287. (b) Oldham, K. B. Anal. Chem. 1992, 64, 646

(14) V. Garcia-Morales, K. Krischer, *PNAS.* **2010**, *107*, 4528-4532.

(15) E. J. F. Dickinson, R. G. Compton, *J. Phys. Chem. C* **2009**, *113*, 17585-17589.

(16) H. S. White, private communication.

(17) Y. Li, D. Bergman, B. Zhang, *Anal. Chem*. **2009**, 81, 5496-5502.

(18) A. S. Baranski, *J. Electroanal. Chem.* **1991**, *307*, 287-292.

(19) K. B. Oldham, *Anal. Chem.* **1992**, *64*, 646-651.

(20) R. He, S. Chen, F. Yang, B. Wu, *J. Phys. Chem. B* **2006**, *110*, 3262-3270.

(21) D. Krapf, B. M. Quinn, M.-Y. Wu, H. W. Zandbergen, C. Dekker, S. G. Lemay, *Nano Lett.* **2006**, *6*, 2531-2535.

(22) R. M. Penner, M. J. Heben, T. L. Longin, N. S. Lewis, *Science* **1990**, *250*, 1118-1121.

(23) A. S. Baranski, *J. Electroanal. Chem.* **1991**, *307*, 287-292.

(24) M. J. Weaver in: *Electrified Interfaces in Physics, Chemistry and Biology* (Ed.: R. Guidelli), *NATO ASI Series*, Kluwer, Dordrecht, 1992, p. 427.

(25) J. J. Watkins H. S. White, *Langmuir* **2004,** *20*, 5474-5483.

(26) R. He, S. Chen, F. Yang, B. Wu, *J. Phys. Chem. B* **2006**, *110*, 3262-3270.

(27) M. V. Mirkin, F.- R. F. Fan, A. J. Bard, *J. Electroanal. Chem.* **1992**, *328*, 47-62.

(28) C. J. Slevin, N. J. Gray, J. V. MacPherson, M. A. Webb, P. R. Unwin, *Electrochem. Commun.* **1999**, *1*, 282-288.

(29) Y. Shao, M. V. Mirkin, G. Fish, S. Kokotov, D. Palanker, A. Lewis, *Anal. Chem.* **1997**, *69*, 1627-1634.

(30) B. B. Katemann, W. Schuhmann, *Electroanalysis* **2002**, *14*, 22-28.

(31) B. Zhang, J. Galusha, P. G. Shiozawa, G. Wang, A. J. Bergren, R. M. Jones, R. J. White, E. N. Ervin, C. C. Cauley, H. S. White, *Anal. Chem.* **2007**, *79*, 4778-4787.

(32) Y. Li, D. Bergman, B. Zhang, *Anal. Chem*. **2009**, 81, 5496-5502.

(33) J. J. Watkins, J. Chen, H. S. White, H. D. Abruña, E. Maisonhaute, C. Amatore, *Anal. Chem.* **2003**, *75*, 3962-3971.

(34) W. Nogala, J. Velmurugan and M. V. Mirkin. Submitted to *Anal Chem*

(35) M. V. Mirkin, W. Nogala, J. Velmurugan and Y. Wang , *Phys. Chem. Chem. Phys*, 10.1039/C1CP22376C

Chapter II References and Notes

(1)Murray, R. W. Chem. ReV. 2008, 108, 2688.

(2) Wehmeyer, K. R.; Deakin, M. R.; Wightman, R. M. Anal. Chem. 1985, 57, 1913.

(3) (a) Morris, R. B.; Franta, D. J.; White, H. S. J. Phys. Chem. 1987, 91, 3559. (b) Conyers, J. L.; White, H. S. Anal. Chem. 2000, 72, 4441. (c) Zhang, B.; Zhang, Y.; White, H. S. Anal. Chem. 2004, 76, 6229. (d) Zhang, B.; Galusha, J.; Shiozawa, P. G.; Wang, G.; Bergren, A. J.; Jones, R. M.; White, R. J.; Ervin, E. N.; Cauley, C. C.; White, H. S. Anal. Chem. 2007, 79, 4778.

(4) Pendley, B. P.; Abrun˜ a, H. D. Anal. Chem. 1990, 62, 782.

(5) Penner, R. M.; Heben, M. J.; Longin, T. L.; Lewis, N. S. Science 1990, 250, 1118.

(6) (a) Mirkin, M. V.; Fan, F.-R. F.; Bard, A. J. J. Electroanal. Chem. 1992, 328, 47. (b) Mirkin, M. V.; Fan, F.-R. F.; Bard, A. J. Science 1992, 257, 364. (c) Fan, F.-R. F.; Bard, A. J. Science 1995, 267, 871.

(7) (a) Shao, Y.; Mirkin, M. V.; Fish, G.; Kokotov, S.; Palanker, D.; Lewis, A. Anal. Chem. 1997, 69, 1627. (b) Sun, P.; Zhang, Z.; Guo, J.; Shao, Y. Anal. Chem. 2001, 73, 5346.

(8) Slevin, C. J.; Gray, N. J.; MacPherson, J. V.; Webb, M. A.; Unwin, P. R. Electrochem. Commun. 1999, 1, 282.

(9) Campbell, J. K.; Sun, L.; Crooks, R. M. J. Am. Chem. Soc. 1999, 121, 3779.

(10) Kranz, C.; Friedbacher, G.; Mizaikoff, B.; Lugstein, A.; Smoliner, J.; Bertagnolli, E. Anal. Chem. 2001, 732, 2491.

(11) (a) Chen, S.; Kucernak, A. Electrochem. Commun. 2002, 4, 80. (b) Chen, S.; Kucernak, A. J. Phys. Chem. B 2002, 106, 9396.

(12) Katemann, B. B.; Schuhmann, W. Electroanalysis 2002, 14, 22.

(13) Chen, J.; Aoki, K. Electrochem. Commun. 2002, 4, 24.

(14) Watkins, J. J.; Chen, J.; White, H. S.; Abrun˜ a, H. D.; Maisonhaute, E.; Amatore, C. Anal. Chem. 2003, 75, 3962.

(15) (a) Sun, P.; Mirkin, M. V. Anal. Chem. 2006, 78, 6526. (b) Sun, P.; Mirkin, M. V. Anal. Chem. 2007, 79, 5809. (c) Sun, P.; Laforge, F. O.; Abeyweera, T. P.; Rotenberg, S. A.; Carpino, J.; Mirkin, M. V, Proc. Natl.Acad. Sci. U.S.A. 2008, 105, 443. (d) Sun, P.; Mirkin, M. V. J. Am. Chem. Soc. 2008, 130, 8241.

(16) Finklea, H. O. In Electroanalytical Chemistry; Bard, A. J., Rubinstein, I., Eds.; Marcel Dekker: New York, 1996; Vol. 19, pp 109- 335.

(17) Daniel, M.-C.; Astruc, D. Chem. ReV. 2004, 104, 293.

(18) For a recent review of nanoelectrode electrochemistry see, W. M. Arrigan Analyst. 2004, 129, 1157.

(19) Mirkin, M. V.; Richards, T. C.; Bard, A. J. J. Phys. Chem. 1993, 97, 7672.

(20) Scanning Electrochemical Microscopy; Bard, A. J., Mirkin, M. V., Eds.; Marcel Dekker: New York, 2001.

(21) (a) Evans, D. H. Chem. ReV. 2008, 108, 2113. (b) Swaddle, T. W. Chem. ReV. 2005, 105, 2573.

(22) Gosavi, S.; Marcus, R. A. J. Phys. Chem. B 2000, 104, 2067.

(23) Finklea, H. O.; Yoon, K.; Chamberlain, E.; Allen, J.; Haddox, R. J. Phys. Chem. B 2001, 105, 3088.

(24) Capon, A.; Parsons, R. J. Electroanal. Chem. 1973, 46, 215.

(25) Iwasita, T.; Schmickler, W.; Schultze, J. W. Ber. Bunsen-Ges. Phys. Chem. 1985, 89, 138.

(26) Wanunu, M.; Vaskevich, A.; Rubinstein, I. J. Am. Chem. Soc. 2004, 126, 5569.

(27) (a) Shao, Y.; Mirkin, M. V. J. Phys. Chem. B 1998, 102, 9915. (b) Amphlett, J. L.; Denuault, G. J. Phys. Chem. B 1998, 102, 9946.

(28) Harris, D. C. QuantitatiVe Chemical Analysis, 6th ed.; W. H. Freeman & Co.: New York, 2003.

(29) (a) Hupp, J. T.; Weaver, M. J. J. Phys. Chem. 1985, 89, 2795. (b) Wherland, S.; Gray, H. B. In Biological Aspects of Inorganic Chemistry; Addison, A. W., Cullen, W., James, B. R., Dolphin, D., Eds.; Wiley: New York, 1977; p 289. (c) Brunschwig, B. S.; Creutz, C.; Macartney, D. H.; Sham, T. K.; Sutin, N. S. Faraday Discuss. Chem. Soc. 1982, 74, 113.

(30) Milner, T. D. F.; Weaver, M. J. J. Phys. Chem. 1985, 89, 2187.

(31) Bard, A. J.; Faulkner, L. R. Electrochemical Methods: Fundamentals and Applications, 2nd ed.; Wiley & Sons: New York, 2001; p 551.

(32) He, R.; Chen, S.; Yang, F.; Wu, B. J. Phys. Chem. B 2006, 110, 3262.

(33) (a) Quinn, B. M.; Liljeroth, P.; Ruiz, V.; Laaksonen, T.; Kontturi, K. J. Am. Chem. Soc. 2003, 125, 6644. (b) Guo, R.; Georganopoulou, D.; Feldberg, S. W.; Donkers, R.; Murray, R. W. Anal. Chem. 2005, 77, 2662.

(34) Smith, C. P.; White, H. S. Anal. Chem. 1993, 65, 3343.

(35) (a) Komarynsky, M. A.; Wahl, A. C. J. Phys. Chem. 1975, 79, 695. (b) Ganesan, V.; Rosokha, S. V.; Kochi, J. K. J. Am. Chem. Soc. 2003, 125, 2559.

Chapter III References and Notes

(1) (a) Amemiya, S.; Bard, A. J.; Fan, F.-R. F.; Mirkin, M. V.; Unwin, P. R. *Annu. Rev. Anal. Chem.* **2008**, *1*, 95. (b) Laforge, F. O.; Sun, P.; Mirkin, M. V. In Rice, S. A. (Ed), *Advances in Chemical Physics*, Vol. 139, Wiley & Sons, 2008, p. 177.

(2) Wittstock, G.; Burchardt, M.; Pust, S.E.; Shen, Y.; Zhao, C. *Angew. Chem. Int. Ed.* **2007**, *46*, 1584.

(3) Fernandez, J. L.; Walsh, D. A.; Bard, A. J. *J. Am. Chem. Soc.* **2005**, *127*, 357.

(4) (a) Barker, A. L.; Gonsalves, M.; Macpherson, J. V.; Slevin, C. J.; Unwin, P. R. *Anal. Chim. Acta* **1999**, *385*, 223. (b) Mirkin, M. V.; Tsionsky, M. In *Scanning Electrochemical Microscopy*; Bard, A. J., Mirkin, M. V., Eds.; Marcel Dekker: New York, 2001; p. 299.

(5) Amemiya, S.; Guo, J.; Xiong, H.; Gross, D. A. *Anal. Bioanal. Chem.* **2006**, *386*, 458.

(6) (a) Casillas, N.; Charlebois, S.; Smyrl, W. H.; White, H. S. *J. Electrochem. Soc.* **1993**, *140*, L142. (b) Wipf, D. O. *Colloid Surf. A* **1994**, *93*, 251.

(7) Macpherson, J. V.; Unwin, P. R. In *Scanning Electrochemical Microscopy*; Bard, A. J., Mirkin, M. V., Eds.; Marcel Dekker: New York, 2001; p. 521.

(8) Wittstock, G.; Schuhmann, W. *Anal. Chem.* **1997**, *69*, 5059.

(9) Wilson, N. R.; Clewes, S. L.; Newton, M. E.; Unwin, P. R.; Macpherson, J. V. *J. Phys. Chem. B* **2006**, *110*, 5639.

(10) Zhu, R.; Nowierski, C.; Ding, Z.; Noeel J. J.; Shoesmith, D. W. *Chem. Mater.* **2007**, *19*, 2533.

(11) Sun, P.; Laforge, F. O.; Abeyweera, T. P.; Rotenberg, S. A.; Carpino, J.; Mirkin, M. V. *Proc. Natl. Acad. Sci. U.S.A.* **2008**, *105*, 443.

(12) Xiong, H.; Gross, D. A.; Guo, J.; Amemiya, S. *Anal. Chem.* **2006**, *78*, 1946.

(13) Zhang, M.; Wittstock, G.; Shao, Y.; Girault, H. H. *Anal. Chem.* **2007**, *79*, 4833.

(14) Zhang, M.; Girault, H. H. *Electrochem. Commun*. **2007**, *9*, 1778.

(15) (a) Wipf, D. O.; Bard, A. J. *J. Electrochem. Soc*. **1991**, *138*, L4.
(b) Wipf, D. O.; Bard, A. J. *Anal. Chem.* **1992**, *64*, 1362.

(16) Fan, F-R. F. In *Scanning Electrochemical Microscopy*; Bard, A. J., Mirkin, M. V., Eds.; Marcel Dekker: New York, 2001; p. 111.

(17) (a) Mirkin, M. V.; Fan, F.-R. F.; Bard, A. J. *J. Electroanal. Chem.* **1992**, *328*, 47. (b) Slevin, C. J.; Gray, N. J.; MacPherson, J. V.; Webb, M. A.; Unwin, P. R. *Electrochem. Commun.* **1999**, *1*, 282. (c) Kranz, C.; Friedbacher, G.; Mizaikoff, B.; Lugstein, A.; Smoliner, J.; Bertagnolli, E. *Anal. Chem.* **2001**, *732*, 2491.

(18) Macpherson, J. V.; Jones, C. E.; Barker A. L.; Unwin, P. R. *Anal. Chem*. **2002**, *74*, 1841.

(19) Fan, F.-R. F., Bard, A. J. *Proc. Natl. Acad. Sci. USA* **1999**, *96*, 14222.

(20) Macpherson, J. V.; Unwin, P. R. *Anal. Chem.* **2001**, *73*, 550.

(21) (a) Sun, P.; Mirkin, M. V. *Anal. Chem.* **2006**, *78*, 6526. (b) Sun, P.; Mirkin, M. V. *Anal. Chem*. **2007**, *79*, 5809. (c) Velmurugan, J.; Sun, P.; Mirkin, M. V. *J. Phys. Chem. C* **2009,** *113*, 459.

(22) (a) Shao, Y.; Mirkin, M. V. *J. Am. Chem. Soc.* **1997**, *119*, 8103. (b) Shao, Y.; Mirkin, M. V. *J. Phys. Chem. B* **1998**, *102*, 9915. (c) Cai, C.; Tong, Y.; Mirkin, M. V. *J. Phys. Chem. B* **2004**, *108*, 17872.

(23) Shao, Y.; Girault, H. H. *J. Electroanal. Chem.* **1990**, *282*, 59.

(24) Yu, H.-Z. *Chem. Commun.* **2004**, 2633.

(25) Wei, C.; Bard, A. J.; Mirkin, M. V. *J. Phys. Chem.* **1995**, *99*, 16033.

(26) (a) MacFarlane, D. R.; Forsyth, M.; Howlett, P. C.; Pringle, J. M.; Sun, J.; Annat, G.; Neil, W.; Izgorodina, E. I. *Acc. Chem. Res.* **2007**, *40*, 1165. (b) Hapiot, P.; Lagrost, C. *Chem. Rev.* **2008**, *108*, 2238.

(27) (a) Laforge, F. O.; Kakiuchi, T.; Shigematsu, F.; Mirkin, M. V. *J. Am. .Chem. Soc.* **2004**, *126*, 15380. (b) Carano, M.; Bond, A. M. *Aust. J. Chem.* **2007**, *60*, 29. (c) Ghilane, J.; Lagrost, C.; Hapiot, P. *Anal. Chem.* **2007**, *79*, 7383. (d) Taylor, A. W.; Qiu, F.; Hu, J.; Licence, P.; Walsh D. A. *J. Phys. Chem. B* **2008**, *112*, 13292.

(28) (a) Wightman, R. M.; Wipf, D. O. In *Electroanalytical Chemistry;* Bard, A. J., Ed.; Marcel Dekker: New York, 1989; Vol. 15, p. 267. (b) Amatore, C. In *Physical Electrochemistry: Principles, Methods, and Applications*; Rubinstein, I., Ed.; Marcel Dekker: New York, 1995; p. 131.

Chapter IV References and Notes

(1) Vetter, K. J. *Electrochemical kinetics: theoretical and experimental aspects;* Academic Press: New York, 1967.

(2) *Electrocatalysis. Frontiers of Electrochemistry*, Vol. 4; Lipkowski, J.; Ross, P. N., Eds.; Wiley-VCH: Weinheim, 1998.

(3) Haas, O.; Cairns, E. J. *Electrochemical energy storage. Annual reports on the progress of chemistry*, Vol. 95C; The Royal Society of Chemistry: London, 1999, pp. 163-197.

(4) Attard, G. S.; Bartlett, P. N.; Coleman, N. R. B.; Elliott, J. M.; Owen, J. R.; Wang, J. H. *Science* **1997**, *278*, 838.

(5) Trasatti, S.; Petrii, O. A. *Pure Appl. Chem.* **1991**, *63*, 711.

(6) Bard, A. J.; Faulkner, L. R. Electrochemical Methods: Fundamentals and Applications; John Wiley & Sons, Inc.: New York, 2001.

(7) Robell, A. J.; Ballou, E. V.; Boudart, M. *J. Phys. Chem.* **1964**, *68*, 2748.

(8) Yang, R. T.; Wang, Y. *J. Am. Chem. Soc.*, **2009**, *131*, 4224.

(9) Conner, W. C.; Falconer, J. L. *Chem. Rev*. **1995**, *95*, 759.

(10) Li, Y.; Yang, R. T. *J. Am. Chem. Soc.* **2006**, *128*, 12410.

(11) Salzer, R.; Dressler, J.; Steinberg, K. H.; Roland, U.; Winkler, H.; Klaeboe, P. *Vib. Spectrosc*. **1991**, *1*, 363.

(12) Miller, M. A.; Wang, C.-Y.; Merrill, G. N. *J. Phys. Chem. C* **2009**, *113*, 3222.

(13) (a) Sun, P.; Mirkin, M. V. *Anal. Chem.* **2006**, *78*, 6526. (b) Sun, P.; Mirkin, M. V. *Anal. Chem.* **2007**, *79*, 5809. (c) Sun, P.; Mirkin, M. V. *J. Am. Chem. Soc.* **2008**, *130*, 8241.

(14) Smith, C. P.; White, H. S. *Anal. Chem.* **1993**, *65*, 3343.

(15) He, R.; Chen, S.; Yang, F.; Wu, B. J. *Phys. Chem. B* **2006**, *110*, 3262.

(16) Zhang, B.; Galusha, J.; Shiozawa, P. G.; Wang, G.; Bergren, A. J.; Jones, R. M.; White, R. J.; Ervin, E. N.; Cauley, C. C.; White, H. S. *Anal. Chem.* **2007**, *79*, 4778.

(17) Laforge, F. O.; Velmurugan, J.; Wang, Y.; Mirkin, M. V. *Anal. Chem.* **2009**, *81*, 3143.

(18) Pletcher, D.; Sotiropoulos, S. *J. Chem. Soc., Faraday Trans.* **1994**, ***90***, 3663.

(19) Velasco, J. G. *Chem. Phys. Lett*. **1999**, *313*, 7.

(20) Spohr, E. *J. Phys. Chem.* **1989**, *93*, 6171.

(21) Watkins, J. J.; Chen, J.; White, H. S.; Abruña, H. D.; Maisonhaute, E.; Amatore, C. *Anal. Chem.* **2003**, *75*, 3962.

(22) Herrero, E.; Franaszczuk, K.; Wieckowski, A. *J. Phys. Chem.* **1994,** *98,* 5074.

(23) Velmurugan, J.; Zhan, D.; Mirkin, M. V. Manuscript in preparation for *Nat. Chem.*

(24) Wightman, R. M.; Wipf, D. O. in *Electroanalytical Chemistry;* Bard, A. J., Ed.; Marcel Dekker: New York, 1989; Vol. 15, p. 267.

(25) Machado, S. A. S.; Tanaka, A. A.; Gonzalez, E. R. *Electrochim. Acta* **1991**, *36*, 1325.

(26) Elliott, J. M.; Birkin, P. R.; Bartlett, P. N.; Attard, G. S. *Langmuir* **1999**, *15*, 7411.

(27) Tu, W.; Liu, W.; Cha, C.; Wu, B. *Electrochim. Acta* **1998**, *43*, 3731.

Chapter V References and Notes

(1) Murray, R.W. Nanoelectrochemistry: Metal Nanoparticles, Nanoelectrodes, and Nanopores, *Chem. Rev.* **108**, 2688-2720 (2008).

(2) Fan, F.-R.F., Bard, A.J. Electrochemical Detection of Single Molecules. *Science* **267**, 871-874 (1995).

(3) Smith, C. P.; White, H.S. Theory of the Voltammetric Response of Electrodes of Submicron Dimensions. Violation of Electroneutrality in the Presence of Excess Supporting Electrolyte. *Anal. Chem.* **65**, 3343-3353 (1993).

(4) Sun, P., Mirkin, M.V. Electrochemistry of Individual Molecules in Zeptoliter Volumes. *J. Am. Chem. Soc.* **130**, 8241-8250 (**2008**).

(5) Bach, H., Baucke, F.K.G. & Krause, D. (eds.) *Electrochemistry of glasses and glass melts, including glass electrodes*. (Springer-Verlag, New York, 2001).

(6) Haugaard, G. The Mechanism of the Glass Electrode. *J. Phys. Chem.* **45**, 148–157 (1941).

(7) Schwabe, K. & Dahms, H. Permeability of the glass electrode to hydrogen ions with the aid of tritium tagging. *Monatsber. Deutschen Akad. Wissen.* **1**, 279-282 (1959). CAN 55:57226.

(8) Vetter, K.J. *Electrochemical kinetics: theoretical and experimental aspects.* (Academic Press, New York, 1967).

(9) Sun, P. & Mirkin, M.V. Kinetics of Electron Transfer Reactions at Nanoelectrodes. *Anal. Chem.* **78**, 6526-6534 (2006).

(10) Attard, G.S., Bartlett, P.N., Coleman, N.R.B., Elliott, J.M., Owen, J.R. & Wang, J.H. Mesoporous Platinum Films from Lyotropic Liquid Crystalline Phases. *Science* **278**, 838-840 (1997).

(11) Fletcher, S., Halliday, C.S., Gates, D., Westcott, M., Lwin, T. & Nelson, G. The response of some nucleation/growth processes to triangular scans of potential**. *J. Electroanal. Chem.* 1983**, *159*, 267-285.

(12) Shao, Y. & Mirkin, M.V. Fast Kinetic Measurements with Nanometer-Sized Pipets. Transfer of Potassium Ion from Water into Dichloroethane Facilitated by Dibenzo-18-Crown-6. *J. Am. Chem. Soc.* **119**, 8103–8104 (1997).

(13) Masterton, W.L. & Gendrano, M.C. Henry's Law Studies of Solutions of Water in Organic Solvents. *J. Phys. Chem.* **70**, 2895-2898 (1966).

(14) Harris, D.C. *Quantitative Chemical Analysis*, 6th ed. (W. H. Freeman and Company, New York, 2002, p. 397).

(15) Hubbard, A.T. & Anson. F.C. The theory and practice of electrochemistry with thin layer cells. In *Electroanalytical Chemistry* (ed. Bard, A.J.) Vol. 4, pp. 129-214 (Marcel Dekker, New York, 1970).

(16) Vonau, W., Gabel, J. & Jahn, H. Potentiometric all solid-state pH glass sensors. *Electrochim. Acta* **50**, 4981–4987 (2005).

(17) Kreuer, K.-D. Solid Potentiometric pH Electrode. *Sens. Actuators, B* **1**, 286-292 (1990).

(18) El-Giar, E.E.-D.M. & Wipf, D.O. Microparticle-based iridium oxide ultramicroelectrodes for pH sensing and imaging. *J. Electroanal. Chem.* **609**, 147-154 (2007).

(19) Malkaj, P., Dalas, E., Vitoratos, E. & Sakkopoulos, S. pH electrodes constructed from polyaniline/zeolite and polypyrrole/zeolite conductive blends. *J. Appl. Polym. Sci.* **101**, 1853-1856 (2006).

(20) Bakker, E. & Pretsch, E. Nanoscale potentiometry. *Trends Anal. Chem.* **27**, 612-618 (2008). 72.

(21) Horrocks, B.R., Mirkin, M.V., Pierce, D.T., Bard, A.J., Nagy, G. & Toth, K. Scanning Electrochemical Microscopy 19. Ion Selective Potentiostatic Microscopy. *Anal. Chem.* **65**, 1213-1224 (1993).

(22) Shao, Y., Mirkin, M.V., Fish, G.; Kokotov, S., Palanker, D. & Lewis, A. Nanometer-Sized Electrochemical Sensors. *Anal. Chem.* **69**, 1627-1634 (1997).

Chapter VI References and Notes

(1) Murray, R. W. *Chem. Rev.* **2008,** *108*, 2688.

(2) Fan, F. - R. F.; Bard, A. J. *Science* **1995**, *267*, 364.

(3) Li, Y.; Cox, J. T.; Zhang, B. *J. Am. Chem. Soc.* **2010**, *132*, 3047.

(4) Krapf, D.; Quinn, B. M.; Wu, M.-Y.; Zandbergen, H. W.; Dekker, C.; Lemay, S. G. *Nano Lett*. **2006**, *6*, 2531.

(5) Penner, R. M.; Heben, M. J.; Longin, T. L.; Lewis, N. S. *Science* **1990**, *250*, 1118.

(6) Watkins, J. J.; Chen, J.; White, H. S.; Abruna, H. D. Maisonhaute, E.; Amatore, C. *Anal. Chem.* **2003**, *75*, 3962.

(7) (a) Sun, P.; Mirkin, M. V. *Anal. Chem.* **2006**, *78*, 6526. (b) Velmurugan, J.; Sun, P.; Mirkin, M. V. *J. Phys. Chem. C* **2009**, *113*, 459.

(8) Sun, P.; Laforge, F. O.; Abeyweera, T. P.; Rotenberg, S. A.; Carpino, J.; Mirkin, M. V. *Proc. Nat. Acad. Sci. USA* 2008, *105*, 443.

(9) Velmurugan, J.; Zhan, D.; Mirkin, M. V. *Nat. Chem.* **2010**, *2*, 498.

(10) Zhan, D.; Velmurugan, J.; Mirkin, M. V. *J. Am. Chem. Soc.* **2009**, *131*, 14756.

(11) Sun P.; Mirkin, M. V. *J. Am. Chem. Soc.* **2008**, *130*, 8241.

(12) Baranski, A. S. *J. Electroanal. Chem.* **1991**, *307*, 287.

(13) Li, Y.; Bergman, D.; Zhang, B. *Anal. Chem.* **2009,** *81*, 5496.

(14) Chen, S.; Kucernak, A. *J. Phys. Chem. B* **2003**, *107*, 8392.

(15) Mirkin, M. V.; Fan, F.-R. F.; Bard, A. J. *J. Electroanal. Chem.* **1992**, *328*, 47.

(16) Sun P.; Mirkin, M. V. *Anal. Chem.* **2007**, *79*, 5809.

(17) Burt, D. P.; Wilson, N. R.; Janus, U.; Macpherson, J. V.; Unwin, P. R. *Langmuir* **2008,** *24*, 12867.

Chapter VII References and Notes

(1) R. W. Murray, *Chem. Rev.* **2008,** *108,* 2688.

(2) *Electrochemistry at the Nanoscale,* (Eds.: P. Schmuki, S. Virtanen) Springer, New York, **2009**.

(3) W. M. Arrigan, *Analyst* **2004**, *129*, 1157.

(4) K. R. Wehmeyer, M. R. Deakin, R. M. Wightman, Anal. *Chem.* **1985**, *57*, 1913.

(5) B. P. Pendley, H. D. Abruña, *Anal. Chem.* **1990**, *62*, 782.

(6) R. M .Penner, M. J. Heben, T. L. Longin, N. S. Lewis, *Science* **1990**, *250*, 1118.

(7) a) M. V. Mirkin, F.-R. F. Fan, A. J. Bard, J. *Electroanal. Chem.* **1992**, *328*, 47; b) M. V. Mirkin, F.-R. F. Fan, A. J. Bard, *Science* **1992**, *257*, 364; c) F.-R. F. Fan, A. J. Bard, *Science* **1995**, *267*, 871.

(8) a) Y. Shao, M. V. Mirkin, G. Fish, S. Kokotov, D. Palanker, A. Lewis, *Anal. Chem.* **1997**, *69*, 1627; b) P. Sun, Z. Zhang, J. Guo, Y. Shao, *Anal. Chem.* **2001**, *73*, 5346.

(9) C. J. Slevin, N. J. Gray, J. V. MacPherson, M. A. Webb, P. R. Unwin, *Electrochem. Commun.* **1999**, *1*, 282.

(10) a) J. L. Conyers, H White, H. S. *Anal. Chem.* **2000**, *72*, 4441; b) B. Zhang, J. Galusha, P. G. Shiozawa, G. Wang, A. J. Bergren, R. M. Jones, R. J. White, E. N. Ervin, C. C. Cauley, H. S. White, Anal. Chem. **2007**, 79, 4778.

(11) B. B. Katemann, W. Schuhmann, *Electroanalysis* **2002**, *14*, 22.

(12) N. Baltes, L. Thouin, C. Amatore, J. Heinze, *Angew. Chem. Int. Ed.* **2004**, *43*, 1431.

(13) C. Yang, P. Sun, Anal. Chem. **2009**, *81*, 7496.

(14) Y. Li, D. Bergman, B. Zhang, *Anal. Chem.* **2009,** *81*, 5496.

(15) a) P. Sun, M. V. Mirkin, *Anal. Chem.* **2006**, *78*, 6526; b) J. Velmurugan, P. Sun, M. V. Mirkin, *J. Phys. Chem. C* **2009**, *113*, 459; c) P. Sun, F. O. Laforge, T. P. Abeyweera, S. A. Rotenberg, J. Carpino, M. V. Mirkin, *Proc. Natl. Acad. Sci. U.S.A.* **2008**, *105*, 443.

(16) a) B. Scharifker, G. J. Hills, *Electroanal. Chem.* **1981**, *130*, 81; b) G. Gunawardena, G. Hills, B. Scharifker, *J. Electroanal. Chem.* **1981**, *130*, 99; c) G. Hllls, A. K. Pour, B. Scharifker, *Electrochim. Acta* **1983**, *28*, 891; d) A. Milchev, V. Tsakova, *Electrochim. Acta* **1985**, *30*, 138.

(17) a) J. L. Zubimendi, L. Vazquez, P. Ocon, J. M. Vara, W. E. Triaca, R. C. Salvarezza, A. J. Arvia, *J. Phys. Chem.* **1993**, *97*, 5095; b) M. E. Martins, R. C. Salvarezza, A. J. Arvia, *Electrochim. Acta* **1998**, *43*, 549.

(18) a) K. R. Wehmeyer, R. M. Wightman, *Anal. Chem.* **1985**, *57*, 1989; b) Z. Stojek, J. Osteryoung, Anal. *Chem.* **1988**, *60*, 131; c) J. Mauzeroll, E. A. Hueske, A. J. Bard, *Anal. Chem.* 2**003**, 75, 3880; d) S. Daniele, C. Bragato, I. Ciani, M.A. Baldo, *Electroanalysis* **2003**, *15*, 621.

(19) S. Chen, A. Kucernak, *J. Phys. Chem. B* **2003**, *107*, 8392.

(20) B. R. Scharifker, J. Mostany in *Encyclopedia of electrochemistry*, Vol.2 (Eds.: A. J. Bard, and M. Stratmann), Wiley-VCH, Weinheim., **2003**, pp. 512-539.

(21) M. Fleischmann, H. R. Thirsk in *Advances in Electrochemistry and Electrochemical Engineering* Vol. 3 (Ed.: P. Delahay), Interscience, New York, **1963**, pp. 123 – 210.

(22) M. P. Zach, K. H. Ng, R. M. Penner, *Science* **2000**, *290*, 2110.

(23) R. L. Deutscher, S. Fletcher, *J. Electroanal. Chem.* **1988**, *239*, 17.

(24) A. Milchev, W. S. Kruijt, M. Sluyters-Rehbach, J. H. Sluyters, *J. Electroanal. Chem.* **1993**, *362*, 21.

(25) A. Radisic, P. M. Vereecken, J. B. Hannon, P. C. Searson, F. M. Ross, *Nano Lett.* **2006**, *6*, 238.

(26) J. Velmurugan, M. V. Mirkin, manuscript in preparation.

(27) D. Zhan, J. Velmurugan, M. V. Mirkin, *J. Am. Chem. Soc.* **2009**, *131*, 14756.

(28) M. V. Mirkin, F.-R. F. Fan, A. J. Bard, *J. Electroanal. Chem.* **1992**, *328*, 47.

(29) Y. D. Gamburg, G. Zangari,*Theory and practice of metal electrodeposition* (Springer, New York, 2011).

(30) A. Milchev, *Electrocrystallization: fundamentals of nucleation and growth* (Kluwer, Boston 2002).

(31) B. R. Scharifker, J. Mostany, Three-dimensional nucleation with diffusion controlled growth: Part I. Number density of active sites and nucleation rates per site. *J. Electroanal. Chem.* **177**, 13-23 (1984).

(32) M. Sluyters-Rehbach, J. H. O. J. Wijenberg, E. Bosco, J. H. Sluyters, The theory of chronoamperometry for the investigation of electrocrystallization: mathematical description and analysis in the case of diffusion-controlled growth. *J. Electroanal. Chem.* **236**, 1-20 (1987).

(33) M. V. Mirkin, A. P. Nilov, Three-dimensional nucleation and growth under controlled potential. *J. Electroanal. Chem.* **283**, 35-51 (1990).

(34) Y. Cao, P. Searson, A. C. West, Direct numerical simulation of nucleation and three-dimensional, diffusion-controlled growth. *J. Electrochem. Soc.* **148**, C376-C382 (2001).

(35) L. Guo, A. Radisic, P. C. Searson, Kinetic Monte Carlo simulations of nucleation and growth in electrodeposition. *J. Phys. Chem. B* **109**, 24008-24015 (2005).

(36) A. Milchev, W. S. Kruijt, M. Sluyters-Rehbach, J. H. Sluyters, Probabilistic analysis of the distance between clusters randomly distributed on the electrode surface. *J. Electroanal. Chem.* **350**, 89-95 (1993).

(37) M.Y. Abyaneh, M. Fleischmann, E. Del Giudice, G. Vitiello, The investigation of nucleation using microelectrodes: I. The ensemble averages of the times of birth of the first nucleus. *Electrochim. Acta* **54**, 879-887 (2009).

(38) A. Milchev, Electrochemical nucleation on active sites—what do we measure in reality? Part I. *J. Electroanal. Chem.* **457**, 36-46 (1998).

(39) . M. E. Hyde, R. G. Compton, A review of the analysis of multiple nucleation with diffusion controlled growth. *J. Electroanal. Chem.* **549**, 1-12 (2003).

(40) A. Radisic, P. M. Vereecken, J. B. Hannon, P. C. Searson, F. M. Ross, Quantifying electrochemical nucleation and growth of nanoscale clusters using real-time kinetic data. *Nano Lett.* **6**, 238-242 (2006).

(41) G. Gunawardena, G. Hills, B. Scharifker, Induction times for the formation of single mercury nuclei on a platinum microelectrode. *J. Electroanal. Chem.* **130**, 99-112 (1981).

(42) R. L. Deutscher, S. Fletcher, Nucleation on active sites: Part IV. Invention of an electronic method of counting the number of crystals as a function of time; and the discovery of nucleation rate dispersion. *J. Electroanal. Chem.* **239**, 17-54 (1988).

(43) H. Liu, R. M. Penner, Size-Selective Electrodeposition of Mesoscale Metal Particles in the Uncoupled Limit. *J. Phys. Chem. B* **104**, 9131-9139 (2000).

(44) S. Chen, A. Kucernak, Electrodeposition of platinum on nanometer-sized carbon electrodes. *J. Phys. Chem. B* **107**, 8392-8402 (2003).

(45) M. P. Zach, K. H. Ng, R. M. Penner, Molybdenum nanowires by electrodeposition. *Science* ***290****, 2120-2123 (2000).*

(46) M. E. Hyde, R. Jacobs, R. G. Compton, In situ AFM studies of metal deposition. *J. Phys. Chem. B* **106**, 11075-11080 (2002).

(47) a) P. Sun, M. V. Mirkin, Anal. *Chem.* **2007**, *79*, 5809; b) P. Sun, M. V. Mirkin, *J. Am. Chem. Soc.* **2008**, 130, 8241.

(48) S. Fletcher, C. S. Halliday, D. Gates, M. Westcott, T. Lwin, G. Nelson, *J. Electroanal. Chem.* **1983**, *159*, 267.

(49) G. J. Hills, D. J. Schiffrin, J. Thompson, *Electrochim. Acta* **1974**, *19*, 657.

(50) a) R. M. Wightman, D. O. Wipf, in *Electroanalytical Chemistry,* Vol. 15 (Ed: A. J. Bard), Marcel Dekker, New York, **1989**, p. 267. b) C. Amatore in *Physical Electrochemistry: Principles, Methods, and Applications* (Ed.: I. Rubinstein), Marcel Dekker, New York, **1995**, p. 131.

(51) Heerman, L.; Tarallo, A. "Electrochemical nucleation on microelectrodes. Theory and experiment for diffusion-controlled growth", *J. Electroanal. Chem.* **1998**, *451*, 101.

(52) H. Liu, R. M. Penner, Size-Selective Electrodeposition of Mesoscale Metal Particles in the Uncoupled Limit. *J. Phys. Chem. B* **104**, 9131-9139 (2000).

(53) S. Chen, A. Kucernak, Electrodeposition of platinum on nanometer-sized carbon electrodes. *J. Phys. Chem. B* **107**, 8392-8402 (2003).

(54) M. P. Zach, K. H. Ng, R. M. Penner, Molybdenum nanowires by electrodeposition. *Science* ***290****, 2120-2123 (2000).*

(55) M. E. Hyde, R. Jacobs, R. G. Compton, In situ AFM studies of metal deposition. *J. Phys. Chem. B* **106**, 11075-11080 (2002).

(56) S. Fletcher, C. S. Halliday, D. Gates, M. Westcott, T. Lwin, G. Nelson, The response of some nucleation/growth processes to triangular scans of potential. *J. Electroanal. Chem.* **159**, 267–285 (1983).

(57) G. J. Hills, D. J. Schiffrin, J. Thompson, Electrochemical nucleation from molten salts—I. Diffusion controlled electrodeposition of silver from alkali molten nitrate. *Electrochim. Acta* **19**, 657-670 (1974).

(58) S. Kariuki, H. D. Dewald, Evaluation of diffusion coefficients of metallic ions in aqueous solutions. *Electroanalysis* **8**, 307-313 (1996).

(59) W. Nogala, J. Velmurugan, M. V. Mirkin, Atomic force microscopy of electrochemical nanoelectrodes, *Anal. Chem, submitted.*

(60) P. Sun, M. V. Mirkin, Scanning electrochemical microscopy with slightly recessed nanotips. *Anal. Chem.* **79**, 5809-5816 (2007).

(61) B. R. Scharifker, J. Mostany, Electrochemical nucleation and growth. In *Encyclopedia of Electrochemistry,* A. J. Bard, M. Stratmann, Eds. (Wiley VCH Weinheim, 2003), vol. 2, chap. 5.3.

(62) P. N. Bartlett, S. L. Taylor, An accurate microdisc simulation model for recessed microdisc electrodes. *J. Electroanal. Chem.* **453**, 49-60 (1998).

Chapter VIII References and Notes

(1) Bogdan C, Rollinghoff M, Diefenbach A (2000) Reactive oxygen and reactive nitrogen intermediates in innate and specific immunity. *Curr Opin Immunol* 12: 64-76.

(2) Russell DG, VanderVen BC, Glennie S, Mwandumba H, Heyderman RS (2009) The macrophage marches on its phagosome: dynamic assays of phagosome function. *Nature Reviews Immunology* 9: 594-600.

(3) Fang FC (2004) Microbial reactive oxygen and nitrogen species: Concepts and controversies. *Nat Rev Microbiol* 2: 820-832.

(4) Schrock DS, Baur JE (2007) Chemical imaging with voltammetry-scanning microscopy. *Anal Chem* 79: 7053–7061

(5) Amatore C, Arbault S, Guille M, Lemaître F (2008) Electrochemical monitoring of cell secretion: Vesicular exocytosis and oxidative stress. *Chem Rev* 108: 2585-2621.

(6) Amatore C, Arbault S, Bruce D, de Oliveira P, Erard M, Vuillaume M (2000) Analysis of individual biochemical events based on artificial synapses using ultramicroelectrodes: cellular oxidative burst. *Faraday Discuss* 116: 319-333.

(7) Amatore C, Arbault S, Bouton C, Coffi K, Drapier J-C, Ghandour H, Tong Y (2006) Monitoring in real time with a microelectrode the release of reactive oxygen and nitrogen species by a single macrophage stimulated by its membrane mechanical depolarization. *ChemBioChem* 7: 653-661.

(8) Amatore C, Arbault S, Bouton C, Drapier J-C, Ghandour H, Koh ACW (2008) Real-time amperometric analysis of reactive oxygen and nitrogen species released by single immunostimulated macrophages. *ChemBioChem* 9: 1472-1480.

(9) Nilsson E, Ghassemifar R, Brunk UT (1997) Lysosomal heterogeneity between and within cells with respect to resistance against oxidative stress. *Histochem J* 29: 857-865.

(10) Brunk UT, Svensson I (1999) Oxidative stress, growth factor starvation and Fas activation may all cause apoptosis through lysosomal leak. *Redox Report* 4: 3-11.

(11) Cech P, Lehrer RL (1984) Heterogeneity of human neutrophil phagolysosomes – Functional consequences for candidacidal activity. *Blood* 64: 147-151.

(12) Yuan XM, Li W, Brunk UT, Dalen H, Chang YH, Sevanian A (2000) Lysosomal destabilization during macrophage damage induced by cholesterol oxidation products. *Free Radic Biol Med* 28: 208-218.

(13) Denicola A, Souza JM, Radi R (1998) Diffusion of peroxynitrite across erythrocyte membranes. *Proc Natl Acad Sci USA* 95: 3566-3571.

(14) Denicola A, Souza JM, Radi R, Lissi E (1996) Nitric oxide diffusion in membranes determined by fluorescence quenching. *Arch Biochem Biophys* 328: 208-212.

(15) Sun P, Laforge FO, Abeyweera TP, Rotenberg SA, Carpino J, Mirkin MV (2008) Nanoelectrochemistry of mammalian cells. *Proc Nat Acad Sci USA* 105: 443-448.

(16) Arbault S, Pantano P, Jankowski JA, Vuillaume M, Amatore C (1995) Monitoring an oxidative stress mechanism at a single human fibroblast. *Anal Chem* 67: 3382–3390.

(17) Elliott JM, Birkin PR, Bartlett PN, Attard GS (1999) Platinum microelectrodes with unique high surface areas. *Langmuir* 15: 7411-7415.

(18) Evans SAG, Elliott JM, Andrews LM, Bartlett PN, Doyle PJ, Denuault G (2002) Detection of hydrogen peroxide at mesoporous platinum microelectrodes. *Anal Chem* 74: 1322-1326.

(19) Shim JH, Lee Y (2009) Amperometric Nitric Oxide Microsensor Based on Nanopore-Platinized Platinum: The Application for Imaging NO Concentrations. *Anal Chem* 81: 8571–8576.

(20) Velmurugan J, Mirkin MV (2010) Fabrication of Nanoelectrodes and Metal Clusters by Electrodeposition. *ChemPhysChem* 11: 3011-3017.

(21) Sun P, Mirkin MV (2007) Scanning electrochemical Microscopy with slightly recessed nanotips. *Anal Chem* 79: 5809-5816.

(22) Amatore C, Arbault S, Bruce D, de Oliveira P, Erard M, Vuillaume M (2001) Characterization of the electrochemical oxidation of peroxynitrite: Relevance to oxidative stress bursts measured at the single cell level. *Chem Eur J* 7: 4171-4179.

(23) Amatore C, Arbault S, Bouret Y, Cauli B, Guille M, Rancillac A, Rossier J (2006) Nitric oxide release during evoked neuronal activity in cerebellum slices: Detection with platinized carbon-fiber microelectrodes. *ChemPhysChem* 7: 181-187.

(24) Sun P, Mirkin MV (2006) Kinetics of electron-transfer reactions at nanoelectrodes. *Anal Chem* 78: 6526-6534.